



BINDING SERVICES

Tel +44 (0)29 2087 4949

Fax +44 (0)29 20371921

e-mail bindery@cardiff.ac.uk

EMBEDDING AT ELECTRODE SURFACES

Ian Merrick

UMI Number: U584704

All rights reserved

INFORMATION TO ALL USERS

The quality of this reproduction is dependent upon the quality of the copy submitted.

In the unlikely event that the author did not send a complete manuscript and there are missing pages, these will be noted. Also, if material had to be removed, a note will indicate the deletion.



UMI U584704

Published by ProQuest LLC 2013. Copyright in the Dissertation held by the Author.
Microform Edition © ProQuest LLC.

All rights reserved. This work is protected against
unauthorized copying under Title 17, United States Code.



ProQuest LLC
789 East Eisenhower Parkway
P.O. Box 1346
Ann Arbor, MI 48106-1346

Declaration

This work has not previously been accepted in substance for any degree and is not being concurrently submitted in candidature for any degree.

Signed I. Munshi (candidate)

Date 13/06/05

STATEMENT 1

This thesis is the result of my own investigations, except where otherwise stated. Other sources are acknowledged giving explicit references. A bibliography is appended.

Signed I. Munshi (candidate)

Date 13/06/05

Signed J.C. Ingles (supervisor)

Date 13 June 2005

Signed I. Munshi (supervisor)

Date 13/06/05

STATEMENT 2

I hereby give consent for my thesis, if accepted, to be available for photocopying and for inter-library loan, and for the title and summary to be made available to outside organisations.

Signed I. Munshi (candidate)

Date 13/06/05

Acknowledgements

I would like to thank several people for their support during studies, most especially my supervisors John Inglesfield and Gary Attard. John has provided me with invaluable assistance over the years, with his extensive expertise, guidance and, not least, his support and friendship. Gary's support and patience has also been integral to the success of my studies. Their presence over the last six years, through all my undergraduate and PhD work, has meant that there has always been someone for continual guidance and motivation.

I would like to thank my collaborators, Hiroshi Ishida and Simon Crampin, who have given up much of their time for my benefit and made my work far less demanding with their influence and suggestions. I am very much indebted to Owen Davies. His comic relief, intentional or not, has kept me motivated these last three years and he has always been there to tell me how much he doesn't know either.

Finally, I would like to thank my family for their support.

List of Publications

- I. Merrick, J.E. Inglesfield, H. Ishida, *Electronic Structure and Surface Reconstruction of Adsorbed Oxygen on Copper(001)*, Surf. Sci. **551**, 158 (2004).
- I. Merrick, J.E. Inglesfield, G.A. Attard, *Local work function and Induced Screening Effects at Stepped Pd Electrodes*, Phys. Rev. B **71**, 085407 (2005).
- I. Merrick, J.E. Inglesfield, G.A. Attard, *Electron Field Emission from Surfaces with Steps*, Phys. Rev. B, *accepted* (2005).

Abstract

Electronic structure calculations are performed on metal surfaces using an embedding method. Firstly, Cu and Ni surfaces with adsorbates are studied. The O/Cu(001) reconstruction is investigated, and it is found that atomic displacements increase bonding symmetry and is most likely the cause of reconstruction. The interaction between a single graphitic layer and the Ni(111) substrate is also studied, and it is found that interacting states are formed at Ni band gaps.

The remainder of the thesis deals with steps on metal surfaces. First, the jellium model is used to calculate the work function dependence on step density. In the low step density limit, the work function varies linearly with step density. Further calculations are performed on realistic Pd and Pt surfaces. When electric fields are applied, the screening charge of stepped surfaces is mostly located at the step edge. This is explained by the increased fields associated with the edge.

Field emission from Pd and Pt surfaces is also studied. It is found that Pd is a better emitter than Pt, owing to work function effects. Transmission is dependent on the surface parallel wavevector and decreases with increasing wavevector. The reduced work function also plays a role at stepped surfaces, although the major influence stems from the reduced *local* work function at the step site. The low effective potential at the step provides a locally reduced barrier to electron removal. In addition, an increase in transmission is seen from non-zero wavevectors for stepped surfaces. The result is that stepped Pd and Pt surfaces, with a step density of one step in every three (001) unit cells, show field emission increased by a factor of four compared with the flat (001) surfaces.

Contents

Abstract	vi
List of Figures	xii
List of Tables	xiii
1 A Brief Introduction	1
Bibliography	5
2 Theory – The Many-Body Problem	6
2.1 The Many-Body Problem	7
2.2 Bloch’s Theorem	9
2.3 Density Functional Theory	9
2.3.1 Kohn-Sham Formalism	11
2.3.2 The Exchange-Correlation Functional	13
The Local Density Approximation	13
The Generalised Gradient Approximation	15
2.4 Embedding and Green’s Functions	15
2.4.1 Applications	20
2.5 Computing within the Jellium Model	20
2.5.1 Mixing Methods	22
2.6 Computing with Atomic Structures	22
2.6.1 Linearised Augmented Plane-Waves	23
2.6.2 Plane-Wave Expansion of the Embedding Potential	24
2.6.3 Mixing Methods	25
2.6.4 Static Electric Fields	26
2.7 The Work Function	26
Bibliography	27

3	Surface Geometry	29
3.1	Metal Substrates and the Surface Miller Index	30
3.1.1	Microfacet Notation	32
3.2	Stepped Surfaces and Embedding	33
3.3	Surface Relaxation and Reconstruction	35
	Bibliography	38
4	Electronic Structure and Surface Reconstruction of Adsorbed O on Cu(001)	39
4.1	The O/Cu(001) Surface	40
4.2	Computational Aspects	43
4.3	Work Function and the Effective Charge	43
4.4	Electronic Structure of Cu(001)-c(2 × 2)-O	45
4.5	Electronic Structure of Cu(001)-(2√2 × √2)R45°-O	53
4.6	Conclusions	61
	Bibliography	64
5	Graphene/Ni(111) Surface Electronic Structure	65
5.1	Surface Structure of Graphene/Ni(111)	66
5.2	Results	69
5.3	Conclusions	75
	Bibliography	76
6	Stepped Surface – Jellium Model	78
6.1	The Jellium Model	79
6.2	Electron Density	80
6.3	Work Function Reduction	82
	Bibliography	85
7	Surface Steps – Atomic Model	86
7.1	Computational Aspects	87
7.2	The Work Function Φ	88
7.3	The Local Work Function Φ_{loc}	90
7.4	Applied Electric Fields at Flat Surfaces	96
7.5	Applied Electric Fields at Stepped Surfaces	100
7.6	Conclusions	103
	Bibliography	107
8	Electron Field Emission From Pd and Pt Surfaces	109
8.1	Computational Aspects	111
8.2	Tunneling Current Density	114
	Bibliography	120

9	Conclusions and Outlook	122
	Bibliography	125
A	Effective Charge	126
B	The Jellium Model	128
	B.1 Initial Conditions	128
	B.2 Matrix Elements	130
	B.3 Poisson's Equation	131
	Bibliography	133

List of Figures

2.1	The embedded region. A general construction showing the embedding plane S , the region of solution (region I) and the substrate (region II).	16
2.2	The surface embedded region for a jellium stepped surface.	21
2.3	Partitioning of space within the <i>linearised-augmented plane wave</i> method.	23
2.4	The surface embedded region – an atomic construction.	24
3.1	Various surface defects on an fcc crystal.	30
3.2	Low Miller index planes of the fcc crystal.	31
3.3	Spherical stereographic projection of faces of the fcc single crystal.	32
3.4	Stereographic triangle of the fcc crystal.	33
3.5	Comparison of the real part of the complex band structure of Pd obtained from the embedding potential calculation and the bulk band structure along equivalent directions. . .	34
3.6	Stepped surface structure avoiding high Miller index planes.	36
4.1	The reconstructed O/Cu(001) surface, as proposed by Woodruff <i>et al.</i>	41
4.2	Work function of Cu(001)– $c(2 \times 2)$ –O and Cu– $(2\sqrt{2} \times \sqrt{2})R45^\circ$ –O as a function of Cu–O interlayer spacing.	44
4.3	Projected density of states for atoms in the $c(2 \times 2)$ phase of the O/Cu(001) surface. . . .	46
4.4	Contour map of valence charge densities of Cu(001)– $c(2 \times 2)$ –O within energy ranges (a) $-6 < E(\text{eV}) < -5.2$, (b) $-5.5 < E(\text{eV}) < -4.5$, (c) $-1.5 < E(\text{eV}) < -1.0$, and (d) $-0.2 < E(\text{eV}) < +0.7$, on a vertical cut-plane.	47
4.5	Contour map of Cu(001)– $c(2 \times 2)$ –O of (a) the total charge density, and the valence charge density within energy range (b) $-5.9 < E(\text{eV}) < -5.4$, (c) $-1.5 < E(\text{eV}) < -1$, and (d) $-0.5 < E(\text{eV}) < +0.5$ on a vertical cut-plane.	48
4.6	(<i>lm</i>)-decomposed density of states for the $c(2 \times 2)$ phase of the O/Cu(001) surface. Cu–O interlayer spacing is 1.5 a.u.	50

4.7	(lm) -decomposed density of states for the $c(2 \times 2)$ phase of the O/Cu(001) surface. Cu–O interlayer spacing is 1.15 a.u.	51
4.8	Projected density of states for atoms in the $(2\sqrt{2} \times \sqrt{2})R45^\circ$ phase of the O/Cu(001) surface.	52
4.9	Contour maps of Cu(001)– $(2\sqrt{2} \times \sqrt{2})R45^\circ$ –O showing (a) the total charge density, and the valence charge density within energy range (b) $-4.75 < E(\text{eV}) < -4.42$, (c) $-4.42 < E(\text{eV}) < 4.18$, (d) $-4.18 < E(\text{eV}) < -4.0$, (e) $-4.0 < E(\text{eV}) < -3.0$, and (f) $-1.0 < E(\text{eV}) < -0.39$, on a vertical-cut plane normal to the line of the missing Cu row.	54
4.10	<i>Part I.</i> Contour map of Cu(001)– $(2\sqrt{2} \times \sqrt{2})R45^\circ$ –O of the valence charge density within energy range (a) $-7.0 < E(\text{eV}) < -6.27$, and (b) $-6.27 < E(\text{eV}) < -5.83$ using the surface geometry of Woodruff <i>et al.</i>	55
4.10	<i>Part II.</i> Contour map of Cu(001)– $(2\sqrt{2} \times \sqrt{2})R45^\circ$ –O of the valence charge density within energy range (c) $-5.83 < E(\text{eV}) < 5.3$, and (d) $-5.3 < E(\text{eV}) < -4.5$, using the surface geometry of Woodruff <i>et al.</i>	56
4.11	<i>Part I.</i> (lm) -decomposed density of states for the $(2\sqrt{2} \times \sqrt{2})R45^\circ$ phase of the O/Cu(001) surface, showing DOS for (a) O($l = 1, m = 0, 1 $) and (b) Cu1($l = 2, m = 0, 1 , 2 $).	58
4.11	<i>Part II.</i> (lm) -decomposed density of states for the $(2\sqrt{2} \times \sqrt{2})R45^\circ$ phase of the O/Cu(001) surface, showing DOS for (c) Cu2($l = 2, m = 0, 1 , 2 $), and (d) Cu3($l = 2, m = 0, 1 , 2 $).	59
4.12	Projected density of states for atoms in the $(2\sqrt{2} \times \sqrt{2})R45^\circ$ phase of the O/Cu(001) surface. $\mathbf{k} = \frac{\pi}{a}(\frac{2}{3}, 0)$	60
4.13	As in Fig. 4.12 but for $\mathbf{k} = \frac{\pi}{a}(\frac{8}{9}, \frac{1}{9})$	61
4.14	As in Fig. 4.12 but for $\mathbf{k} = \frac{\pi}{a}(\frac{2}{3}, \frac{2}{3})$	62
5.1	Proposed structure of graphene/Ni(111) – geometry I. (a) Top view, (b) side view.	67
5.2	Possible structures of the graphene/Ni(111) surface – geometries II and III. (a) Top view, (b) side view.	68
5.3	Spin magnetic moments of Ni atoms at various surfaces, obtained from the surface embedding code.	70
5.4	Bulk band structure of Ni, surface band structure of the graphene monolayer on Ni(111), and the surface density of states of the graphene/Ni(111) surface at certain high symmetry \mathbf{k} -points. All quantities are for majority spin.	71
5.5	l -decomposed density of states integrated through the muffin-tins of atoms in the graphene/Ni(111) surface at the $\bar{\Gamma}$ point.	73
5.6	l -decomposed density of states integrated through the muffin-tins of atoms in the graphene/Ni(111) surface at the \bar{K} point.	74
6.1	Contour maps of electron density for (a) Al(10,1) and (b) Al(5,1) stepped surfaces.	80
6.2	Charge density along a vertical line perpendicular to the Al(10,1) stepped surface, crossing a central position in the terrace.	81
6.3	Calculated work function change for Al jellium stepped surfaces as a function of step density.	83

7.1	Linear-averaged valence electron density of a three layer Pd(311) vicinal surface.	88
7.2	Total potential $V_{eff}(x, z)$ surrounding the hetero-island equivalent (a) 3(001)×(111), (b) 3(111)×(111), and (c) 3(111)×(001) stepped surfaces.	92
7.3	The same as in Fig. 7.2 but for the exchange-correlation potential $V_{xc}(x, z)$	94
7.4	The change in the local work function along Pd stepped surfaces.	95
7.5	Screening charge density $\rho_{scr}^\sigma(x, z)$ of (a) Pd(111) and (b) Pd(001) surfaces in an externally applied positive electric field ($F = 0.65 \text{ V}\text{\AA}^{-1}$).	97
7.6	Screening charge density of Pd(111) produced by an inducing field $F = 0.65 \text{ V}\text{\AA}^{-1}$ ($\sigma = -1 \times 10^{-3} \text{ a.u.}$).	98
7.7	(Upper panel) Image plane position z_{im} as a function of the applied external electric field for Pd(111) and Pd(001). (Lower panel) Planar averaged effective potential at 5 a.u. from the outermost surface plane of atoms for Pd(111) and Pd(001) surfaces.	99
7.8	Linear-averaged screening density of the Pd(311) vicinal surface in an externally applied positive electric field ($F = 0.07 \text{ V}\text{\AA}^{-1}$).	101
7.9	Linear-averaged screening density of a Pd hetero-island stepped surface in an externally applied positive electric field of (a) $F = 0.19 \text{ V}\text{\AA}^{-1}$, and (b) $F = 0.97 \text{ V}\text{\AA}^{-1}$	102
7.10	Vector field plot of the electric field superimposed onto the screening charge density at the hetero-island equivalent 3(001)×(111) surface.	103
7.11	Vector field plot of the difference in the electric field between the hetero-island equivalent 3(001)×(111) surface with, and without, an externally applied field.	104
7.12	Density of states of separate surface atoms of (a) Pt6 × (001) and (b) Pd(311) stepped surfaces.	105
8.1	Planar averaged effective potential normal to the Pt(001) surface with three different applied external electric fields.	111
8.2	Pt bulk band structure along (001) direction for $\mathbf{k}_{//}$ -points along $\bar{\Gamma}\bar{X}$ and $\bar{\Gamma}\bar{K}$	113
8.3	Tunneling current density as a function of surface-parallel wavevector for Pt and Pd surfaces.	115
8.4	$\mathbf{k}_{//}$ -resolved tunneling current density $J_{k_{//}}(E)$, and $\mathbf{k}_{//}$ -resolved density of states $n_{k_{//}}(E)$ for Pt(001) with external field strength $F = -0.65 \text{ V}\text{\AA}^{-1}$	116
8.5	$\mathbf{k}_{//}$ -resolved tunneling current density $J_{k_{//}}(E)$, and (a) $\mathbf{k}_{//}$ -resolved density of states $n_{k_{//}}(E)$, and (b) $\mathbf{k}_{//}$ -resolved Green's function (real part only) $\Re G_{k_{//}}(E)$ integrated though the surface muffin-tin of Pt(001). Applied external field strength $F = -0.97 \text{ V}\text{\AA}^{-1}$	117
8.6	Fowler-Nordheim plot of emission current densities for Pt(001), Pt(111), Pt6 × (001)(stepped) and Pd(111) surfaces.	118
B.1	Physical construction of the jellium surface.	129

List of Tables

3.1	Surface relaxation of Pd(001) and other materials.	37
4.1	Structural parameters of the Cu(001)– $(2\sqrt{2} \times \sqrt{2})$ R45°–O surface.	40
4.2	Centre of gravity (in eV) relative to E_F of the DOS of chemisorbed O for varying surface structures of the O/Cu(001) system.	63
5.1	C–Ni interlayer spacing (averaged over non-equivalent C atoms) and atomic spacing parameters as reported in the literature for different structural studies of the graphene/Ni(111) surface.	66
5.2	Work function values (eV) of clean Ni(111), graphene/Ni(111), and <i>h</i> -BN/Ni(111) surfaces.	69
7.1	Work function values (eV) of various surfaces of Pd and Pt.	89
7.2	Work functions values (eV) of (111) and (001) faces of Pd.	90
8.1	Bulk state transmission current densities ($\times 10^8 A m^{-2}$) with an applied field of $-0.65 V \text{\AA}^{-1}$, and work function values (eV) obtained from the embedding code for different surfaces of Pt and Pd.	114

CHAPTER 1

A Brief Introduction

Contents

Bibliography	5
-------------------------------	----------

Interfaces between states of matter have been the subject of intense scientific interest for many decades. The interest partly stems from the industrial importance of the solid-gas and solid-liquid interfaces [1], in connection with catalysis, corrosion, pollution control, energy conversion etc., together with many more everyday processes involving reactions at solid surfaces. From a scientific point of view, the interface region encapsulates many important and wide-spread concepts in both chemistry and physics. A chemist would deal with reactivity and electrochemical phenomena at the interface, whereas a physicist might deal with the spectroscopy of the surface electronic structure.

Traditionally, theory and experiment have gone hand in hand in surface science; theory being used to explain spectroscopic and structural data obtained from experiment. Increasingly though with advances in theoretical techniques and a surge in computational power, theory can be used as a highly accurate method for *predicting* surface properties. This thesis utilises some of the theoretical advancements, namely, density functional theory [2] (first reported by Hohenberg and Kohn in 1964 [3]), and various techniques for the solution of the Schrödinger equation, together with the recent computational availability to study the surfaces of semi-infinite metals.

The framework of density functional theory is essential in modern day electronic structure calculations since it reduces the calculation from the solution of the many-body Schrödinger equation to an effectively one-particle calculation. Density functional theory allows the calculation of highly accurate results, and reduces computation to a practical level, from an otherwise impossible calculation. This thesis deals with several areas of surface science, always solving the Schrödinger equation within the density functional theory framework.

It is generally true that the major influence on all surface properties is the electronic structure. The reduction in the atomic symmetry at the surfaces of materials causes an abrupt alteration in the electronic wavefunction from its bulk state. The result affects the full spectrum of surface properties, such as surface relaxation / reconstruction, the work function and reactivity. As well as the termination of the bulk crystal structure, the surface in general relaxes and reconstructs. Surface defects are invariably present on a real surface, but it is obviously simpler to solve the Schrödinger equation for an ideal surface with perfect two-dimensional translational symmetry, than for the surface with defects. Early chapters of this thesis deal with relaxed and reconstructed surfaces. Chapter 4 treats the O/Cu(001) reconstruction in which it will be seen that the Cu(001) surface reconstructs on O adsorption at a particular coverage. It will be shown that the fully reconstructed surface involves complicated atomic positioning. This increases surface stability by optimising the bonding at the surface. Chapter 5 investigates the interaction of a single graphitic layer on a Ni(111) substrate. Interesting bonding is seen between the metal and adlayer within Ni band gaps.

Chapters 4 and 5, although involving reconstruction and relaxation, still treat highly symmetric surface structures. In fact, the modelling of the surface electronic structure in the presence of defects is a colossal task. Symmetry breaking caused by an isolated defect means we cannot take advantage of the surface symmetry in reducing computational effort. This difficulty is unfortunate, since defects are an inherent property of any surface in nature, and can significantly alter the local properties of the surface. The importance of understanding the change in the local electronic structure around surface defects is apparent, since it is these changes which may contribute most to processes at the surface, such as reactivity, and may even alter macroscopic properties such as the work function. The difficulty may be avoided by forcing periodicity of steps onto the surface in which case a normal treatment can be made.

One of the objects of this thesis is to study the properties associated with surface defects, steps in particular, not only because of their natural occurrence, but also because of the increased reactivity associated with them. Metals of interest are Pd and Pt, which are useful in electrochemical catalysis. Chapters 6–8 describe how steps influence surface properties, firstly dealing with the jellium model (Chapter 6) and later moving onto realistic structures (Chapters 7 and 8) using the all-electron techniques used in Chapters 4 and 5. The jellium model is used to give a simplified account of the alteration of macroscopic properties, particularly the work function, due to steps. The results describe the relationship between work function and step density.

Although naturally occurring defects on surfaces may be randomly positioned, the surfaces investigated in Chapter 6 are based on stepped surfaces of a well-defined nature. This is a requirement since the surface must possess translational symmetry within the model, but it is also practical in the sense that well-defined stepped surfaces are used in experimental procedures for catalytic reactions [4], and surface characterisation [5]. This means that a direct comparison can be made between theory and experiment. However, because of the limitations of the jellium model, these results are applicable only to the nearly-free electron metals such as Al and Na.

The closing chapters (Chapters 7 and 8) deal with realistic surface structures, with steps on Pd and Pt surfaces. Here we return to the method of solution used in Chapters 4 and 5, in which atoms at the surface are treated in the framework of the full-potential linearised-augmented plane-waves (FLAPW) method. First to be dealt with are the *local* properties associated with the step. Due to the efficient screening by electrons at metal surfaces a clear distinction can be made between the electronic structure at the step and terrace sites, which differ significantly from each other. Electrochemical phenomena at these surfaces are also investigated in these chapters. The interest in the charged surface comes from experimental catalytic studies, in which redox reactions are carried out at the charged interface [4]. The highly reactive nature of the step sites on these catalytic metals makes them even more susceptible to chemical reactions.

Chapter 7 begins with a study of atomically flat surfaces in applied electric fields. Next, the stepped surfaces of Pd and Pt are charged. These investigations suggest enhanced electron screening at step sites which may in turn produce enhanced redox reactivity.

Staying with electrochemical phenomena, the thesis continues with a study of field emission of electrons at flat and stepped surfaces. The interest in field emission has recently received renewed attention because of its application in modern field-emitting devices. For instance, Spindt-type emitters and carbon nanotubes are of particular interest because of their use in flat panel displays [6, 7] and vacuum microelectronic devices [8]. Chapter 8 presents calculations on the current density resulting from electrons emitted from metal substrates in the presence of strong electric fields. When the investigation is applied to the stepped surfaces, the anticipated result of an increase in electron emission occurs. Here, the lowering of the work function, the low potential at the step site, and increased screening effects, all associated with the step site, are the cause of increased current density.

These final chapters (Chapters 6–8) investigate the local properties of the surface. It will be shown that the surface properties vary with different local geometries, and can be explained by the way in which the electron wavefunctions smooth themselves over the different geometries and defects in order to reduce kinetic energy. This is known as the Smoluchowski effect [9], and it illustrates that the all-important electron wavefunction is again the source of the defect properties. The message, as we shall see in the course of this thesis, is that a local description of stepped surfaces is needed to understand the real processes at these defective sites.

In this thesis I use atomic units (a.u.), in which $e = \hbar = m_e = 1$. The atomic unit of length is one Bohr radius a_0 , and energy is one Hartree ($1H = 27.211$ eV).

Bibliography

- [1] M. Prutton, *Introduction to Surface Physics*, Oxford Science Publications, Ch. 1 (1994).
- [2] R.O. Jones and O. Gunnarsson, *Rev. Mod. Phys.* **61**, 689 (2001).
- [3] P. Hohenberg and W. Kohn, *Phys. Rev.* **136**, B864 (1964).
- [4] G.A. Attard and A. Ahmadi, *J. of Electro. Chem.* **389**, 175 (1995).
- [5] V. Climent, G.A. Attard, J.M. Feliu, *J. of Electro. Chem.* **532**, 67 (2002). .
- [6] A.A. Talin, K.A. Dean and J.E. Jaskie, *Solid State Electronics*, **45**, 963 (2001).
- [7] M. Suzuki, T. Kusunoki., M. Sagawa and K. Tsuji, *IEEE Trans Electron Dev* **49**, 1005 (2002).
- [8] P.R. Schwoebel and I. Brodie, *J. Vac. Sci. Technol.* **B13**, 1391 (1995).
- [9] R. Smoluchowski, *Phys. Rev.* **60**, 661 (1941).

CHAPTER 2

Theory – The Many-Body Problem

Contents

2.1	The Many-Body Problem	7
2.2	Bloch's Theorem	9
2.3	Density Functional Theory	9
2.3.1	Kohn-Sham Formalism	11
2.3.2	The Exchange-Correlation Functional	13
2.4	Embedding and Green's Functions	15
2.4.1	Applications	20
2.5	Computing within the Jellium Model	20
2.5.1	Mixing Methods	22
2.6	Computing with Atomic Structures	22
2.6.1	Linearised Augmented Plane-Waves	23
2.6.2	Plane-Wave Expansion of the Embedding Potential	24
2.6.3	Mixing Methods	25
2.6.4	Static Electric Fields	26
2.7	The Work Function	26
	Bibliography	27

This chapter describes the approximations used in this thesis for the theoretical and computational method of the solution of the Schrödinger equation at metal surfaces. For complex materials, such as the transition metals we treat in this thesis, the number of interactions in the system means that the full Schrödinger equation becomes impossible to solve, even numerically [1]. This means that suitable models are required for these systems in order to obtain physical results. Here I describe the theoretical techniques implemented in this thesis for the successful solution of the Schrödinger equation for transition metal surfaces.

In Sec. 2.1 the many-body problem is discussed in more detail, and Sec. 2.3 describes density functional theory [2] which reduces the many-body problem to a single-particle calculation. This has the effect of greatly reducing the scale of computation. Section 2.4 then describes the embedding method [3], which is a method allowing the Schrödinger equation to be solved entirely within a reduced space, but still retaining the full effect of the infinite surroundings. For the specific model of the metal substrates, calculations in this thesis have been performed using both the jellium model [4] and full-potential linearised-augmented plane-waves (FLAPW) [5]. A brief mathematical background for each of these models is given in sections 2.5 and 2.6.

2.1 The Many-Body Problem

The properties of any material result from the interactions within the crystal, which enter the Hamiltonian as follows:

$$H = T_e + T_n + V_{n-n} + V_{e-e} + V_{e-n}, \quad (2.1)$$

where,

$$T_e = \sum_i T_{e_i} \quad (2.2)$$

$$T_n = \sum_J T_{n_J} \quad (2.3)$$

$$V_{e-n} = - \sum_{i,I} \frac{Z_I e^2}{|\mathbf{r}_i - \mathbf{R}_I|} \quad (2.4)$$

$$V_{n-n} = \frac{1}{2} \sum_{\substack{I,J \\ I \neq J}} \frac{Z_I Z_J e^2}{|\mathbf{R}_I - \mathbf{R}_J|} \quad (2.5)$$

$$V_{e-e} = \frac{1}{2} \sum_{\substack{i,j \\ i \neq j}} \frac{e^2}{|\mathbf{r}_i - \mathbf{r}_j|}. \quad (2.6)$$

T denotes the kinetic energy, V the potential energy, with subscripts n and e labelling ions and electrons respectively. \mathbf{R} represents the spatial coordinates of the ions and \mathbf{r} the electrons. The subscripts i, j and I, J are indices ranging respectively over the numbers of electrons and ions in the crystal. Where specified, $i \neq j$ and $I \neq J$ prevent self-interaction. The resulting Schrödinger equation for the full nuclear and electronic wavefunction $\Psi_{e,n}(\mathbf{R}, \mathbf{r})$ is:

$$\left\{ -\frac{1}{2} \sum_I \frac{\nabla_I^2}{M_I} - \frac{1}{2} \sum_i \nabla_i^2 - \sum_{i,I} \frac{Z_I e^2}{|\mathbf{r}_i - \mathbf{R}_I|} + \sum_{I,J; I \neq J} \frac{Z_I Z_J e^2}{|\mathbf{R}_I - \mathbf{R}_J|} + \sum_{i,j; i \neq j} \frac{e^2}{|\mathbf{r}_i - \mathbf{r}_j|} \right\} \Psi_{e,n}(\mathbf{R}, \mathbf{r}) = E_{e,n} \Psi_{e,n}(\mathbf{R}, \mathbf{r}), \quad (2.7)$$

where M is the nuclear mass, Z is the atomic number and $E_{e,n}$ is the total energy.

For a crystal of moderate size of say, 1 cm^3 , the total number of ions present is of the order of 10^{23} . With our coupled system of interacting ions and electrons, we are left with a vastly complicated calculation, and in order to obtain tractable techniques for the solution of the Schrödinger equation for such complex systems, we must make approximations.

The first approximation which must be made is to separate the motion of electrons and ions. Because the nuclear mass is much greater than the electron mass the motions of the nuclei are considerably slower than the rapidly moving electrons. Hence, the electron wavefunctions almost instantaneously follow the nuclear motion. This is the Born-Oppenheimer approximation [6], and although it is not applicable to systems in which the electronic and nuclear motions are comparable or coupled, it is accurate for all our purposes. This approximation allows us to separate nuclear and electronic motion:

$$\Psi_{e,n}(\mathbf{R}, \mathbf{r}) = \Phi(\mathbf{R})\Psi(\mathbf{R}, \mathbf{r}). \quad (2.8)$$

$\Phi(\mathbf{R})$ is the nuclear wavefunction, while $\Psi(\mathbf{R}, \mathbf{r})$ is the electronic wavefunction with the nuclear coordinates given by \mathbf{R} . The resulting electron Hamiltonian has the form

$$H = T_e + V_{e-e} + V_{e-n}, \quad (2.9)$$

and the electronic Schrödinger equation, within the Born-Oppenheimer approximation, now becomes:

$$\left\{ -\frac{1}{2} \sum_i \nabla_i^2 - \sum_{i,I} \frac{Z_I e^2}{|\mathbf{r}_i - \mathbf{R}_I|} + \sum_{i,j; i \neq j} \frac{e^2}{|\mathbf{r}_i - \mathbf{r}_j|} \right\} \Psi(\mathbf{R}, \mathbf{r}) = E \Psi(\mathbf{R}, \mathbf{r}), \quad (2.10)$$

where E is the electronic energy.

The result of this approximation is that the electronic wavefunctions can be solved independently of the nuclear motion. The nuclei are fixed at their mean positions and the calculation is performed for this static structure.

However, we are still left with a many-body problem treating a vast number of particles. The necessity still remains then for the calculation to be reduced to a single-particle problem, rather than the present many-body system. Fortunately, there are means available to us for such a reduction. Density functional theory (DFT) [2] allows us to reduce the many-body problem to a single-particle Schrödinger equation, and Bloch's theorem exploits the symmetry of the crystal lattice and allows us to reduce the domain over which the solution is found to one unit cell of the lattice structure. A brief account of Bloch's theorem is given in the next section, and DFT is discussed in Sec. 2.3.

2.2 Bloch's Theorem

In this section we shall briefly discuss Bloch's theorem [6]. Due to crystal periodicity, it is beneficial to include a periodic function within the expression for the electron wavefunction $\psi_k(\mathbf{r})$, which has the same period as the lattice structure. This is known as a Bloch wavefunction, and can be written

$$\psi_k(\mathbf{r}) = u(\mathbf{r})e^{i\mathbf{k}\cdot\mathbf{r}} \quad (2.11)$$

for an eigenfunction of the Schrödinger equation with wavevector \mathbf{k} in a periodic potential. $u(\mathbf{r})$ must be periodic over the lattice with lattice vector \mathbf{l} , $u(\mathbf{r} + \mathbf{l}) = u(\mathbf{r})$, and $e^{i\mathbf{k}\cdot\mathbf{r}}$ is a plane wave.

The convenience of Bloch wavefunctions is that translations of the wavefunction over the lattice vector results in a maximum change of $\psi_k(\mathbf{r})$ by a phase factor only:

$$\begin{aligned} \psi_k(\mathbf{r} + \mathbf{l}) &= u(\mathbf{r} + \mathbf{l})e^{i\mathbf{k}\cdot(\mathbf{r}+\mathbf{l})} \\ &= u(\mathbf{r})e^{i\mathbf{k}\cdot\mathbf{r}} e^{i\mathbf{k}\cdot\mathbf{l}} \\ &= \psi_k(\mathbf{r})e^{i\mathbf{k}\cdot\mathbf{l}}. \end{aligned} \quad (2.12)$$

This means that $\psi_k(\mathbf{r})$ need only be found for a single lattice unit cell, or equivalently, \mathbf{k} can be taken to always lie within the first Brillouin zone.

The periodicity of the unit cell within a crystal, over an effectively infinite region of space, means that each unit cell is indistinguishable from another. With this in mind, the electronic wavefunction within one cell must then be equivalent to that in any other, aside from some phase factor.

2.3 Density Functional Theory

Density functional theory (DFT) is based on the principle that the many-body ground state electron density $\rho(\mathbf{r})$ may be used as the basic variable in the calculation of the exact properties of the system.

This density replaces the vastly more complex many-body wavefunction Ψ , converting the calculation from $3N$ spatial variables for N electrons to just three spatial variables. This was demonstrated by Hohenberg and Kohn [7] in 1964, who showed that a unique relationship exists between the external potential $V_{ext}(\mathbf{r})$ and the corresponding electron density $\rho(\mathbf{r})$:

$$V_{ext}(\mathbf{r}) \Longleftrightarrow \rho(\mathbf{r}). \quad (2.13)$$

This is an important statement [8], and means that $\rho(\mathbf{r})$ determines implicitly all properties derivable from the Hamiltonian through the solution of the Schrödinger equation. This leads on to the two statements of DFT:

- The total electronic energy of the system is a functional of $\rho(\mathbf{r})$,

$$E = E[\rho(\mathbf{r})], \quad (2.14)$$

- and the electronic ground state energy $E_{V_{ext}}[\rho(\mathbf{r})]$ for a system in an external potential $V_{ext}(\mathbf{r})$ assumes its minimum value E_0 for the correct ground state electron density $\rho(\mathbf{r})$,

$$E_0 \leq E_{V_{ext}}[\rho(\mathbf{r})]. \quad (2.15)$$

For an extension to the spin-polarised system, the equivalent functionals become dependent on the individual electron spin densities of the ground state many-body system:

$$E = E[\rho_{\downarrow}(\mathbf{r}), \rho_{\uparrow}(\mathbf{r})] \quad (2.16)$$

$$E_0 \leq E_v[\rho_{\downarrow}(\mathbf{r}), \rho_{\uparrow}(\mathbf{r})] \quad (2.17)$$

The former statement (2.14) is valid since, from $\rho(\mathbf{r})$, all properties which can be found from the Hamiltonian are available through the solution of the Schrödinger equation. From this solution the exact many-body ground state electron wavefunction Ψ is obtainable, meaning that Ψ itself is a functional of the many-body electron density $\rho(\mathbf{r})$:

$$\Psi = \Psi[\rho(\mathbf{r})]. \quad (2.18)$$

It follows that the total energy E is also a functional of ρ , leading to (2.14).

Hohenberg and Kohn's [7] second statement (2.15) deals with the charge density equivalent to the wavefunction variational principle. Since Ψ is a functional of $\rho(\mathbf{r})$ then so too are the kinetic $\langle \Psi | T_e | \Psi \rangle$ and potential $\langle \Psi | V_{e-e} | \Psi \rangle$ energies. These energies, together with the external potential V_{ext} , form the Hamiltonian

$$H = T_e + V_{e-e} + V_{ext}. \quad (2.19)$$

Assuming these functionals can be separated from the external potential, we can define a general density functional for energy in an external potential V_{ext} as

$$E_{V_{ext}}[\rho(\mathbf{r})] = \langle \Psi | H | \Psi \rangle = \int V_{ext}(\mathbf{r})\rho(\mathbf{r})d\mathbf{r} + F[\rho(\mathbf{r})], \quad (2.20)$$

where the functionals of $\rho(\mathbf{r})$ are contained in the final term:

$$F[\rho(\mathbf{r})] = \langle \Psi | (T_e + V_{e-e}) | \Psi \rangle. \quad (2.21)$$

H in (2.20) is the total Hamiltonian corresponding to V_{ext} , T_e and V_{e-e} in (2.19). Hohenberg and Kohn proved that this functional for the ground state energy $E_{V_{ext}}[\rho(\mathbf{r})]$ of a system in an external potential V_{ext} assumes its minimum value for the correct ground state electron density $\rho(\mathbf{r})$. This is the charge density equivalent to the wavefunction variational principle.

The results of Hohenberg and Kohn can be summarised by saying that there is a unique relationship between V_{ext} and $\rho(\mathbf{r})$, and through the solution of the Schrödinger equation, the exact ground state electron density $\rho(\mathbf{r})$ determines implicitly all properties derivable from the Hamiltonian. The remaining problem is to determine the exact form of the functional $F[\rho(\mathbf{r})]$ of (2.21). $F[\rho(\mathbf{r})]$ contains the electron-electron interaction energy, but unfortunately this functional dependence is not known. However, with approximations, the total energy can be minimised via a self-consistency procedure, satisfying the variational principle. This is dealt with in the next section, which uses the Kohn-Sham [9] equations to calculate the ground state one-electron density but allows for an extra potential term to convert the single-particle effective potential to the resultant many-body effective potential.

2.3.1 Kohn-Sham Formalism

The preceding section described a method for reducing the Schrödinger equation from a calculation involving $3N$ spatial dimensions to just three dimensions, for an N -electron system. The Kohn-Sham formalism [9] further reduces computation by replacing the many-body problem with a single-particle problem. The pre-requisite of this is to convert all quantities to single-particle form. The task of re-establishing many-body effects is then left to an effective potential added on to the single-particle Hamiltonian. The unknown interaction effects can be combined into one term called exchange-correlation, E_{xc} :

$$\begin{aligned} E[\rho(\mathbf{r})] = & T_s[\rho(\mathbf{r})] + \int d^3\mathbf{r} \rho(\mathbf{r}) V_{ext}(\mathbf{r}) \\ & + \frac{1}{2} \int d^3\mathbf{r} \int d^3\mathbf{r}' \rho(\mathbf{r}) \frac{1}{|\mathbf{r}-\mathbf{r}'|} \rho(\mathbf{r}') + E_{xc}[\rho(\mathbf{r})]. \end{aligned} \quad (2.22)$$

$T_s[\rho(\mathbf{r})]$ is the single-particle kinetic term corresponding to the electron density $\rho(\mathbf{r})$ for N *non-interacting* electrons, introduced by Kohn and Sham [9],

$$T_s[\rho(\mathbf{r})] = \sum_i^N \langle \psi_i(\mathbf{r}) | -\frac{1}{2} \nabla^2 | \psi_i(\mathbf{r}) \rangle. \quad (2.23)$$

The exact form of the exchange-correlation energy is still unknown, but must depend on the electron density since all other terms of (2.22) do so.

At this point it is prudent to point out that the solution is still exact, since no approximations have been made. Simply, all that has been done is to combine all unknown quantities in to the final term of (2.22). The exchange-correlation term is then defined as the difference between the exact energy and the sum of the energy of the known terms. This leads to the idea that instead of solving the many-electron problem, the single-electron problem can be solved, but with an approximation to the exchange-correlation potential only. In practice, the approximation to this quantity is obtained from a parametrisation [10] which is based on quantum Monte-Carlo calculations of electron gases at various densities [11].

The energy $E[\rho(\mathbf{r})]$ can now be formulated from (2.22) by considering independent electrons moving in an effective potential V_{eff} , which is the self-consistent field (SCF),

$$V_{eff} = V_{SCF} = V_{ext}(\mathbf{r}) + V_H(\mathbf{r}) + V_{xc}(\mathbf{r}). \quad (2.24)$$

Here, $V_H(\mathbf{r})$ is the Hartree potential,

$$V_H = \int d^3\mathbf{r}' \rho(\mathbf{r}') \frac{1}{|\mathbf{r} - \mathbf{r}'|} \quad (2.25)$$

and V_{xc} is the single electron exchange-correlation potential,

$$V_{xc} = \frac{\delta E_{xc}}{\delta \rho(\mathbf{r})}. \quad (2.26)$$

The corresponding Schrödinger equation can then be written,

$$\left[-\frac{1}{2} \nabla^2 + V_{eff}(\mathbf{r}) \right] \psi_i(\mathbf{r}) = E_i \psi_i(\mathbf{r}) \quad i = 1 \dots N \quad (2.27)$$

with the exact electron density given by,

$$\rho(\mathbf{r}) = \sum_i^N |\psi_i(\mathbf{r})|^2, \quad (2.28)$$

and from (2.22) the exact many-body ground state energy is given by

$$E = \sum_i E_i + E_{xc}[\rho(\mathbf{r})] - \frac{1}{2} \int d^3\mathbf{r} \int d^3\mathbf{r}' \rho(\mathbf{r}) \frac{1}{|\mathbf{r} - \mathbf{r}'|} \rho(\mathbf{r}') - \int d^3\mathbf{r} V_{xc}[\rho(\mathbf{r})] \rho(\mathbf{r}). \quad (2.29)$$

Equations (2.24), and (2.27) – (2.29) are known as the Kohn-Sham equations and form the central part of the solution of the Schrödinger equation of a many-electron system by reducing it to an independent

particle problem. These independent particles then move in an effective potential of all other particles. Simplifying the many-body problem, the trade-off is the need for a self-consistent procedure to obtain the final ground state density. This is because the exact ground state charge density is needed in order to obtain the exact effective potential, since (2.24) uses (2.25) and (2.26) which in turn need $\rho(\mathbf{r})$. But on the other hand, in order to solve for the exact charge density (2.28), the exact effective potential is needed in (2.27). The remedy is to start the charge density (or effective potential) off at some trial initial state, and self-consistently use the Kohn-Sham equations to iteratively solve for the potential (or charge density). For each successive iteration, the new input state is a mixture of the input and output of the previous iteration. The whole procedure is carried out until a pre-defined limit has been reached in the difference of these input and output states.

The key to successful and rapid convergence depends on a number of factors, the most important being the initial “guessed” state, and the mixing method employed. Both these topics are covered later in this chapter.

2.3.2 Approximations to the Exchange–Correlation Functional

The Kohn-Sham equations discussed in the previous section reduce the many-body problem to a series of single-particle problems. In doing so, the electron-electron interaction problem becomes one of evaluating the exchange-correlation energy functional E_{xc} and potential V_{xc} . This section describes various approximations to these terms. Starting with the most simple method we describe the local density approximation (LDA), moving on to the more sophisticated method of the generalised gradient approximation (GGA).

The Local Density Approximation to the Exchange–Correlation Functional

The local density approximation (LDA) is the simplest functional available to us for evaluating E_{xc} and V_{xc} . Within LDA, the exchange-correlation energy (hence the potential) is calculated from the local electron density only,

$$E_{xc}[\rho(\mathbf{r})] = \int d^3\mathbf{r} \epsilon_{xc}[\rho(\mathbf{r})]\rho(\mathbf{r}) \quad (2.30)$$

where ϵ_{xc} is the exchange-correlation energy per electron of a homogeneous electron gas with the local density $\rho(\mathbf{r})$. This may seem an unreasonable assumption because the electron density within a crystal is far from homogeneity. However, it has been shown that LDA works remarkably well [2] in electronic structure calculations, but does produce small discrepancies associated with the binding energy [12], giving rise to overbinding.

The term “exchange-correlation” describes the processes involved in the interaction energy between electrons. The term “exchange” refers to the phenomenon of the “exchange hole”, where it is found that electrons of a particular spin are surrounded by a region – or hole – in which electrons of the same spin are excluded by the Pauli exclusion principle. For the free electron gas this is given by

$$\epsilon_x(\rho) = -\frac{0.458}{r_S} \quad (2.31)$$

in atomic units. r_S is the radius of a sphere containing one electron within a density ρ ,

$$r_S = \left(\frac{4}{3}\pi\rho\right)^{-\frac{1}{3}}. \quad (2.32)$$

The correlation effects are dynamical processes between electrons. These include the Coulombic repulsion between the electrons, whereby the electron cloud is pushed away from an electron moving through it. The resulting potential is dependent on the electron density of both spin states.

Care must be used when talking of exchange-correlation in DFT, since the definition differs from that of more traditional quantum chemistry methods, such as in Hartree-Fock (HF) [13]. Hartree-Fock is a variational method in which the ground state electron energy is minimised with respect to variations in the wavefunction (as opposed to the density in DFT). The resulting Schrödinger equation is

$$\left(-\frac{1}{2}\nabla^2 + V_{ext}(\mathbf{r})\right)\psi_k(\mathbf{r}) + \int d^3\mathbf{r}' V_x(\mathbf{r}, \mathbf{r}')\psi_k(\mathbf{r}') = E^{HF}_k \psi_k(\mathbf{r}) \quad (2.33)$$

where the exchange term $V_x(\mathbf{r}, \mathbf{r}')$ involves a non-local operator and gives the exact exchange energy E^{HF}_x .

One difference in the definition of the correlation energy between DFT and HF lies in reducing the many-body problem to an independent particle calculation within DFT. The Kohn-Sham equations discussed in Sec. 2.3.1 give the electron kinetic energy as the sum of the occupied one-electron kinetic terms (equation 2.23). However, this ignores the many-body effects associated with the kinetic energy, which must therefore be included elsewhere. This is not necessarily an oversight of DFT, since we can include these many-body effects in the exchange-correlation correction E_{xc} .

The total correlation effect in DFT can therefore be constructed from effects associated with the kinetic many-body effects and the electron-electron interaction effects,

$$E_c = [T - T_s] + [V_{xc} - E_x] = T_c + V_c, \quad (2.34)$$

where T is the exact many-body electron kinetic energy and $V_{xc} = V_{e-e} - V_H$, is the exchange-correlation part of the exact electron-electron interaction energy V_{e-e} . On the other hand, the traditional definition of the correlation energy E^{HF}_c , is the difference in the energy E , the exact ground state many-body electron

energy, and the HF energy, E^{HF} :

$$\begin{aligned} E_c^{\text{HF}} &= E - E^{\text{HF}} \\ &= T_c^{\text{HF}} + V_{\text{ext}_c}^{\text{HF}} + V_{H_c}^{\text{HF}} + V_c^{\text{HF}}. \end{aligned} \quad (2.35)$$

The definitions of 2.34 and 2.35 differ conceptually from one another since E_c is a functional of the exact density, whereas E_c^{HF} will involve the difference $\Delta\rho = \rho - \rho^{\text{HF}}$. The result is that the correlation corrections to the nuclear-electron interaction $V_{\text{ext}_c}^{\text{HF}}$, and the electron-electron interaction $V_{H_c}^{\text{HF}}$, do not enter into E_c . Similarly, a difference arises in the terms T_c^{HF} , V_c^{HF} and E_c^{HF} with the corresponding terms T_c , V_c and E_c .

In the DFT-LDA, the exchange and correlation effects are most successfully taken care of by parametrisation of the exchange-correlation energy of the free-electron gas as a function the electron density. The most popular of these, and the one which is used throughout the LDA calculations in this thesis is the Perdew-Zunger [10] parametrisation of the Ceperley-Alder [11] Monte-Carlo calculations for $\epsilon_{\text{xc}}[\rho(\mathbf{r})]$.

The Generalised Gradient Approximation to the Exchange-Correlation Functional

The incentive to use the generalised gradient approximation (GGA) in electronic structure calculations is that it is based on a more realistic model of exchange and correlation. Since interactions between electrons do not simply rely on a local density dependence, GGA, which includes non-local properties of the electronic structure, is able to deal more effectively with these interactions. Instead of relying solely on the electron density $\rho(\mathbf{r})$, as LDA does in (2.30), GGA depends also on the gradient of $\rho(\mathbf{r})$:

$$E_{\text{xc}}^{\text{GGA}}[\rho(\mathbf{r})] = \int d\mathbf{r}^3 \epsilon_x^{\text{LDA}}[\rho(\mathbf{r})] F_{\text{xc}}^{\text{GGA}}[\rho(\mathbf{r}), s(\mathbf{r})] \rho(\mathbf{r}) \quad (2.36)$$

where

$$s(\mathbf{r}) = \frac{|\nabla[\rho(\mathbf{r})]|}{2k_{\text{F}}\rho} \bigg|_{\rho=\rho(\mathbf{r})}. \quad (2.37)$$

Equation (2.36) is the generic form of GGA. The enhancement factor $F_{\text{xc}}^{\text{GGA}}(\rho, s)$ (over LDA exchange) is a function of the local density ρ and a scaled gradient s and different forms of this factor have been given [12]. Various electronic structure codes use GGA, including PW91 [14] and BLYP [15]. Even though the present version of the computer code used in this thesis has at its disposal various GGA functionals, the calculations described here have only been performed using LDA, for compatibility with earlier versions.

2.4 Embedding and Green's Functions

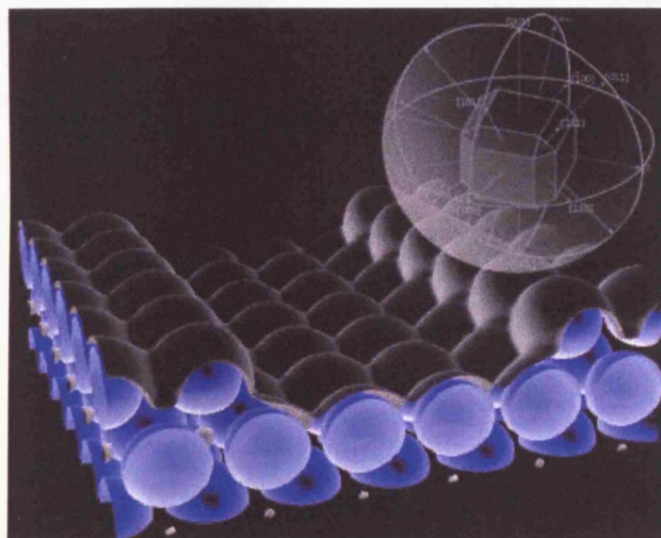
The calculations in this thesis are performed within the embedding method [3], which is a way of calculating the electronic structure of a surface for a semi-infinite system. This section describes the method



Embedding at Electrode Surfaces

**A thesis submitted
to Cardiff University,
for the degree of
Doctor of Philosophy**

May, 2005



Ian Merrick



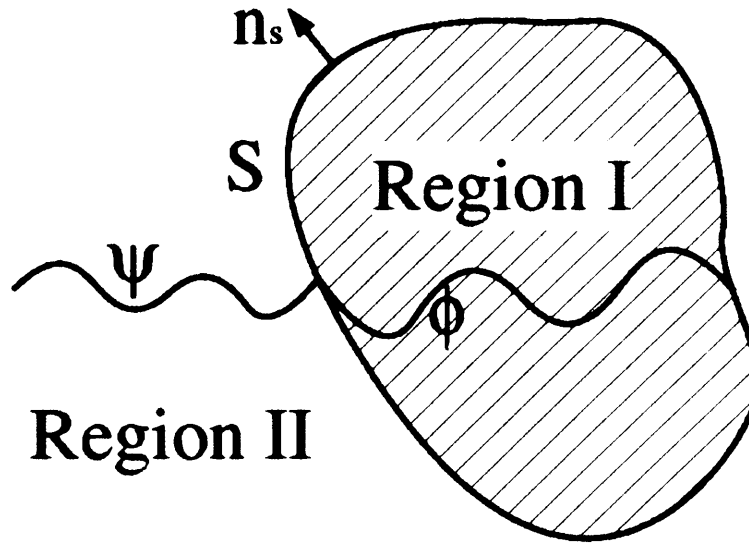


Figure 2.1: The embedded region. A general construction showing the embedding plane S , the region of solution (region I) and the substrate (region II). The substrate wavefunction ψ matches onto the trial wavefunction ϕ in region I in amplitude, but not derivative.

of embedding, showing its mathematical construction as described by Inglesfield in his 1981 paper [3]. Subsequent sections demonstrate its applicability to surface science and take a brief look at its other varied uses.

Inglesfield's description of embedding is variational in principle, in which the standard definition of the expectation value of energy is given by

$$E = \frac{\langle \Psi_0 | H | \Psi_0 \rangle}{\langle \Psi_0 | \Psi_0 \rangle} = \text{minimum} \quad (2.38)$$

where Ψ_0 is the exact ground-state electron wavefunction and H is the Hamiltonian. Instead of dealing with a complete system, or even with a reduced system (as in slab calculations), the embedding method partitions space and concentrates on the region of interest, region I (Fig. 2.1). This has the benefit of reducing the domain of Ψ_0 to a finite, local region. The boundary of this region is denoted by S , which is a surface over which the trial wavefunction $\phi(\mathbf{r})$ matches in amplitude to the exact solution $\psi(\mathbf{r})$ of the external region II:

$$\Psi(\mathbf{r}) = \begin{cases} \phi(\mathbf{r}), & \mathbf{r} \in I \\ \psi(\mathbf{r}), & \mathbf{r} \in II \end{cases} \quad (2.39)$$

and,

$$\phi(\mathbf{r}_S) = \psi(\mathbf{r}_S), \quad (2.40)$$

where $\Psi(\mathbf{r}) = \Psi_0(\mathbf{r})$ on self-consistency. A pictorial representation is given in Fig. 2.1 showing region I as shaded, and region II separated from region I by the boundary S . ϕ matches onto ψ in amplitude but

no assumptions are made, or conditions forced, with regard to derivative matching. Substituting (2.39) into (2.38) yields

$$E = \frac{\left\{ \int_I d^3\mathbf{r} \phi^*(\mathbf{r}) H \phi(\mathbf{r}) + \epsilon \int_{II} d^3\mathbf{r} \psi^*(\mathbf{r}) \psi(\mathbf{r}) + \frac{1}{2} \int_S d^2\mathbf{r}_S \phi^*(\mathbf{r}_S) \left(\frac{\partial \phi(\mathbf{r}_S)}{\partial n_S} - \frac{\partial \psi(\mathbf{r}_S)}{\partial n_S} \right) \right\}}{\int_I d^3\mathbf{r} \phi^*(\mathbf{r}) \phi(\mathbf{r}) + \int_{II} d^3\mathbf{r} \psi^*(\mathbf{r}) \psi(\mathbf{r})}. \quad (2.41)$$

The first two terms of the numerator of (2.41) are volume integrals over I and II respectively. H is the single-particle Hamiltonian and ϵ is the energy at which the wavefunction $\psi(\mathbf{r})$ in region II is evaluated. The third term arises from the discontinuity of the normal derivative at the boundary, where \mathbf{r} is placed on S (denoted by \mathbf{r}_S).

So far the energy expectation value is given in terms of $\phi(\mathbf{r})$ and $\psi(\mathbf{r})$. The remaining proof uses Green's theorem to manipulate (2.41) to obtain an expression in terms of $\phi(\mathbf{r})$ only. The derivative term $\frac{\partial \psi(\mathbf{r}_S)}{\partial n_S}$ therefore needs to be expressed in terms of $\phi(\mathbf{r})$ and similarly the volume integral of $|\psi(\mathbf{r})|^2$ over region II.

We deal first with the surface integral involving the derivative terms. We introduce the Green's function $G_0(\mathbf{r}, \mathbf{r}')$ for region II at energy ϵ , and then multiply the Schrödinger equation for $G_0(\mathbf{r}, \mathbf{r}')$ by $\psi(\mathbf{r})$, and that for $\psi(\mathbf{r})$ by G_0 . We have

$$\psi(\mathbf{r}) \left(-\frac{1}{2} \nabla^2 + V(\mathbf{r}) - \epsilon \right) G_0(\mathbf{r}, \mathbf{r}') = \psi(\mathbf{r}) \delta(\mathbf{r} - \mathbf{r}'), \quad (2.42)$$

$$G_0(\mathbf{r}, \mathbf{r}') \left(-\frac{1}{2} \nabla^2 + V(\mathbf{r}) - \epsilon \right) \psi(\mathbf{r}) = 0. \quad (2.43)$$

Subtracting (2.43) from (2.42) gives

$$-\frac{1}{2} \left(\psi(\mathbf{r}) \nabla^2 G_0(\mathbf{r}, \mathbf{r}') - G_0(\mathbf{r}, \mathbf{r}') \nabla^2 \psi(\mathbf{r}) \right) = \psi(\mathbf{r}) \delta(\mathbf{r} - \mathbf{r}'). \quad (2.44)$$

After integrating over region II, the use of Green's theorem gives the result

$$\psi(\mathbf{r}) = -\frac{1}{2} \int_S d^2\mathbf{r}'_S \left(G_0(\mathbf{r}, \mathbf{r}'_S) \frac{\partial \psi(\mathbf{r}'_S)}{\partial n_S} - \psi(\mathbf{r}'_S) \frac{\partial G_0(\mathbf{r}, \mathbf{r}'_S)}{\partial n_S} \right). \quad (2.45)$$

The change of sign on the right-hand side of (2.45) is introduced because of the convention in embedding that the surface normal derivative is taken from region I to II. Equation (2.45) also involves swapping $\mathbf{r} \leftrightarrow \mathbf{r}'_S$. By placing \mathbf{r} on S and forcing a boundary condition of $G_0(\mathbf{r}_S, \mathbf{r}'_S)$ to have zero surface-normal derivative on S , we are left with

$$\psi(\mathbf{r}_S) = -\frac{1}{2} \int_S d^2\mathbf{r}'_S G_0(\mathbf{r}_S, \mathbf{r}'_S) \frac{\partial \psi(\mathbf{r}'_S)}{\partial n_S}, \quad (2.46)$$

and inverting this equation, together with the result $\psi(\mathbf{r}_S) = \phi(\mathbf{r}_S)$ gives

$$\frac{\partial \psi(\mathbf{r}_S)}{\partial n_S} = -2 \int_S d^2\mathbf{r}'_S G_0^{-1}(\mathbf{r}_S, \mathbf{r}'_S) \phi(\mathbf{r}'_S). \quad (2.47)$$

This equation is well established in mathematics and is known as Dirichlet-to-Neumann mapping. It converts a problem from that in which $\psi(\mathbf{r}_S)$ (or $\phi(\mathbf{r}_S)$) is known (Dirichlet boundary conditions) to a problem in which its derivative $\frac{\partial\psi(\mathbf{r}_S)}{\partial n_S}$ is known (Neumann boundary conditions). Here, the Dirichlet-to-Neumann operator G_0^{-1} is the embedding potential, and is the surface inverse Green's function at an energy ϵ of the region II Schrödinger equation.

Having obtained an expression for $\frac{\partial\psi(\mathbf{r}_S)}{\partial n_S}$ in terms of the region I trial wavefunction, the remaining volume integral of region II needs rearranging in order to similarly depend only upon ϕ . Starting from

$$H\psi(\mathbf{r}) = \epsilon\psi(\mathbf{r}), \quad \mathbf{r} \in II \quad (2.48)$$

and varying ϵ by a small amount, gives

$$H\delta\psi(\mathbf{r}) = \delta\epsilon\psi(\mathbf{r}) + \epsilon\delta\psi(\mathbf{r}). \quad (2.49)$$

Multiplying (2.49) by $\psi^*(\mathbf{r})$ and the complex conjugate of the Schrödinger equation in II by $\delta\psi(\mathbf{r})$ gives

$$\psi^*(\mathbf{r})H\delta\psi(\mathbf{r}) = \psi^*(\mathbf{r})\delta\epsilon\psi(\mathbf{r}) + \psi^*(\mathbf{r})\epsilon\delta\psi(\mathbf{r}), \quad (2.50)$$

$$\delta\psi(\mathbf{r})H\psi^*(\mathbf{r}) = \delta\psi(\mathbf{r})\epsilon\psi^*(\mathbf{r}). \quad (2.51)$$

Subtracting (2.51) from (2.50):

$$-\frac{1}{2} \left(\psi^*(\mathbf{r})\nabla^2 \frac{\partial\psi(\mathbf{r})}{\partial\epsilon} - \frac{\partial\psi(\mathbf{r})}{\partial\epsilon} \nabla^2 \psi^*(\mathbf{r}) \right) = \psi^*(\mathbf{r})\psi(\mathbf{r}) \quad (2.52)$$

and integrating through II:

$$\int_{II} d^3\mathbf{r} \psi^*(\mathbf{r})\psi(\mathbf{r}) = -\frac{1}{2} \int_{II} d^3\mathbf{r} \left(\psi^*(\mathbf{r})\nabla^2 \frac{\partial\psi(\mathbf{r})}{\partial\epsilon} - \frac{\partial\psi(\mathbf{r})}{\partial\epsilon} \nabla^2 \psi^*(\mathbf{r}) \right). \quad (2.53)$$

Application of Green's theorem gives

$$\int_{II} d^3\mathbf{r} \psi^*(\mathbf{r})\psi(\mathbf{r}) = \frac{1}{2} \int_S d^2\mathbf{r}_S \left(\psi^*(\mathbf{r}_S) \frac{\partial}{\partial n_S} \frac{\partial\psi(\mathbf{r})}{\partial\epsilon} - \frac{\partial\psi(\mathbf{r}_S)}{\partial\epsilon} \frac{\partial\psi^*(\mathbf{r}_S)}{\partial n_S} \right) \quad (2.54)$$

where the change in sign of the right-hand side of (2.54) is again due to the surface normal derivative convention of embedding. Substituting (2.47) into (2.54) produces

$$\begin{aligned} \int_{II} d^3\mathbf{r} \psi^*(\mathbf{r})\psi(\mathbf{r}) = & - \int_S d^2\mathbf{r}_S \left(\psi^*(\mathbf{r}_S) \frac{\partial}{\partial\epsilon} \int_S d^2\mathbf{r}'_S G_0^{-1}(\mathbf{r}_S, \mathbf{r}'_S) \phi(\mathbf{r}'_S) \right. \\ & \left. - \frac{\partial\psi(\mathbf{r}_S)}{\partial\epsilon} \int_S d^2\mathbf{r}'_S G_0^{-1}(\mathbf{r}_S, \mathbf{r}'_S) \phi(\mathbf{r}'_S) \right). \end{aligned} \quad (2.55)$$

But $\psi(\mathbf{r}_S) = \phi(\mathbf{r}_S)$, and because this does not depend on ϵ we can rearrange (2.55) to give

$$\int_{II} d^3\mathbf{r} \psi^*(\mathbf{r})\psi(\mathbf{r}) = - \int_S d^2\mathbf{r}_S \int_S d^2\mathbf{r}'_S \phi^*(\mathbf{r}_S) \frac{\partial G_0^{-1}(\mathbf{r}_S, \mathbf{r}'_S)}{\partial\epsilon} \phi(\mathbf{r}'_S). \quad (2.56)$$

By substituting (2.47) and (2.56) in to (2.41), Inglesfield finally obtains the expectation value of the energy in terms of quantities dependent entirely on region I and the boundary S :

$$E = \frac{\left(\int_I d^3\mathbf{r} \phi^*(\mathbf{r}) H \phi(\mathbf{r}) + \frac{1}{2} \int_S d^2\mathbf{r}_S \phi^*(\mathbf{r}_S) \frac{\partial \phi(\mathbf{r}_S)}{\partial n_S} + \int_S d^2\mathbf{r}_S \int_S d^2\mathbf{r}'_S \phi^*(\mathbf{r}_S) G_0^{-1}(\mathbf{r}_S, \mathbf{r}'_S) \phi(\mathbf{r}'_S) - \epsilon \int_S d^2\mathbf{r}_S \int_S d^2\mathbf{r}'_S \phi^*(\mathbf{r}_S) \frac{\partial G_0^{-1}(\mathbf{r}_S, \mathbf{r}'_S)}{\partial \epsilon} \phi(\mathbf{r}'_S) \right)}{\int_I d^3\mathbf{r} \phi^*(\mathbf{r}) \phi(\mathbf{r}) - \int_S d^2\mathbf{r}_S \int_S d^2\mathbf{r}'_S \phi^*(\mathbf{r}_S) \frac{\partial G_0^{-1}(\mathbf{r}_S, \mathbf{r}'_S)}{\partial \epsilon} \phi(\mathbf{r}'_S)}. \quad (2.57)$$

By expanding the wavefunction ϕ in a set of functions,

$$\phi(\mathbf{r}) = \sum_i a_i \chi_i(\mathbf{r}), \quad (2.58)$$

it follows that the matrix representation of the single-particle embedded Schrödinger equation is given by

$$\sum_j \left[H_{ij} + (G_0^{-1})_{ij} + (E - \epsilon) F_{ij} \right] a_j = E \sum_j O_{ij} a_j, \quad (2.59)$$

where the matrix elements H_{ij} , $(G_0^{-1})_{ij}$, and F_{ij} can be expressed in terms of the basis functions χ_i by

$$H_{ij} = \int_I d^3\mathbf{r} \chi_i^*(\mathbf{r}) H \chi_j(\mathbf{r}) + \frac{1}{2} \int_S d^2\mathbf{r}_S \chi_i^*(\mathbf{r}_S) \frac{\partial \chi_j(\mathbf{r}_S)}{\partial n_S} \quad (2.60)$$

$$(G_0^{-1})_{ij} = \int_S d^2\mathbf{r}_S \int_S d^2\mathbf{r}'_S \chi_i^*(\mathbf{r}_S) G_0^{-1}(\mathbf{r}_S, \mathbf{r}'_S) \chi_j(\mathbf{r}'_S) \quad (2.61)$$

$$F_{ij} = \int_S d^2\mathbf{r}_S \int_S d^2\mathbf{r}'_S \chi_i^*(\mathbf{r}_S) \frac{\partial G_0^{-1}(\mathbf{r}_S, \mathbf{r}'_S)}{\partial \epsilon} \chi_j(\mathbf{r}'_S) \quad (2.62)$$

$$O_{ij} = \int_I d^3\mathbf{r} \chi_i^*(\mathbf{r}) \chi_j(\mathbf{r}). \quad (2.63)$$

The integrals in (2.60) are contained within I, with the extra derivative term in (2.60) ensuring Hermiticity.

The Hamiltonian, as usual, can be written as

$$H = -\frac{1}{2} \nabla^2 + V_{\text{eff}}(\mathbf{r}) \quad (2.64)$$

where the effective one-electron potential felt by the electron consists of the nuclear potential, the electrostatic potential due to the other electrons (the Hartree potential, $V_H(\mathbf{r})$), and the local exchange-correlation potential $V_{xc}(\mathbf{r})$. The basis functions χ_i are chosen so that they extend beyond S , providing variational freedom to describe both the amplitude and derivative over S .

Rather than solve for the wavefunction in region I, it is convenient to find the Green's function for the surface region [16] evaluated at E so that the term involving F_{ij} in (2.59) disappears. In matrix form, the Green's function then satisfies

$$(\mathbf{H} + \mathbf{G}_0^{-1} - E\mathbf{O}) \mathbf{G}(E) = \mathbf{I}, \quad (2.65)$$

where $G(\mathbf{r}, \mathbf{r}'; E)$ is given in terms of matrix elements by

$$G(\mathbf{r}, \mathbf{r}'; E) = \sum_{i,j} G_{ij}(E) \chi_i(\mathbf{r}) \chi_j^*(\mathbf{r}'). \quad (2.66)$$

From the Green's function, the local density of states [17] can now be written as

$$n(\mathbf{r}, E) = \frac{1}{\pi} \Im G(\mathbf{r}, \mathbf{r}; E + i\delta) \quad \mathbf{r} \in I \quad (2.67)$$

from which the charge density can be found by integrating up to the Fermi energy

$$\rho(\mathbf{r}) = \frac{2}{\pi} \int^{E_F} dE \Im G(\mathbf{r}, \mathbf{r}; E + i\delta), \quad (2.68)$$

where the factor of 2 allows for spin. We can now go to self-consistency, and for the particular application of calculating the surface electronic structure of metals, the efficient screening means that we need only go to self-consistency in region I.

The embedding method for surfaces has been further advanced by Ishida [18, 19], using a new approach for determining the embedding potential over a convenient flat interface. With this approach a buffer region is used to avoid cutting muffin tin spheres, and by adding a cap (a part of the muffin tin sphere cut by a plane) onto the surface region, and removing a similar cap on the substrate side, this has the effect of allowing a full solution within the muffin tins overlapping the embedding plane.

2.4.1 Applications of Embedding

Most surface electronic structure calculations use the supercell method in order to retain periodicity in the surface normal direction. This is so that conventional bulk codes can be used, which now consist of periodic layers parallel to the surface. This supercell (typically 5–20 atomic layers thick) is useful in that conventional bulk codes can be used for its wavefunction solution and has proven useful in the calculation of surface energies, atomic geometry, and surface electronic structure [20]. However, limitations are imposed on this method due to the finite number of layers, in particular when bulk solutions impose an important contribution to surface properties. When these features, such as surface states, are important, the supercell approximation is inadequate for comparison with experiment [20]. This is where the embedding method is deemed most appropriate for surface electronic structure calculations.

Recently, embedding has been used for the electronic structure calculations of large molecules [21]. The partitioning of space which the embedding method allows, can be used to split the molecules into component parts, but still retains information from the remainder of the molecule.

2.5 Computing within the Jellium Model

It is sometimes convenient to use the jellium model for a metal surface. In this model the nuclear lattice is replaced with a smooth background positive charge density n , in the potential of which the electrons

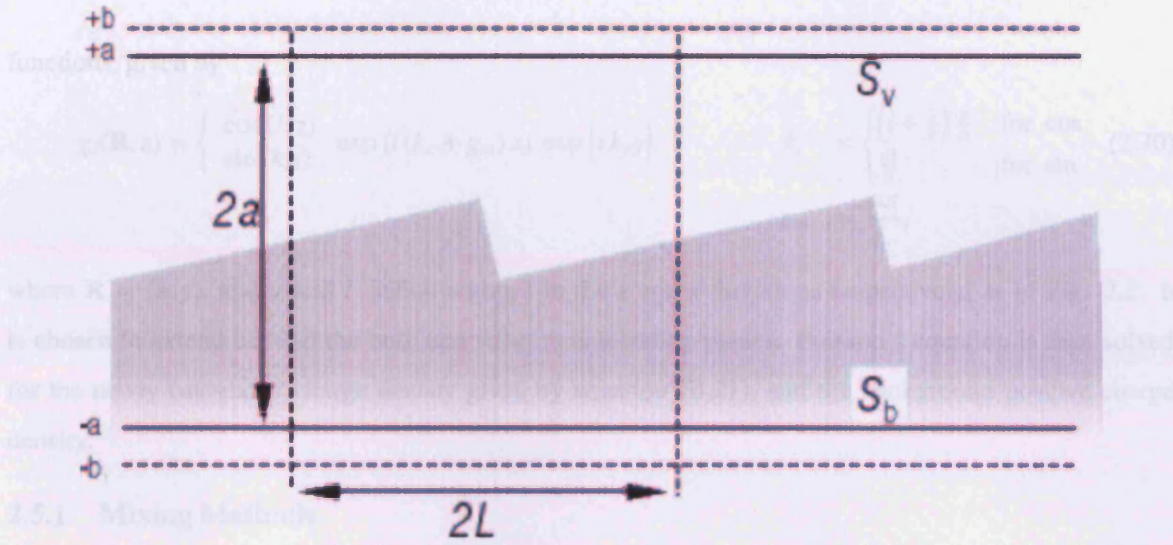


Figure 2.2: The surface embedded region for a jellium stepped surface. The embedding planes for both bulk S_b and vacuum S_v are shown. Region I is the near surface region between S_b and S_v .

are free to move. At the surface the background charge stops abruptly so that

$$\rho_b(z) = \begin{cases} n & z \leq z_s \\ 0 & z > z_s \end{cases} \quad (2.69)$$

where n is found from the *real* material ionic charge density, z is the displacement normal to the surface, and directed away from the bulk and z_s is the position of the surface / vacuum interface. For a stepped surface, as given in Fig. 2.2, z_s is dependent on the surface parallel position, and is described by a sawtooth function. Details of the exact function are given in Appendix B. In the embedding method, the Schrödinger equation for the electronic charge density is then solved to self-consistency within this free electron model between embedding planes placed within the bulk and vacuum some distance away from the surface.

As with any self-consistent procedure, the cycle of solving the Schrödinger equation followed by solving Poisson's equation is needed. Starting from an initial, *guessed* solution for the potential at the jellium surface, the charge density is calculated using the Schrödinger equation. In turn, a new potential is created from the solution of Poisson's equation for the electron density plus the positive jellium background. With appropriate mixing of the effective potential between iterations, this procedure is continued until some pre-defined self-consistent limit has been reached. The details of the initial conditions used in the jellium model are given in Appendix B.

Having constructed the initial potential of the stepped jellium system the first iteration for solution of the self-consistent procedure can be started. This involves finding the Green's function in (2.66) using the initial potential $V(x, z)$ of (B.2), with a suitable basis χ . For this model we choose free-electron

functions, given by

$$\chi_i(\mathbf{R}, z) = \begin{cases} \cos(k_i z) & \exp\{i(k_x + g_m)x\} \exp\{ik_y y\}. \\ \sin(k_i z) & \end{cases} \quad \begin{aligned} k_i &= \begin{cases} \left(i + \frac{1}{2}\right) \frac{\pi}{b} & \text{for cos} \\ \frac{\pi i}{b} & \text{for sin} \end{cases} \\ g_m &= \frac{m\pi}{L}, \end{aligned} \quad (2.70)$$

where $\mathbf{R} = \{x, y\}$, and a and L define region I in the z and x directions respectively, as in Fig. 2.2. b is chosen to extend beyond the bulk and vacuum embedding planes. Poisson's equation is then solved for the newly calculated charge density given by equation (B.21), and the background positive charge density.

2.5.1 Mixing Methods

The type of mixing used is an important consideration for the rate of convergence of the charge density in the self-consistent calculation. Within the jellium model we use simple mixing, whereby the newly calculated potential is mixed linearly with that from the previous iteration, i.e.

$$V_{ij}^n = A V_{ij}^{n-1} + (1 - A) V_{ij}^{\prime n-1} \quad (2.71)$$

where V_{ij}^n is the input potential matrix element for iteration number n , and $V_{ij}^{\prime n}$ is the output potential matrix element calculated from the charge density for the same iteration. A is the fractional mixing. Simple mixing is convenient and easy to implement, but a small value of A must be used to ensure stability, which decreases the rate of convergence, of course.

A more standard mixing routine is that of Broyden mixing [22], in which the potentials (or charge densities) from a number of previous iterations are taken into consideration, and are mixed according to some weighting determined by the Broyden parameters. This is used in later calculations.

2.6 Computing with Atomic Structures

Although jellium is still useful for some applications, realistic calculations must involve the atomic structure. However, the electronic wavefunctions are highly oscillatory within the atomic core and methods must be found to deal with this problem.

One such method is to replace the potential resulting from the nucleus and core electrons with a shallow *pseudopotential* [13]. This is constructed in such a way that valence electrons are scattered by the pseudopotential in the same way as by the actual potential. Outside the core, the pseudopotential is the same as the actual potential, and consequently the pseudo-wavefunction is the same as the actual wavefunction in the outer region. The advantage of the pseudopotential is that the valence electrons can be modelled using a plane-wave basis set, since the rapid oscillations of the electron wavefunctions are

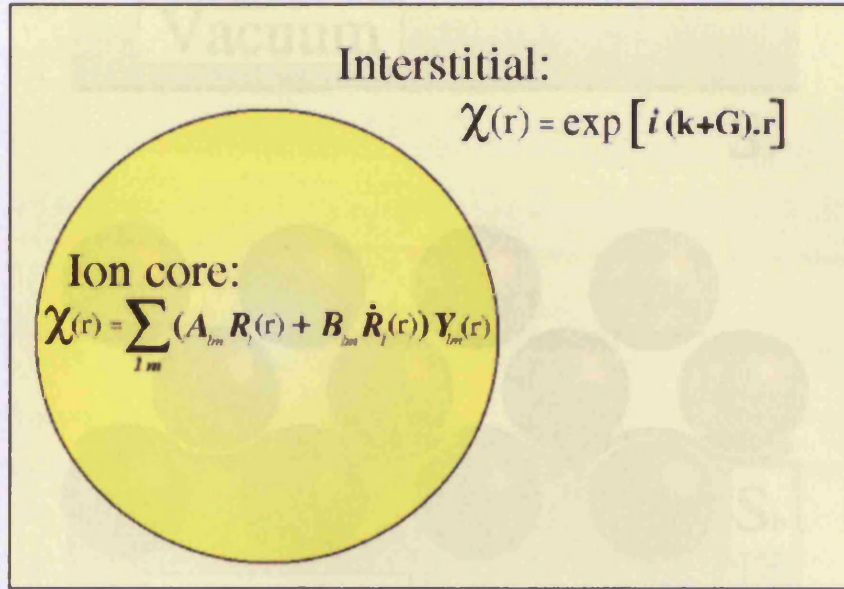


Figure 2.3: Partitioning of space within the *linearised-augmented plane wave* method. Plane waves are used in the interstitial region, whereas radial solutions to the Schrödinger equation are used within the spherical region of the ion core.

removed due to the shallow pseudopotential. This method is widely used and implemented in codes such as *SFHingX* and *FHI98PP* [23].

Another model, this time an all-electron method, was developed by Slater in 1937 [24], and is called the *augmented plane wave* method. This is the basis for the more modern and sophisticated *linearised-augmented plane-wave method* (LAPW) [25, 26] which is used throughout all atomistic calculations in this thesis.

2.6.1 Linearised Augmented Plane-Waves

In the LAPW method, space is partitioned into muffin tins containing the ion core and the interstitial region (Fig. 2.3) [5]. Within the interstitial region, the basis functions are given by plane-waves,

$$\chi_N^{\text{int}}(\mathbf{r}) = \sqrt{\frac{2}{AL}} \exp\{i(\mathbf{k} + \mathbf{G}) \cdot \mathbf{R}\} \sin(p_n z), \quad (2.72)$$

where $p_n = \frac{n\pi}{L}$ with $(n \geq 1)$, $N = \{\mathbf{G}, n\}$, and $\mathbf{R} = \{x, y\}$. A is the area of the 2-dimensional surface unit cell and L is the distance between the embedding planes. A plane-wave expansion is convenient since the potential in this region is rather flat: plane-waves are solutions of the Schrödinger equation in a constant potential, and so are a natural choice.

The basis functions inside the muffin tins consist of radial solutions of the Schrödinger equation,

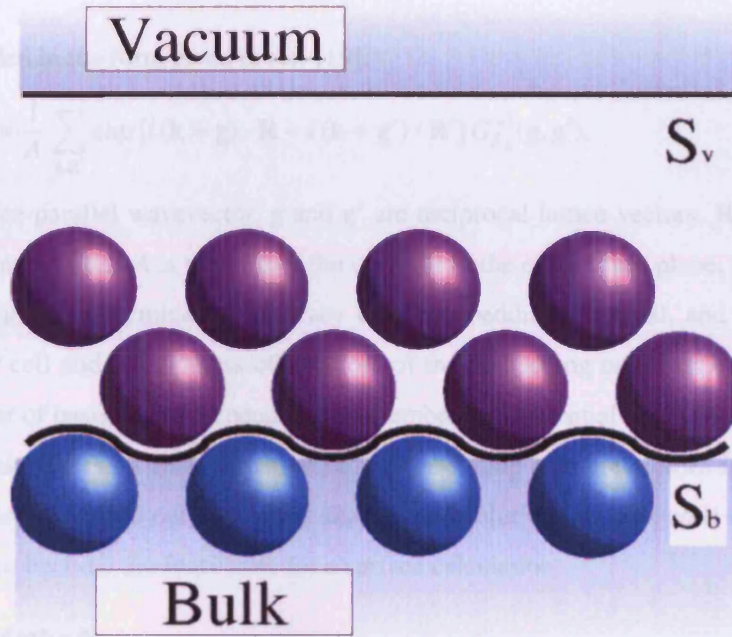


Figure 2.4: The surface embedded region. An atomistic surface with embedding planes for both bulk S_b and vacuum S_v . Region I is the near surface region between S_b and S_v .

motivated by the strongly varying, but near-spherical potential and wavefunctions:

$$\chi_N^{\text{ion}}(\mathbf{r}) = \sum_l \sum_m (A_{l,m} R_l(\mathbf{r}) + B_{l,m} \dot{R}_l(\mathbf{r})) Y_{l,m}. \quad (2.73)$$

The basis function $\chi_N^{\text{ion}}(\mathbf{r})$ is given in terms of the radial solution of the Schrödinger equation $R_l(\mathbf{r})$ and its energy derivative $\dot{R}_l(r) (= \frac{\partial R_l(\mathbf{r})}{\partial E})$ inside the muffin-tin, using a standard scalar-relativistic treatment [27]. The coefficients A_{lm} and B_{lm} are found by matching (2.72) and (2.73) over the muffin tin boundary in amplitude and derivative [5, 16]. The LAPW basis functions are highly efficient, and typically 100 basis functions per atom is adequate.

2.6.2 Plane-Wave Expansion of the Embedding Potential

An important consideration for any embedding calculation is the accuracy of the embedding potential G_0^{-1} . Further details of embedding potential accuracy are discussed in the next chapter. However, we shall briefly mention areas of concern in surface calculations. Figure 2.4 shows a typical set-up of a low Miller index surface calculation. The analytical vacuum embedding potential [19]

$$G_{S_v}^{-1}(\mathbf{g}, \mathbf{g}') = -\frac{i}{2} \delta_{\mathbf{g}, \mathbf{g}'} \sqrt{2(\epsilon - \epsilon_v) - |\mathbf{k} + \mathbf{g}|^2} \quad (2.74)$$

is placed on S_v . ϵ_v denotes the vacuum energy. The bulk embedding potential $G_{S_b}^{-1}$ is placed on S_b , and is determined prior to the surface calculation from a self-consistent bulk calculation. The bulk embedding

potential is expanded in the form given in ref. [19]:

$$G_{S_b}^{-1}(\mathbf{R}, \mathbf{R}') = \frac{1}{A} \sum_{\mathbf{g}, \mathbf{g}'} \exp [i(\mathbf{k} + \mathbf{g}) \cdot \mathbf{R} - i(\mathbf{k} + \mathbf{g}') \cdot \mathbf{R}'] G_{S_b}^{-1}(\mathbf{g}, \mathbf{g}'), \quad (2.75)$$

where \mathbf{k} is a surface-parallel wavevector, \mathbf{g} and \mathbf{g}' are reciprocal lattice vectors, \mathbf{R} and \mathbf{R}' are position vectors over the plane S_b and A is the area of the unit cell of the embedding plane. The number of basis functions will obviously determine the accuracy of the embedding potential, and depends on the size of the surface unit cell and the richness of structure of the embedding potential itself. These concerns increase the number of basis functions needed for the embedding potential when dealing with small spacings between atomic layers, as more structure in the embedding potential comes from adjacent atomic layers. These concerns are laid out in the next chapter, and solutions are proposed when the embedding potential is found to become too inaccurate for a surface calculation.

2.6.3 Mixing Methods

In the self-consistent procedure, the LAPW calculation iterates in terms of the *charge density*. In the case of the jellium model discussed previously, the *potential* is mixed between iterations, but the principle that both of these quantities are mixed in some way between iterations, is the same. The initial charge density and potential for the LAPW surface calculation is calculated from the superposition of single atom charge densities. The Schrödinger equation is then solved using the embedding methodology, and Broyden mixing [22] of the input and output charge densities obtains the new input charge for the following iteration. In the next iteration, Poisson's equation for that charge density is solved, and the cycle continues until convergence is achieved.

The Broyden method of mixing is a non-linear routine, mixing charge densities over a number of previous iterations, typically up to eight, after which the process is re-initialised. The benefit of this method is a greater convergence rate over simple mixing routines, but a small fractional mixing is still used in order for the convergence to remain stable.

A further feature of Ishida's embedding code is the use of the full potential of the ion core in the interstitial potential calculation [28, 29]. This is implemented in the Poisson solution, by replacing the radial wavefunction inside the muffin-tin by a plane-wave expansion of a *pseudocharge*, possessing the same multipole moments as the radial wavefunction. The corresponding electrostatic potential can then be found directly, and corresponds to the full solution of Poisson's equation outside the muffin-tins. The solution within each muffin tin is found by integrating Poisson's equation with the full muffin-tin charge density, with the boundary conditions that the potential matches onto the interstitial value.

2.6.4 Static Electric Fields

One emphasis of this thesis is the study of surfaces and defective surfaces in static electric fields. The calculations in Chapters 7 and 8 deal with electrified interfaces to investigate screening and field emission properties of various surfaces. An electric field F is applied perpendicular to the surface by placing a notional charge density σ at the vacuum embedding plane S_v (Fig. 2.4). The electric field related to this charge density is given by

$$F = -4\pi\sigma. \quad (2.76)$$

Here, σ is defined as the charge density in atomic units. The convention used is that a positive value of σ indicates a positive charge density at S_v , inducing a negative field of $-4\pi\sigma$ a.u. The field is in the direction normal to the surface.

2.7 The Work Function

Throughout this thesis a large emphasis is placed on work function values. It is crucial therefore to explicitly define the work function and how it is calculated using the embedding method. The energy needed to extract an electron has its roots in the energy of the occupied electrons, which is a bulk property, but the barrier to electron removal is also strongly dependent on the surface dipole. This surface dipole is face dependent, which means that extra care is needed in the work function definition. Taking this into account, the work function of a metal can be defined as the energy required to remove an electron from the Fermi energy of the metal to just outside the surface. The term “just outside” means that the work function is truly face dependent if the electron-metal distance is small compared to the material dimensions, but remains large on the atomic scale [30].

For practical purposes, the work function calculation within the embedding method follows this definition by considering the difference in the Hartree potential at the vacuum embedding plane $V_H^{S_v}$, and the metal Fermi energy,

$$\Phi = V_H^{S_v} - E_F. \quad (2.77)$$

At the vacuum embedding plane the Hartree potential has reached its asymptotic limit and can therefore be considered far from the surface on the atomic scale.

Bibliography

- [1] S.L. Altmann, *Band Theory of Metals : the Elements* Oxford University Press, Pergamon (1970).
- [2] R.O. Jones and O. Gunnarsson, *Rev. Mod. Phys.* **61**, 689 (2001).
- [3] J. E. Inglesfield, *J. Phys. C: Solid State Phys.* **14**, 3795 (1981).
- [4] A. Zangwill, Cambridge University Press, Cambridge (1964).
- [5] D.J. Singh, *Planewaves, Pseudopotentials, and the LAPW method*, Kluwer Academic, Norwell (1994).
- [6] J. Callaway, *Quantum Theory of the Solid State*, Kluwer Academic Press (1976); and reference within: M. Born and J.R. Oppenheimer, *Ann. Phys. (Leipzig)* **84**, 457 (1927).
- [7] P. Hohenberg and W. Kohn, *Phys. Rev.* **136**, B864 (1964).
- [8] Walter Kohn shared the 1998 Nobel Prize for Chemistry for his development of density functional theory. His early work on DFT was reported in two publications with P. Hohenberg [7] in 1964 and Lu J. Sham [9]. Although W. Kohn is not a chemist, the DFT he describes has many widespread applications in this field, allowing for the ground state description of the electronic properties of atoms and molecules. DFT calculations are now used to predict and model static models of atoms/molecules as well as chemical reactivity in the chemistry and biochemistry field. John A. Pople shared the 1998 Nobel Prize for Chemistry for his unrelated work on the “development of computational methods in quantum chemistry”.
- [9] W. Kohn and L. J. Sham, *Phys. Rev.* **140**, A1133 (1965).
- [10] J.P. Perdew and A. Zunger, *Phys. Rev. B* **23**, 5048 (1981).
- [11] D.M. Ceperley and B.J. Alder, *Phys. Rev. Lett.* **45**, 566 (1980).
- [12] M. Fuchs and X. Gonze, *Phys. Rev.* **65**, 235109 (2002).
- [13] J.M. Thijssen, *Computational Physics* Oxford University Press, Cambridge (1999).
- [14] J.P. Perdew and Y. Wang, *Phys. Rev. B* **33**, 8800 (1986).
- [15] A.D. Becke, *J. Chem. Phys.* **98**, 1372 (1992).
- [16] G.A. Benesh and J.E. Inglesfield, *J. Phys. C: Solid State Phys.* **17**, 1595 (1984).
- [17] V. Heine, *Solid State Physics*, Vol. **35**, 1 (1980).

- [18] H. Ishida, Surf. Sci. **388**, 71 (1997).
- [19] H. Ishida, Phys. Rev. B **63**, 165409 (2001).
- [20] J.E. Inglesfield, Comput. Phys. Commun. **137**, 89 (2001).
- [21] O.R. Davies and J.E Inglesfield, Phys. Rev. B **69**, 195110 (2004).
- [22] C.G. Broyden, Math. Computing. **19**, 577 (1965).
- [23] M. Fuchs and M. Scheffler, Comp. Phys. Comm. **119**, 67 (1999).
- [24] J.C. Slater, Phys. Rev. **51**, 846 (1937).
- [25] D.D. Koelling and G.O. Arbman, J. Phys. F: Metal Phys. **5**, 2041 (1975).
- [26] O.K. Anderson, Phys. Rev. B **12**, 3060 (1975).
- [27] D.D. Koelling and B.N. Harmon, J. Phys. C: Solid State Phys. **10**, 3107 (1977).
- [28] E. Wimmer, H. Krakauer, M. Weinert and A.J. Freeman, Phys. Rev. B **24**, 864 (1981).
- [29] M. Weinert, E. Wimmer and A.J. Freeman, Phys. Rev. B **26**, 4571 (1982).
- [30] N.W. Ashcroft, N.D. Mermin, *Solid State Physics*, Saunders College Publishing, p. 354 (1976).

CHAPTER 3

Surface Geometry

Contents

3.1	Metal Substrates and the Surface Miller Index	30
3.1.1	Microfacet Notation	32
3.2	Stepped Surfaces and Embedding	33
3.3	Surface Relaxation and Reconstruction	35
	Bibliography	38

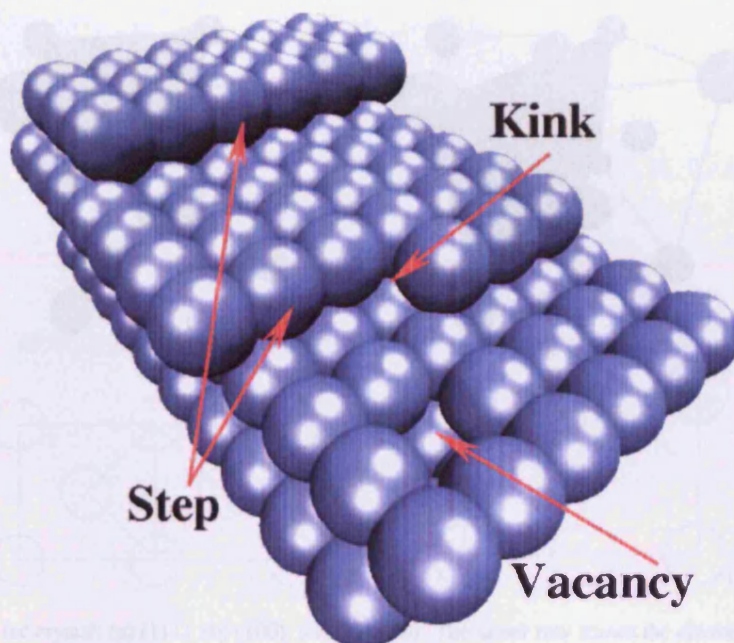


Figure 3.1: Various surface defects on an fcc crystal. Shown are steps, kinks and vacancies.

The properties of any surface, such as reactivity or work function, depend not only upon the chemical properties of the material but also on the surface structure. This chapter considers some concepts and nomenclature of surface structure and gives a brief account of surface Miller indices, defects, relaxation and reconstruction at metal surfaces.

3.1 Metal Substrates and the Surface Miller Index

Many substrates such as metals and semiconductors can be grown as single crystals of considerable size (of the order of 1 cm or more in diameter) [1]. In nature though, most substrates are not single crystals, and the materials possess defects such as grain boundaries, dislocations and vacancies. These defects can be transferred to the surfaces, which in turn possess defects such as steps, kinks and vacancies [2] (Fig. 3.1). In this thesis we shall mainly be concerned with idealised surfaces, either flat surfaces or surfaces with a regular array of steps. In Chapters 4 and 5, reconstructed and relaxed surfaces are considered, due to their significance in adsorbate bonding.

The possible surfaces can be conveniently described by the surface Miller indices [3]. The different crystallographic planes are revealed by slicing through single crystals at different angles. The Miller index of a surface of a cubic crystal, with unit vectors **a**, **b**, and **c**, are described by considering the intersection of the surface plane on each axis of the unit-cell, xa , $y\mathbf{b}$, and $z\mathbf{c}$. The reciprocal quantities $1/x$, $1/y$, and $1/z$ are transformed to the lowest integer values of the same ratio and are termed the surface Miller index (hkl). The Miller indices are also convenient because they describe the vector normal to the

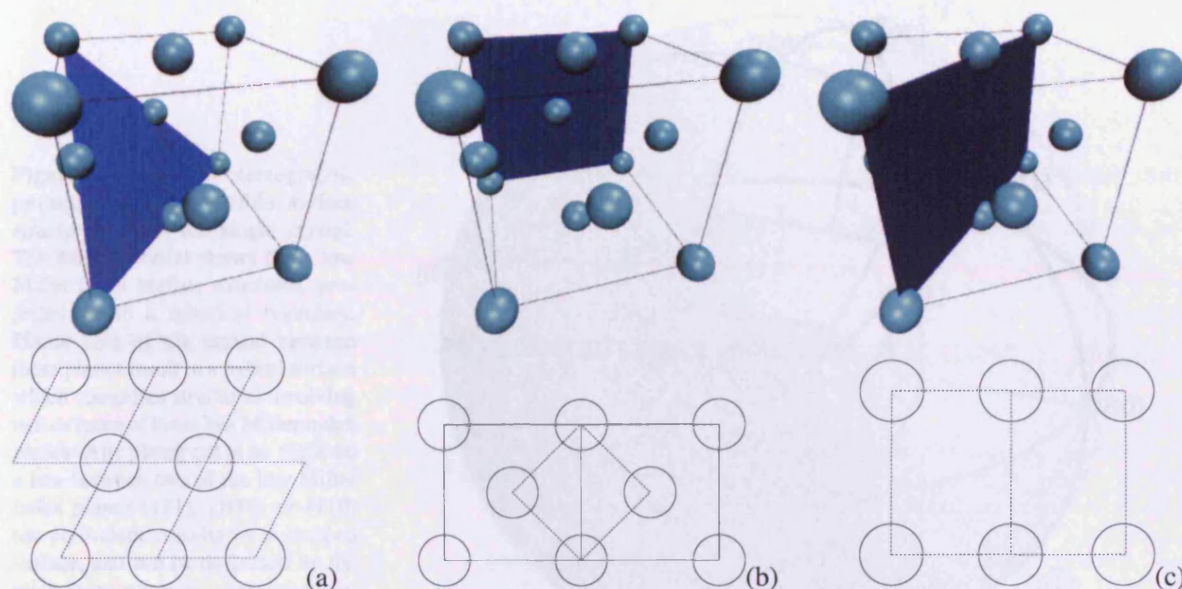


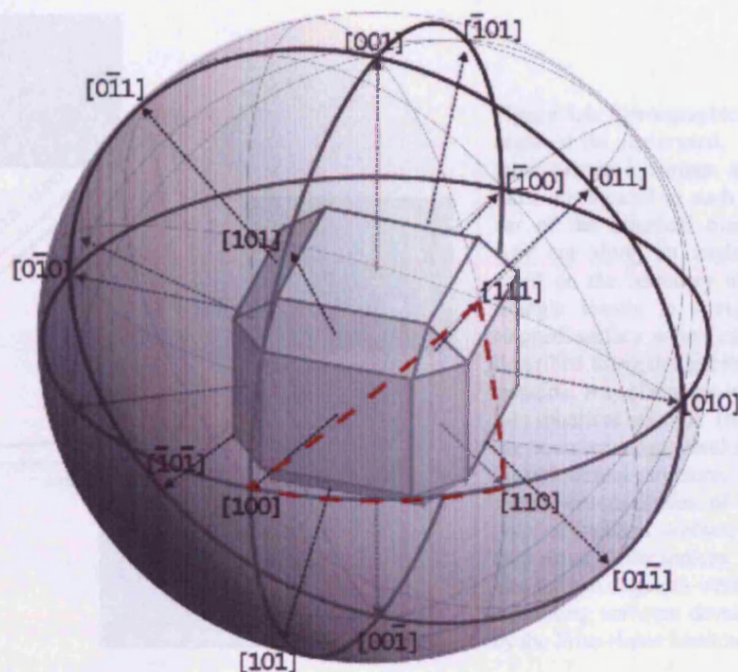
Figure 3.2: Low Miller index planes of the fcc crystal; (a) (111), (b) (100), and (c) (110). The upper row shows the cleavage plane for the surface within the lattice unit cell, the lower row gives a plan view of the corresponding surface plane.

cutting plane, denoted with square brackets $[hkl]$. Figure 3.2 demonstrates different cutting planes for the face-centred cubic Bravais lattice. The cut in Fig. 3.2a gives rise to a (111) surface, Fig. 3.2b to (100), and Fig. 3.2c to (110). Here, each component of the Miller index (h,k,l) gives the relative x -, y -, and z - components of the surface normal vector. These three surfaces have the smallest non-equivalent Miller indices for the fcc crystal structure, and are here termed *flat* surfaces. For the most part, this thesis considers surfaces on fcc metals.

The three surface structures of the fcc crystal shown in Fig. 3.2 are clearly not the only surfaces obtainable by cleaving the crystal. For instance, cutting an fcc single crystal in the x - y plane results in a (001) surface (equivalent structures are also found for the x - z and y - z planes (Fig. 3.2b)). But if this plane has, say, a small z - component, the resulting surface would be a stepped surface; for small tilts from the original x - y plane, this would consist of (001) terraces, separated by equally spaced rows of (011) steps. By increasing the angle of tilt, a surface with a greater step density would result.

All possible surface structures can be conveniently visualised using a stereographic projection (Fig. 3.3). This projection shows which surface structure results from cutting an fcc single crystal for any given plane. For the sake of simplicity the diagram only highlights the flat surfaces. Throughout the spherical projection, many equivalent structures occur at different planar cuts. Since, for the moment, we are only interested in flat and stepped surfaces, the diagram can be reduced to show how a surface can be made up of separate facets of the low Miller index surfaces already described. This representation is called the stereographic triangle [4] (Fig. 3.4), and from this diagram the idea of a microfacet notation

Figure 3.3: Spherical stereographic projection of the possible surface structures of an fcc single crystal. The central crystal shows three low Miller index surface structures, projected on to a spherical boundary. Planar cuts of the crystal between these planes result in a hybrid surface which comprises structures involving two or more of these low Miller index planes. Any planar cut at an angle on a line between two of the low Miller index planes (111), (100), or (110) (or equivalent) results in a stepped surface, and can be described by the microfacet notation. Any other cut would result in a kinked surface. The diagram highlights the stereographic triangle (dashed line).



[5] is introduced.

3.1.1 Microfacet Notation

As mentioned, a stepped surface is a hybrid of two or more low Miller index surface facets, such as (100) and (111). For a well-defined stepped surface, the microfacet notation is based on the ratio of these steps and terraces within one primitive unit cell of the stepped structure. These surface structures can be conveniently represented by the stereographic triangle (Fig. 3.4), which is the planar representation of the spherical triangle having corners at the (100), (110), and (111) faces. A planar cut of the fcc single crystal in a direction between any of these primitive faces results in a stepped surface. So in the microfacet notation, a cut between the (100) and (110) faces gives a structure of $n(100) \times (110)$, or alternatively $n(110) \times (100)$ where n is the integer ratio of the length of terrace and step facets, dependent on the angle of the cut. For example, on the (510) surface (Fig. 3.4) the terraces possess a (100) geometry and the steps a (110) geometry in the ratio of 3 : 1. This gives a microfacet notation of $3(100) \times (110)$. Likewise, the (430) surface has (110) terraces and (100) steps in the ratio of 3 : 1. This now gives the microfacet notation of $3(110) \times (100)$.

These examples clearly show a distinct step-terrace structure. If however, the planar cut of the fcc crystal gives a step and terrace of similar size, then it is difficult to distinguish between the two. This is known as the turning point and occurs at high step densities. In Fig. 3.4 the turning point is represented by the break in the outer lines of the diagram. As an example, the turning point between the (100) plane

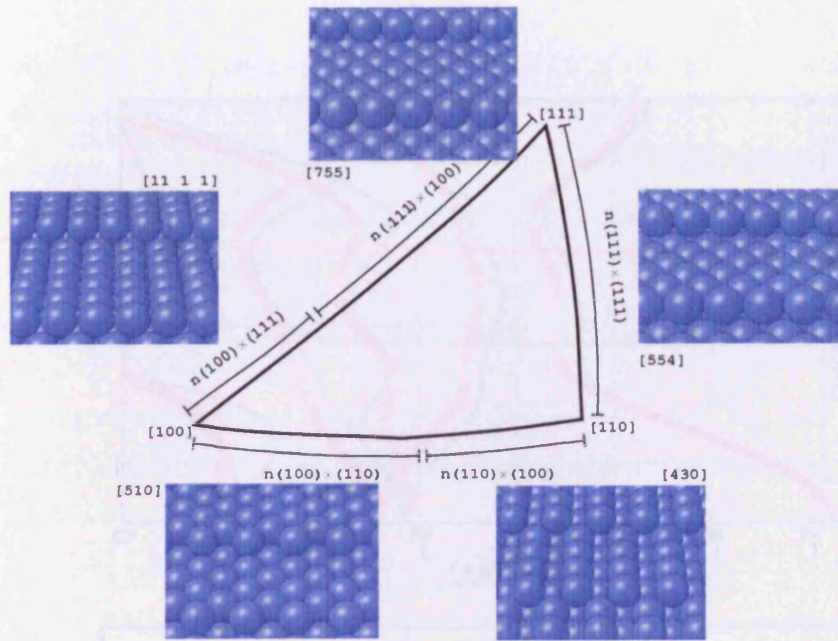


Figure 3.4: Stereographic triangle of the fcc crystal. The three primitive surface structures are located at each corner of the spherical triangle. Any cut along an angle located on the boundary of the triangle results in a regular stepped surface which can be described using the microfacet notation. Any planar cut *within* the spherical triangle (not at the boundary edge) results in a kinked surface structure. Also shown are examples of each type of stepped surface, and their usual Miller indices.

The surface diagrams were created using software developed by the Fritz-Haber Institute [6].

and the (111) plane is the (311) surface.

The microfacet notation is a convenient way of describing stepped surfaces of a regular nature. It gives very clearly both the structure of the terrace and step, and the size of the terrace in terms of the number of low Miller index units. Ideally, the calculations in this thesis would be based on vicinal surfaces, in which the surface normal direction is tilted slightly from low index planes. However, a constraint is imposed on the surface when performing calculations using the embedding method. This drawback, together with a possible solution, is discussed in the next section.

3.2 Stepped Surfaces and Embedding – Approximations and Justification

Since we are going to investigate high Miller index, stepped surfaces, the surface unit cell has a large area, but with a much reduced spacing between atomic layers. This means that when the embedding potential is calculated over a plane between atomic layers, more atoms must cross this plane. This results in a rapidly varying embedding potential, and with the increased surface area, a greater plane wave basis set is needed to expand the embedding potential. This in fact leads to a point, for increasing terrace length of the vicinal surface, where the embedding potential cannot be described accurately. In our work, and with our computing resources, it is found that the highest Miller indices feasible for a vicinal surface

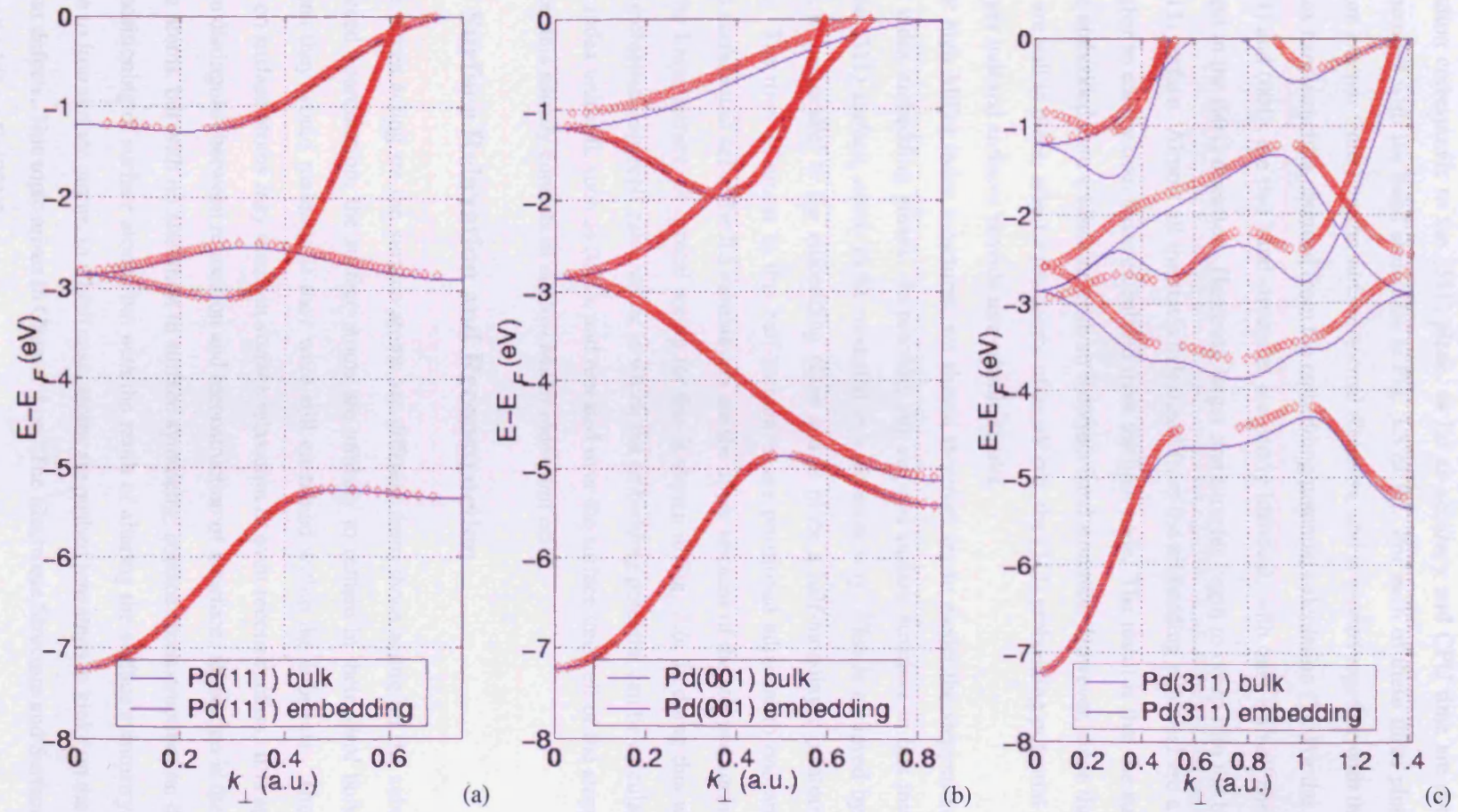


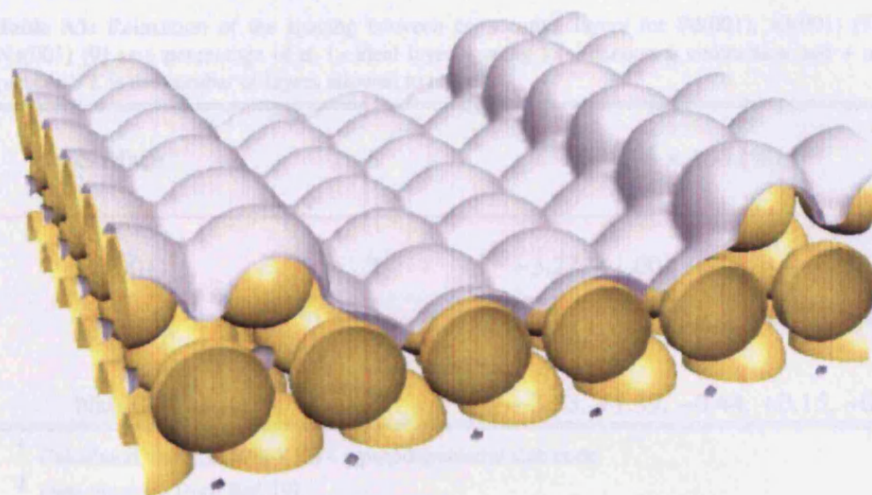
Figure 3.5: Comparison of the real part of the complex band structure of Pd obtained from the embedding potential calculation and the bulk band structure along equivalent directions. The real part of the complex band structure is shown as red circles, and the bulk band structure is represented as a solid line. Wavevector directions are along the surface normal direction as indicated for each plot.

calculation corresponds to the (311) plane, as far as accuracy and CPU time are concerned. This is demonstrated with the band structures in Fig. 3.5 of Pd. For each of these three plots, the bulk band structure extends from Γ in the surface normal direction, and is plotted together with the real part of the complex band structure obtained from the embedding potential calculation [7]. For the low index planes of (111) and (001), the two band structures are nearly identical, with only a small energy difference in a d -band in the (001) direction. However, larger inaccuracies begin to creep into the band structure for the (311) surface. Almost all the states calculated from the embedding potential are a few tenths of an eV higher in energy than those calculated from the bulk code. The result is that the surface calculation will be embedded onto a substrate with an incorrect band structure. However, since the structure of the bands are still in place, albeit a few tenths of an eV out, the (311) embedding potential can still be used, but larger indexed surfaces provide unworkable results.

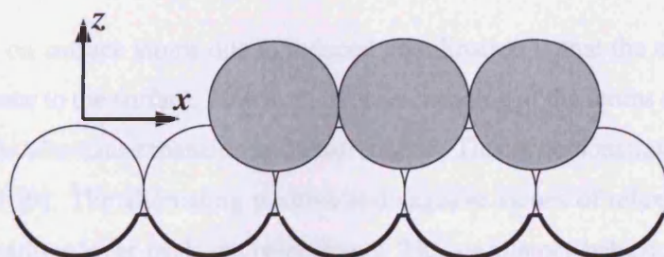
For high Miller index structures, we should therefore try to model the stepped surface using low Miller index embedding planes. In practice, any stepped surface structure in this investigation, other than the (311) surface, needs to be modelled in a different way. This is achieved by considering the terrace to be parallel to the embedding plane and to place a half-monolayer of atoms on top of this terrace. The rows of atoms in this half-monolayer are positioned adjacent to one another within the chosen surface unit cell. The 0.5 monolayers are the upper terraces of the stepped surface, with the next layer the lower terrace. A typical set-up for this is shown in Fig. 3.6. In doing this we are left with a two-dimensional supercell calculation, in which the embedding potential can be calculated over one low Miller index unit cell, such as (001), and repeated over the surface unit cell of the stepped structure. In practice, this usually consists of six low Miller index unit cells.

3.3 Surface Relaxation and Reconstruction

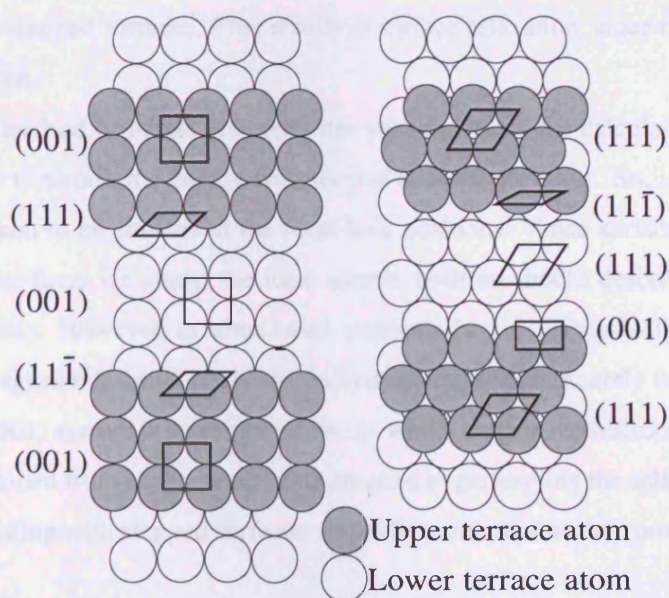
As the forces acting on the surface atoms are different from those acting on the substrate atoms due to reduced coordination, the surface atoms are unlikely to remain in their *ideal* bulk positions – the positions they would maintain if they were still contained within the substrate. The different forces acting on surface atoms may result in surface relaxation or even reconstruction. It is appropriate at this point to distinguish between relaxation and reconstruction of a surface: relaxation is the repositioning of surface atoms, but with no alteration in surface symmetry; surface reconstruction, on the other hand, is the repositioning of surface atoms, but *with* the result of altering the surface symmetry. The result may even be to *lose* surface atoms, in which case, atoms are pushed into steps or kinks on the surface, causing irregular defects. This topic arises in Chapter 4 on “The Electronic Structure and Surface Reconstruction of Adsorbed O on Cu(001)”.



(a)



(b)



(c)

Figure 3.6: Stepped surface structure avoiding high Miller index planes. Islands of rows of atoms are equally spaced over the substrate. This surface layout avoids the high Miller index surface planes, and so the accuracy of the embedding plane is not limited by the greater embedding structure. The result is a supercell calculation over many low Miller index surface planes, and the embedding potential retains the accuracy of a single cell calculation. (a) shows charge iso-surfaces of a self-consistent Pd surface, (b) and (c) give side and plan views respectively of similar structures.

Table 3.1: Relaxation of the spacing between consecutive layers for Pd(001), Al(001) [9] and Na(001) [9] as a percentage of d_z (= ideal layer spacing) (– denotes a contraction and + an expansion). L is the number of layers allowed to relax.

Surface	L	$\frac{\Delta z}{d_z} \times 100$ (%)
Pd(001) [†]	3	–3.27, +1.00, –0.18
Al(001) [‡]	10	–0.54, +0.08, –0.01
Na(001) [‡]	10	–3.53, +1.39, –0.44, +0.15, –0.05

[†] Calculated using *SFHHX* [8] – a pseudopotential slab code.

[‡] Data obtained from Ref. [9].

The usual effect on surface atoms due to reduced coordination is that the one-sided forces alter the interlayer spacing close to the surface. However, the layer spacing of the atoms does not simply contract, but usually undergoes alternate expansion and contractions. This is demonstrated for Pd(001) and other surfaces in Table 3.1 [9]. The alternating positive and negative values of relaxation indicate increasing and decreasing relaxations layer-by-layer, respectively. This oscillatory behaviour is an effect of Friedel oscillations in the charge densities near the surface, which is touched upon in Chapter 6 dealing with the jellium model of stepped surfaces. This results in surface relaxation, since two-dimensional surface symmetry is unaffected.

The embedding method of Ishida [10] does not yet implement the calculation of total energy, and so cannot be used to minimise the energy with respect to atom positions. So, in most cases, the atoms at the surface are taken to be situated at the ideal bulk positions. Since surface relaxation is expected to be small for the surfaces we study, the ideal atomic position should describe the properties of the surface quite accurately. However, in some cases, particularly for surfaces with adsorbates, it is found that the surface undergoes relaxation or reconstruction, deviating significantly from the ideal surface. In Chapter 4 the O/Cu(001) system is investigated, one in which surface reconstruction occurs. In this case, atomic positions obtained from experimental data are used in performing the self-consistent calculations. Chapters 7 and 8, dealing with stepped surfaces, use bulk-terminated atomic positions.

Bibliography

- [1] E.M. McCash, *Surface Chemistry*, Oxford University Press (2001), p.3.
- [2] G.E. Rhead, *Surf. Sci.* **68**, 20 (1977).
- [3] J.R. Hook and H.E. Hall, *Solid State Physics (The Manchester Physics Series)*, John Wiley and Sons Ltd (1991).
- [4] G.A. Attard and C. Barnes, *Surfaces*, Oxford University Press (1998), p.17.
- [5] B. Lang, R.W. Joyner and G.A. Somorjai, *Surf. Sci.* **30**, 440 (1972).
- [6] *Java-based web-application developed by the Fritz-Haber-Institute, Berlin*
- [7] D. Wortmann, H. Ishida and S. Blügel, *Phys. Rev. B* **65**, 165103 (2002).
- [8] M. Fuchs and M. Scheffler, *Comp. Phys. Comm.* **119**, 67 (1999).
- [9] U. Landman, R.N. Hill and M. Mostoller, *Phys. Rev. B* **21**, 448 (1980), and references therein.
- [10] H. Ishida, *Phys. Rev. B* **63**, 165409 (2001).
- [11] C.J. Fall, N. Binggeli and A. Baldereschi, *Phys. Rev. B* **65**, 045401 (2001).
- [12] K. Wandelt, *Surf. Sci.* **251**, 387 (1991).
- [13] K. Hermann, B. Gumhalter and K. Wandelt, *Surf. Sci.* **251**, 1128 (1991).

CHAPTER 4

Electronic Structure and Surface Reconstruction of Adsorbed O on Cu(001)

Contents

4.1	The O/Cu(001) Surface	40
4.2	Computational Aspects	43
4.3	Work Function and the Effective Charge	43
4.4	Electronic Structure of Cu(001)-c(2 × 2)-O	45
4.5	Electronic Structure of Cu(001)-(2√2 × √2)R45°-O	53
4.6	Conclusions	61
	Bibliography	64

Chapter 3 introduced the phenomenon of surface relaxation and reconstruction. External effects may also have an influence on atomic repositioning. For instance, applied electric fields can cause reconstruction of Ag(110) [1], Pt(110), and Au(110) [2] surfaces, and atomic or molecular adsorption frequently influences surface structure. This chapter deals with such a reconstruction, where O chemisorbed onto Cu(001) is the cause of a missing row reconstruction. Calculations are based on two phases of the reconstruction, using ideal-terminated, and fully reconstructed geometries according to experimental data [3].

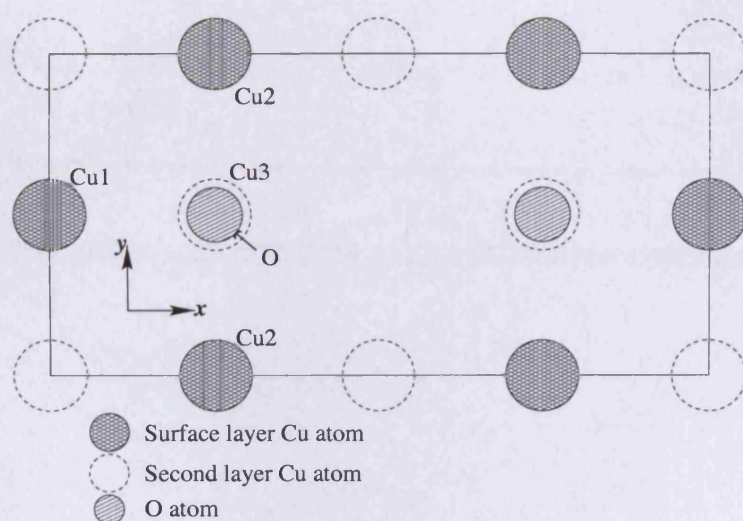
4.1 The O/Cu(001) Surface

It is well known that O adsorption on Cu(001) at 0.5 monolayer coverage has the $(2\sqrt{2} \times \sqrt{2})R45^\circ$ structure with surface reconstruction involving missing Cu rows [4, 5]. However, adsorbed O initially has a $c(2 \times 2)$ structure, with a local coverage of 0.5 monolayer contained within small islands, up to an overall coverage of 0.34 monolayers [3, 6]. After the 0.34 monolayer coverage has been reached the system undergoes the missing row reconstruction and the $(2\sqrt{2} \times \sqrt{2})R45^\circ$ phase is formed.

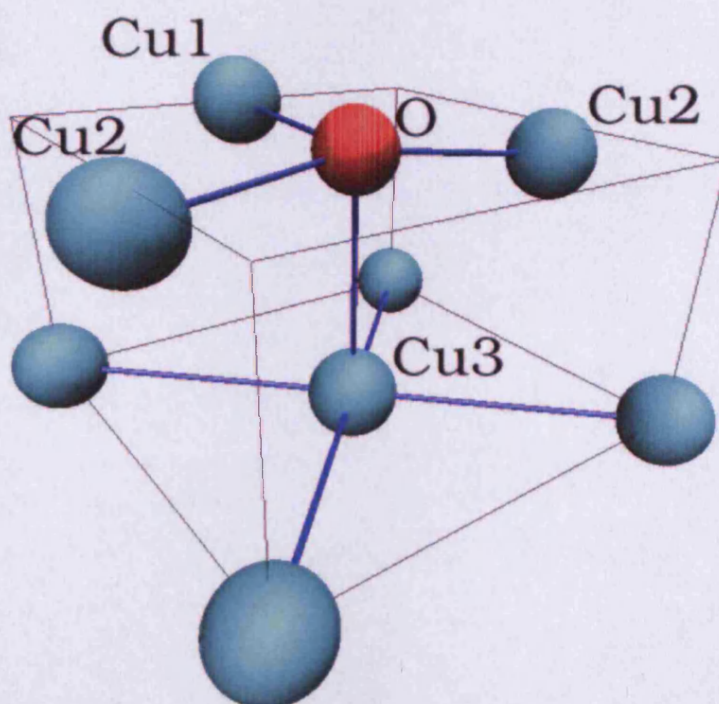
In the Cu(001)- $c(2 \times 2)$ -O phase, the O is chemisorbed in fourfold hollow sites, with the surface Cu atom in essentially bulk-terminated positions. A range of values for the Cu-O inter-layer spacing, $d_{\text{Cu-O}}$, has been obtained experimentally. Surface-extended X-ray-absorption fine-structure (SEXAFS) variously gives $d_{\text{Cu-O}} = 0.94$ a.u. [5], and $d_{\text{Cu-O}} = 1.3$ a.u. [7, 8]. For this reason we perform calculations for a range of $d_{\text{Cu-O}}$ between 1.15 a.u. and 1.7 a.u. which span most of the observed experimental results (and also previous theoretical results [9] which go up to 1.9 a.u.). The full range of $d_{\text{Cu-O}}$ cannot be studied because of restrictions on the radii of the atomic muffin tins which are used to construct the LAPW basis functions. There is a weak dependence of the self-consistent solution on the muffin tin radius of the surface atoms, and to avoid this we use the radii of 1.4 a.u. for O and 2.19 a.u. for the surface Cu atom in all our electronic structure calculations. This gives a lower limit of the $d_{\text{Cu-O}}$ value of 1.15 a.u., which is somewhat larger than the minimum value found from experiment.

Table 4.1: Structural parameters of the Cu(001)- $(2\sqrt{2} \times \sqrt{2})R45^\circ$ -O surface from Woodruff *et al.* [3]. The surface normal distances relative to Cu3 are given for each of the atoms Cu1, Cu2 and O. The surface parallel displacements δx_{O} and δx_{Cu2} are relative to the ideal bulk-terminated positions of the atom in the x -direction as defined in Fig. 4.1. All values are given in atomic units (a.u.).

Cu1	4.04
Cu2	3.55
O	3.87
δx_{O}	0.075
δx_{Cu2}	0.55



(a)



(b)

Figure 4.1: Structure of the Cu(001)-(2 $\sqrt{2} \times \sqrt{2}$) R45°-O surface showing (a) a plan view of the ideal bulk-terminated surface on the (001) plane, and (b) a perspective view of the structure as proposed in [3], showing the local environment of the O atom. Notice in (a) the missing Cu atom in the top layer, which if present, would form an ideal $c(2 \times 2)$ structure. All lines between atoms are guides for the eye and do not represent the bonding at the surface.

The second system is the missing row reconstructed surface of $\text{Cu}(001)-(2\sqrt{2} \times \sqrt{2})\text{R}45^\circ\text{-O}$. For this phase, two separate local structures are investigated in detail. Firstly, we take bulk-terminated Cu atoms, with every fourth row removed (Fig. 4.1a), and with $d_{\text{Cu-O}} = 1.5 \text{ a.u.}$, comparable to the values taken in the $c(2 \times 2)$ structure. Secondly, we study a locally reconstructed model of the $(2\sqrt{2} \times \sqrt{2})\text{R}45^\circ$ phase [3]. This is the most recent experimental result determined from photoelectron diffraction, and we base our calculation on these structural results in preference to other studies [15], though they mostly have very similar structural parameters. Figure 4.1b shows a perspective view of one half unit cell of this structure. Atoms Cu1 and Cu2 do not lie in exactly the same plane, and the O plane lies approximately 0.2 a.u. below this outermost Cu layer. Furthermore, the atoms next to the missing Cu row (O and Cu2 in Fig. 4.1) are allowed to move perpendicular to this row in the surface plane. It will be seen in Sec. 4.5 that this is beneficial for the bonding effects taking place at the surface. Table 4.1 gives the structural parameters of this locally reconstructed $(2\sqrt{2} \times \sqrt{2})\text{R}45^\circ$ phase using the atomic labels shown in Fig. 4.1.

There has been much discussion in recent years on this O/Cu(001) reconstruction. Earlier theoretical calculations [10, 11] were focused mainly on demonstrating the instability of the $c(2 \times 2)$ phase. More recently, theoretical research has been extended to calculations of the reconstructed phase [12, 13, 14], drawing conclusions from the comparison of the electronic structure of the two O/Cu(001) systems. These recent theoretical calculations have proposed bonding mechanisms for both phases deduced from the local density of states and symmetry considerations. In this chapter, we advance these discussions by studying in detail the energy-resolved charge density, that is, the local density of states, showing explicitly the bonding mechanism active at the surface. It is the aim of these calculations to describe in some way the reason for the reconstruction in terms of the electronic structure and the binding effects of the O/Cu(001) system.

In this chapter we first deal with calculations of the unreconstructed $\text{Cu}(001)-c(2 \times 2)\text{-O}$ surface, discussing the effective charge [10], density of states and the energy-resolved charge density. The effective charge is discussed more fully in Sec. 4.3 and Appendix A. The density of states argument is discussed in Sec. 4.4. This is followed by a similar study for the reconstructed phase of $\text{Cu}(001)-(2\sqrt{2} \times \sqrt{2})\text{R}45^\circ\text{-O}$ in Sec. 4.5. It will be seen that the early effective charge argument [10] for the instability of $\text{Cu}(001)-c(2 \times 2)\text{-O}$ seems to be untenable, and that both phases of the O/Cu(001) system must be studied in order to elucidate the reconstruction. This is discussed using a detailed analysis of the energy-resolved charge density.

4.2 Computational Aspects

In this chapter we find it convenient to work with the density of states (DOS), and a “local-energy valence charge density”. The density of states in atom i , $n_i(E)$, is given by integrating (2.67) over the i^{th} muffin-tin. This gives a density of states for each non-equivalent atom. This can also be projected onto a spherical harmonic to give the l - and m - angular momentum-resolved probability density for each atom. Using this DOS, the angular momentum-resolved energy dependence of the electronic structure is available for each atom. We next define the local-energy valence charge density on atom i , $\rho_{i,E}$, as the spatial distribution of the states within an energy window, in other words, equation (2.67) integrated over a convenient range of energies found from the DOS

$$\rho_{i,E} = 2 \int_{E_1}^{E_2} dE n_i(E). \quad (4.1)$$

The range of energies is typically around some peak in the DOS – this gives the actual charge density associated with the peak. With this spatial and energy distribution, bonding can then be discussed systematically.

To find the full charge density, the local density of states $n(\mathbf{r}, E)$ is integrated from an energy starting below the O 2s level, which is taken as a valence state, up to the Fermi energy (E_F). 32 energy points are sufficient for the self-consistent charge density calculation, 10 non-equivalent \mathbf{k} -points are used in the irreducible part of the two-dimensional surface Brillouin zone (SBZ) for the $c(2 \times 2)$ phase, and 16 non-equivalent \mathbf{k} -points for the $(2\sqrt{2} \times \sqrt{2})R45^\circ$ phase. The DOS is evaluated at several of these \mathbf{k} -points, using an energy integration with a small imaginary part of 0.001 a.u. to broaden the peaks.

4.3 Work Function and the Effective Charge

The self-consistent DFT calculations conveniently give good charge densities and work function values. In this section we calculate the work function, Φ , of various phases of O/Cu(001), and investigate its variation from structure to structure. The dependence on $d_{\text{Cu-O}}$ is also calculated. From this variation an effective charge, q^* , may be defined for the surface atoms.

The work function and its dependence on the Cu–O interlayer spacing is shown in Fig. 4.2 for one and two Cu layer calculations of Cu(001)– $c(2 \times 2)$ –O and a bulk-terminated two Cu layer calculation for Cu(001)– $(2\sqrt{2} \times \sqrt{2})R45^\circ$ –O. Within the embedding technique, the precision of the calculation is little affected by the number of layers used in the self-consistent calculation. A quick check of this is shown by the small difference in the work-function results of Cu(001)– $c(2 \times 2)$ –O (Fig. 4.2) for which excellent agreement is seen in Φ for the same $d_{\text{Cu-O}}$ spacing. It is also seen that the work function for both O/Cu(001) phases is greater than that found for clean Cu(001) ($\Phi_{\text{Cu}} = 5.0 \text{ eV}$ is found in a

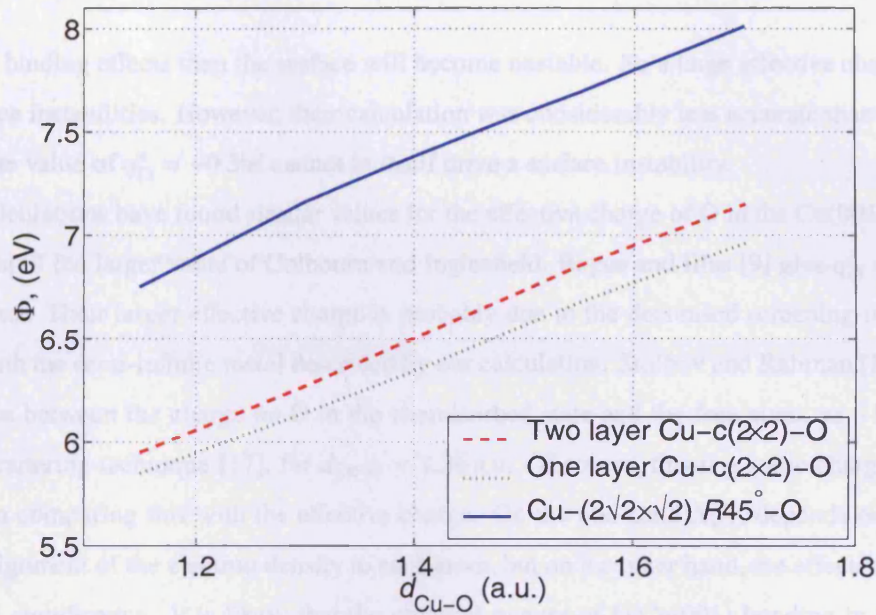


Figure 4.2: Work function of Cu(001)-c(2×2)-O and Cu-(2√2×√2)R45°-O as a function of Cu-O interlayer spacing. The dotted line is a one Cu, one O layer calculation, and the dashed line is a two Cu, one O layer calculation for the Cu(001)-c(2×2)-O unreconstructed surface. The solid line is a two layer Cu, one O layer calculation for the reconstructed Cu(001)-(2√2×√2)R45°-O surface with Cu in bulk-terminated positions.

similar embedding calculation, compared with the experimental value of $\Phi_{\text{Cu}} = 4.59 \text{ eV}$ [16]). The work function is larger than that of the clean Cu(001) surface due to electron transfer from the surface to O. The work function for the Woodruff structure is 5.5 eV, in line with the trend for the work function to decrease with decreasing $d_{\text{Cu-O}}$.

The excess negative charge found on the O atom is related to the effective charge q_i^* . However, the effective charge is not a direct measure of the amount of charge on an atom, but describes the dipole variation with the atomic displacement, and can be calculated using [10]

$$-\frac{\partial \Phi}{\partial z_i} = \frac{4\pi}{A} q_i^* \quad (4.2)$$

In this equation $\partial \Phi / \partial z_i$ is the variation of the work function with the perpendicular displacement of an atom i , occupying surface area A . From Fig. 4.2 the present calculations show that the effective charge on the O atom is $-0.3|e|$ for both surface structures. For details of the proof, see Appendix A. This value is in disagreement with Colbourn and Inglesfield [10], who obtain an effective charge of $-0.9|e|$ for the c(2×2) phase at an O-Cu layer spacing of 1.3 a.u. They argue that an effective charge of this magnitude would lead to phonon softening, hence a tendency to reconstruct. A large effective charge on an atom of type i at a surface can be used to describe possible instabilities by phonon softening. The effective charge on the atoms induces local fields when these atoms are displaced by a small amount from the surface. If the resultant force on the atoms of type i overcomes the local restoring force from

the ordinary binding effects then the surface will become unstable. So a large effective charge is able to induce surface instabilities. However, their calculation was considerably less accurate than ours, and the more accurate value of $q_O^* = -0.3|e|$ cannot in itself drive a surface instability.

Other calculations have found similar values for the effective charge of O in the Cu(001)-c(2 × 2)-O system to that of the larger value of Colbourn and Inglesfield. Bagus and Illas [9] give $q_O^* = -1.17|e|$ for a Cu₅O cluster. Their larger effective charge is probably due to the decreased screening in their cluster compared with the semi-infinite metal described by our calculation. Stolbov and Rahman [12] give ΔQ_O , the difference between the charge on O in the chemisorbed state and the free atom, as $-1.043|e|$ using a multiple scattering technique [17], for $d_{Cu-O} = 1.36$ a.u. Of course, this is a static charge, and care is needed when comparing this with the effective charge. On the one hand ΔQ_O depends on a somewhat arbitrary assignment of the electron density to each atom, but on the other hand, the effective charge only has dynamic significance. It is likely that the physical picture of O/Cu(001) bonding in the system is most accurately described by an actual (not effective) charge on the O of about $-1|e|$, and from this the conclusion can be made that care is needed in using the notion of effective charge as a measure of charge transfer.

As the value of the effective charge on the O is too small to drive a phonon instability, separate explanations are sought for the instability of c(2 × 2) with respect to $(2\sqrt{2} \times \sqrt{2})R45^\circ$ as the O coverage increases. The study is continued in the following sections by considering the chemical binding in both structures. The angular momentum-resolved DOS are used, focusing on O and the nearest-neighbour Cu atoms in the two outermost surface layers. Overlapping peaks in the DOS on different atoms may correspond to a bonding state between these atoms, and to investigate this further we calculate the local-energy valence charge density over a small energy window around such states. Represented as a contour map, this will show explicitly the probability density of the electrons over the small energy window. In most cases this resolves the angular distribution of the bonding orbitals, and also shows the degree of overlap of the electrons for each interacting orbital.

4.4 Electronic Structure of Cu(001)-c(2 × 2)-O

Shown in Fig. 4.3 are the projected density of states for the c(2 × 2) phase of chemisorbed O on Cu(001) at $\bar{\Gamma}$, using an imaginary energy of 0.001 a.u. to broaden the peaks. The plotted DOS are for the O atom p-orbitals (Op), the p-orbitals (Cu1p) and the d-orbitals (Cu1d) for the surface Cu atom, and the d-orbitals of the second layer Cu directly below the O atom (Cu2d). Note that for the case of this c(2 × 2) surface structure the atoms are labelled differently from that of the reconstructed phase. For this structure, using the bulk-terminated Cu atoms and O in its ideal fourfold-hollow site, all the first layer Cu atoms are

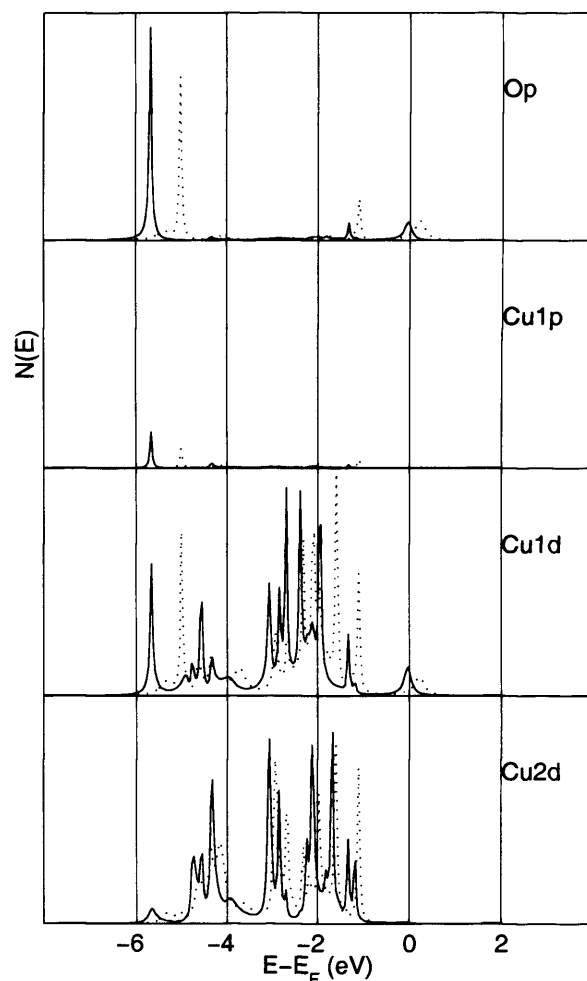


Figure 4.3: Projected density of states for atoms in the c(2 × 2) phase of the O/Cu(001) surface. The DOS are shown for $d_{\text{Cu-O}} = 1.15$ a.u. (solid line) and $d_{\text{Cu-O}} = 1.5$ a.u. (dotted line) for the $\bar{\Gamma}$ -point for Op, Cu1p, Cu1d, and Cu2d. For a description of the atom labelling see text.

equivalent and are labelled Cu1. There are two non-equivalent Cu atoms in the second layer. The Cu atom directly beneath the O atoms are labelled Cu2, and the other non-equivalent Cu atom in this layer is not discussed in this chapter, and the electronic structure is not shown. It is found that the adsorbed O has little effect on this Cu atom and its DOS resembles a second layer Cu DOS of a clean surface. The DOS is shown for two separate Cu–O interlayer spacings, 1.5 a.u. and 1.15 a.u. Figures 4.4 and 4.5 show the local-energy valence charge densities of each structure, obtained from energy ranges for which prominent states are found within the Op DOS of the respective structure. These are all evaluated at $\bar{\Gamma}$. The charge densities are vertical cross-sections cutting nearest-neighbour Cu–O–Cu atom centres with O centred on zero in the surface parallel direction. To gain perspective of the atomic positions in these contour plots, a full self-consistent charge density contour map of Cu(001)-c(2 × 2)-O for $d_{\text{Cu-O}} = 1.15$ a.u. is given in Fig. 4.5a. By comparing the densities of states shown in Fig. 4.3 with the local-energy charge densities

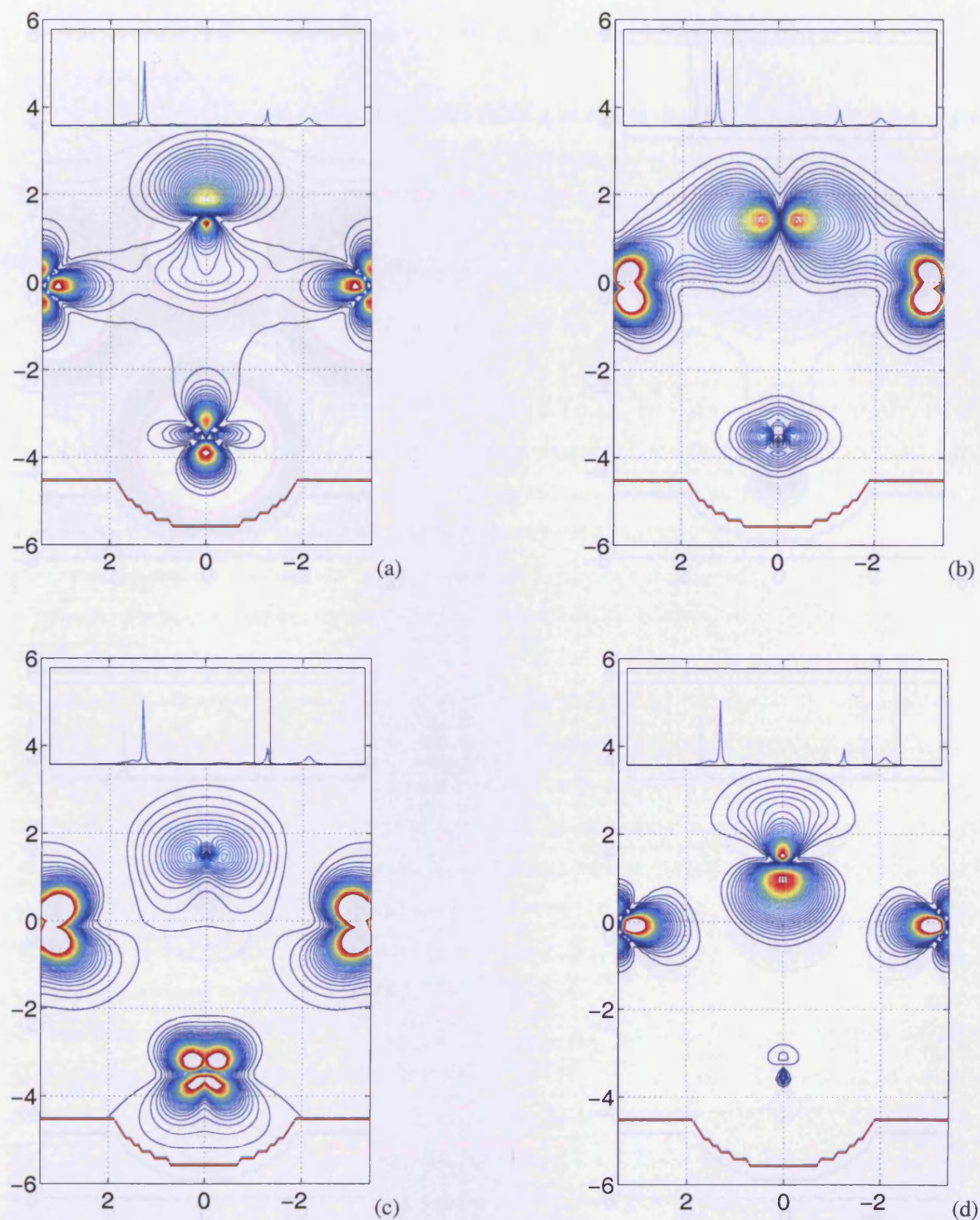


Figure 4.4: Contour map of valence charge densities of Cu(001)-c(2 × 2)-O within energy ranges (a) $-6 < E(\text{eV}) < -5.2$, (b) $-5.5 < E(\text{eV}) < -4.5$, (c) $-1.5 < E(\text{eV}) < -1.0$, and (d) $-0.2 < E(\text{eV}) < +0.7$, on a vertical cut-plane. Energies are relative to the Fermi energy E_F . The surface parallel direction cuts three nearest-neighbour atoms Cu-O-Cu. Cu-O interlayer spacing is 1.5 a.u. A boundary can be seen below $z = -4.5$ a.u. This is the embedding surface and the charge density below this line (excluding the muffin tin cap) is meaningless. Contour spacings are 2.5×10^{-4} a.u. with a maximum cut-off at 0.01 a.u. Inset – DOS of O atom as shown in Fig. 4.3 giving energy range from which local-energy charge density was obtained.

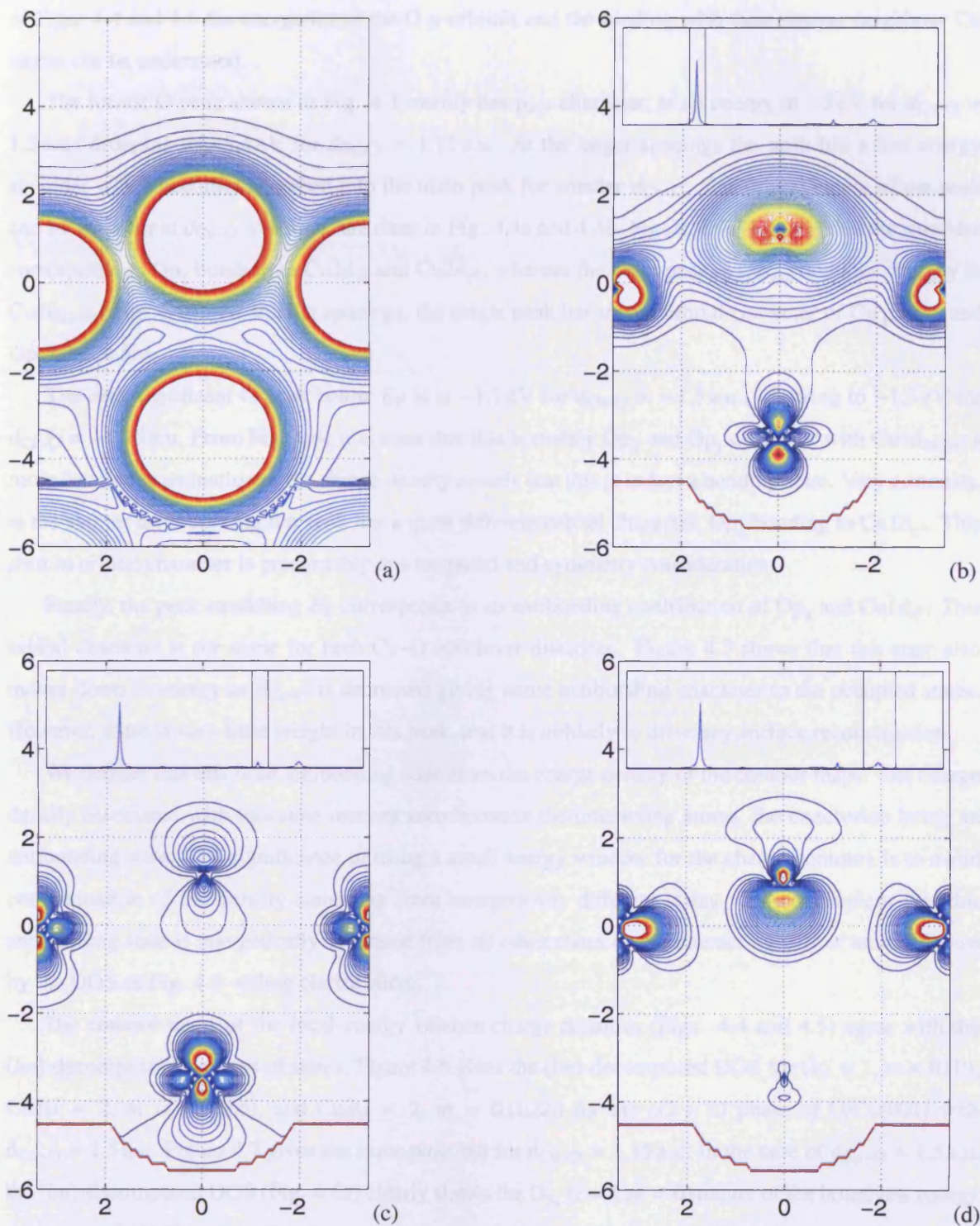


Figure 4.5: Contour map of Cu(001)-c(2 × 2)-O of (a) the total charge density, and the valence charge density within energy range (b) $-5.9 < E(\text{eV}) < -5.4$, (c) $-1.5 < E(\text{eV}) < -1$, and (d) $-0.5 < E(\text{eV}) < +0.5$ on a vertical cut-plane. Energy is relative to the Fermi energy, E_F . The surface parallel direction cuts three nearest-neighbour atoms Cu-O-Cu. Cu-O interlayer spacing is 1.15 a.u. Contour spacings are 2.5×10^{-4} a.u. with a maximum cut-off at 0.01 a.u. except for (a), for which contour spacings are 2.5×10^{-4} a.u. with a maximum cut-off at 0.2 a.u. See Fig. 4.4 for a description of the embedding surface and inset diagrams.

of Figs. 4.4 and 4.5 the energetics of the O p-orbitals and the binding with their nearest neighbour Cu atoms can be understood.

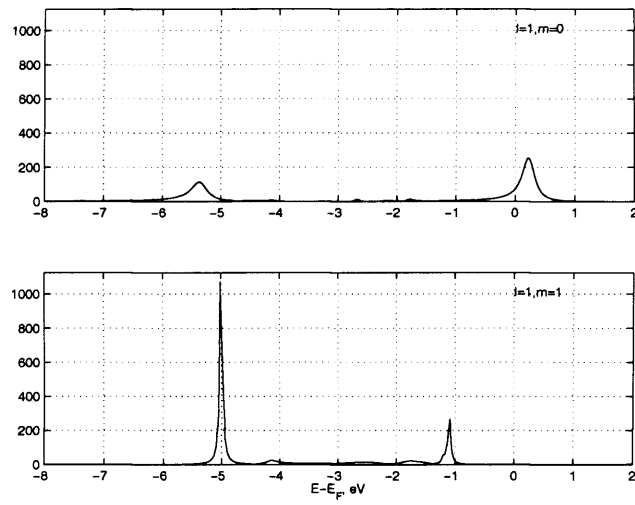
The lowest O peak shown in Fig. 4.3 mainly has $p_{x/y}$ character, at an energy of -5 eV for $d_{\text{Cu-O}} = 1.5$ a.u. dropping to -5.4 eV for $d_{\text{Cu-O}} = 1.15$ a.u. At the larger spacings the peak has a low energy shoulder which becomes absorbed into the main peak for smaller $d_{\text{Cu-O}}$. The orbital nature of the peak and its shoulder at $d_{\text{Cu-O}} = 1.5$ a.u. are clear in Fig. 4.4a and 4.4b. Figure 4.4a suggests that the shoulder corresponds to Op_z bonding to Cu1d_{z^2} and Cu2d_{z^2} , whereas the main peak is $\text{Op}_{x/y}$ bonding strongly to $\text{Cu1d}_{zx/yz}$ (Fig. 4.4b). At smaller spacings, the single peak has mixed orbital character of Op_x , Op_y , and Op_z (Fig. 4.5b).

The next significant O peak below E_F is at -1.1 eV for $d_{\text{Cu-O}} = 1.5$ a.u., lowering to -1.3 eV for $d_{\text{Cu-O}} = 1.15$ a.u. From Fig. 4.4c it is clear that this is mainly Op_x and Op_y character with $\text{Cu1d}_{zx/yz}$; a more detailed examination of the charge density reveals that this is in fact a bonding state. Very curiously, at the shorter layer spacing the peak has a quite different orbital character, Op_z bonding to Cu1d_{z^2} . This shift in orbital character is presumably due to spatial and symmetry considerations.

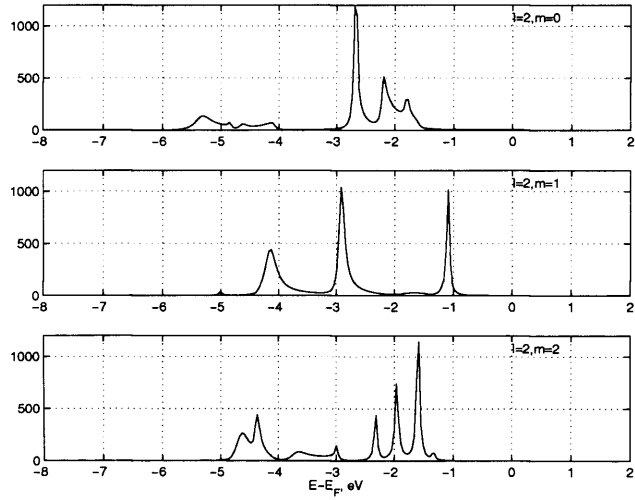
Finally, the peak straddling E_F corresponds to an antibonding contribution of Op_z and Cu1d_{z^2} . This orbital character is the same for both Cu–O interlayer distances. Figure 4.3 shows that this state also moves down in energy as $d_{\text{Cu-O}}$ is decreased giving some antibonding character to the occupied states. However, there is very little weight in this peak, and it is unlikely to drive any surface reconstruction.

We deduce that this is an antibonding state from the charge density of the contour maps. The charge density associated with this state reaches zero between the interacting atoms, the conclusion being an antibonding state. The significance of using a small energy window for the charge contours is to avoid contamination of the density stemming from energetically different states. It is convenient that this antibonding state is energetically separated from all other states of the interacting pair of atoms, shown by the DOS of Fig. 4.3, aiding clarification.

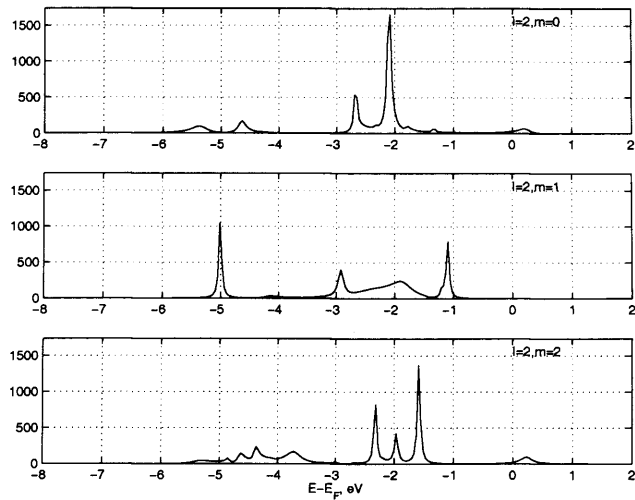
The contour maps of the local-energy valence charge densities (Figs. 4.4 and 4.5) agree with the (lm) -decomposed densities of states. Figure 4.6 gives the (lm) -decomposed DOS for $\text{O}(l = 1, m = 0, |1|)$, $\text{Cu1}(l = 2, m = 0, |1|, |2|)$, and $\text{Cu2}(l = 2, m = 0, |1|, |2|)$ for the $c(2 \times 2)$ phase of O/Cu(001) with $d_{\text{Cu-O}} = 1.5$ a.u. Figure 4.7 gives the same plots but for $d_{\text{Cu-O}} = 1.15$ a.u. In the case of $d_{\text{Cu-O}} = 1.5$ a.u. the (lm) -decomposed DOS (Fig. 4.6a) clearly shows the Op_z ($l = 1, m = 0$) nature of the broad low energy peak at -5.2 eV. The $\text{Op}_{x/y}$ ($l = 1, m = |1|$) nature of the large peak at -5 eV is also seen. The contour maps of Figs. 4.4 and 4.5 show that these two peaks combine with one another with a reduction in energy with a movement of O into the surface from $d_{\text{Cu-O}} = 1.5$ a.u. to $d_{\text{Cu-O}} = 1.15$ a.u. The coalescence of these peaks is seen for $(l = 1, m = 0)$ and $(l = 1, m = |1|)$ for $d_{\text{Cu-O}} = 1.15$ a.u. (Fig. 4.7), and also shows



(a)

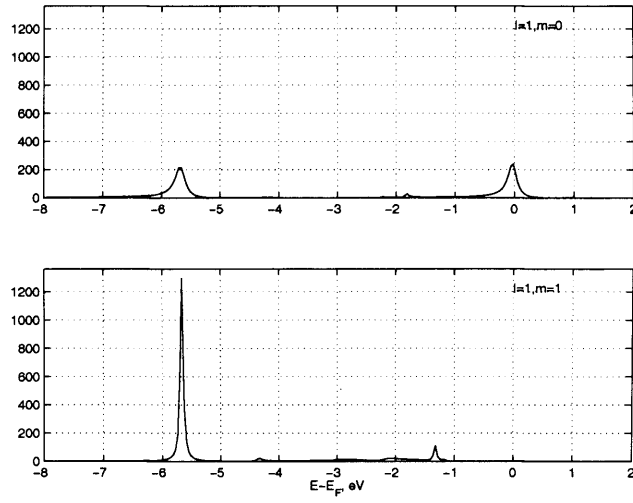


(b)

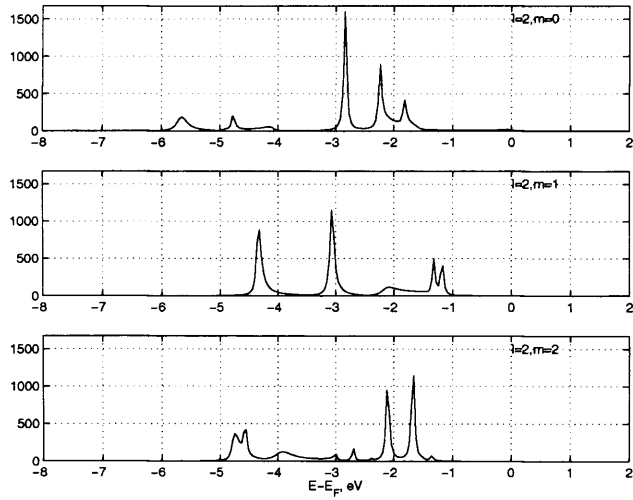


(c)

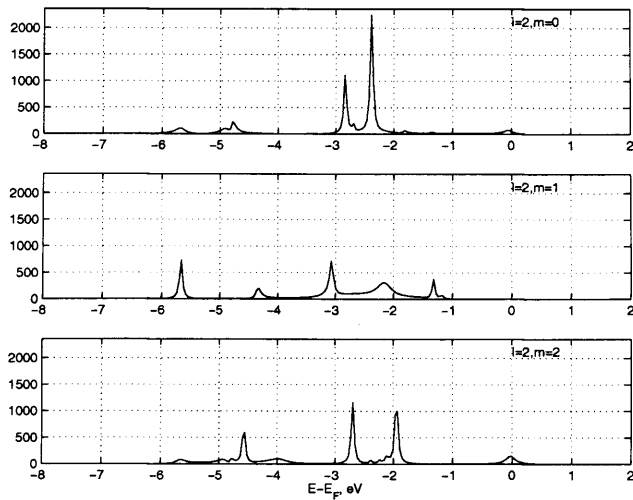
Figure 4.6: (lm)-decomposed density of states for the $c(2 \times 2)$ phase of the O/Cu(001) surface, showing DOS for (a) O($l = 1, m = 0, |1|$), (b) Cu1($l = 2, m = 0, |1|, |2|$), and (c) Cu2($l = 2, m = 0, |1|, |2|$). Cu–O interlayer spacing is 1.5 a.u.



(a)



(b)



(c)

Figure 4.7: (lm)-decomposed density of states for the $c(2 \times 2)$ phase of the O/Cu(001) surface, showing DOS for (a) O($l = 1, m = 0, |1\rangle$), (b) Cu1($l = 2, m = 0, |1\rangle, |2\rangle$), and (c) Cu2($l = 2, m = 0, |1\rangle, |2\rangle$). Cu–O interlayer spacing is 1.15 a.u.

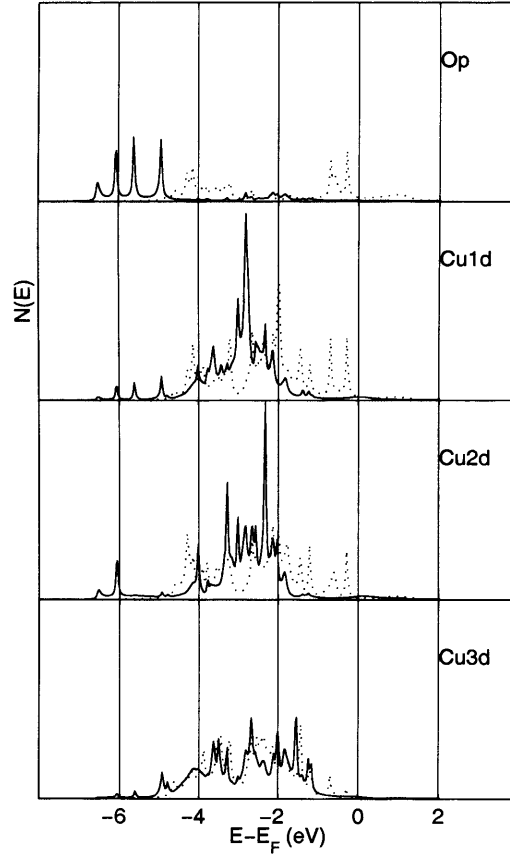


Figure 4.8: Projected density of states for atoms in the $(2\sqrt{2} \times \sqrt{2})\text{R}45^\circ$ phase of the $\text{O}/\text{Cu}(001)$ surface. The DOS are shown for locally reconstructed phase of Woodruff *et al.* [3] (solid line) and $d_{\text{Cu-O}} = 1.5$ a.u. (dotted line) for ideal bulk-terminated geometries of Cu using $\bar{\Gamma}$ -point only. DOS shown for Op, Cu1d, Cu2d, and Cu3d. For a description of the atom labelling see text.

their bonding nature to the appropriate Cu atoms adjacent to O, as described previously.

The surprising distance dependence of the orbital nature of the peak at -1.2 eV for the Op state is not clear from the (lm) -decomposed DOS. Although the peak at this energy for $l = 1$, $m = |1|$ does not transform to a peak at a similar energy for $l = 1$, $m = 0$ for O, from $d_{\text{Cu-O}} = 1.5$ a.u. to $d_{\text{Cu-O}} = 1.15$ a.u., the original peak for $d_{\text{Cu-O}} = 1.5$ a.u. does decrease considerably in density on the transition (Figs. 4.6 and 4.7).

The (lm) -decomposed DOS does show the p_z nature of the peak at the Fermi energy for both values of $d_{\text{Cu-O}}$, as suggested in the contour maps in Figs. 4.4 and 4.5. The antibonding nature of the interacting orbitals at these energies cannot be shown however by the density of states, and we must therefore rely on the charge densities to make such assumptions.

4.5 Electronic Structure of Cu(001)– $(2\sqrt{2} \times \sqrt{2})$ R45°–O

Having examined some aspects of the chemical bonding at the Cu(001)–c(2 × 2)–O system, the reconstructed Cu(001)– $(2\sqrt{2} \times \sqrt{2})$ R45°–O phase is now considered, to see how the bonding alters on reconstruction. Again, the local-energy charge densities, integrated over suitable energy regions, are used to study the binding between the chemisorbed O and its nearest-neighbour Cu atoms at the surface.

Figure 4.8 shows the density of states at $\bar{\Gamma}$ for the Op state, the d-orbitals of the two non-equivalent surface Cu atoms, (Cu1d) and (Cu2d), and the second layer Cu (Cu3d) directly below the O. The atoms are labelled as in Fig. 4.1. The DOS for two $(2\sqrt{2} \times \sqrt{2})$ R45° structures are given, that of $d_{\text{Cu-O}} = 1.5$ a.u. with Cu atoms in bulk-terminated positions, and the structure given by ref. [3], which we may assume to be the more realistic structure of 0.5 monolayer of O on Cu(001). The reconstruction with the large Cu–O spacing is given for comparison with the c(2 × 2) phase, as in this model of $(2\sqrt{2} \times \sqrt{2})$ R45°, rows of the Cu atoms are removed and the remaining atoms more or less keep their unreconstructed positions. The corresponding local-energy valence charge densities are shown in Fig. 4.9. Due to the anisotropy of the surface a convention must be used to describe the surface parallel directions. For the purpose of this thesis the *x*-direction is taken as the line cutting an O centre and the nearest missing Cu site (in Fig. 4.1 this would mean cutting atoms O and Cu1 and extending to the missing Cu site). The *y*-direction can then be taken as the line parallel to the missing Cu row (or the line Cu2–O–Cu2 in Fig. 4.1).

A general feature of the results is the large spatial distortions of the O orbitals due to the symmetry breaking in the reconstructed surface. On surface reconstruction to the $(2\sqrt{2} \times \sqrt{2})$ R45° phase there is a large change in the environment of the O atoms. For a similar $d_{\text{Cu-O}}$ spacing to the unreconstructed phase it is expected that large distortions in the O orbitals will result, as a break in symmetry is now present along a surface parallel direction in addition to the surface normal. The effect of the large symmetry-breaking on the orbitals is shown in Fig. 4.9, showing the local-energy charge density at the $(2\sqrt{2} \times \sqrt{2})$ R45° bulk-terminated surface with a Cu–O interlayer spacing of 1.5 a.u. For certain energies the charge shows large spatial distortions in the Op electron density, from the usual orthonormal lobes – this is particularly apparent in Figs. 4.9b and 4.9f. One way to reduce this distortion would be to bring the O atom down to the plane of the surface Cu atoms. This is precisely what the structure of Woodruff *et al.* (Fig. 4.1) achieves. Figure 4.10 shows the local-energy electron density contour maps for this structure, for prominent peaks found in the DOS of Op in Fig. 4.8.

On inspection of the densities of states in Fig. 4.8 together with the corresponding local-energy charge densities of Figs. 4.9 and 4.10, an increased binding effect at the surface is clearly shown on moving to the fully reconstructed surface shown in Fig. 4.1b. Strong interaction effects are seen in the

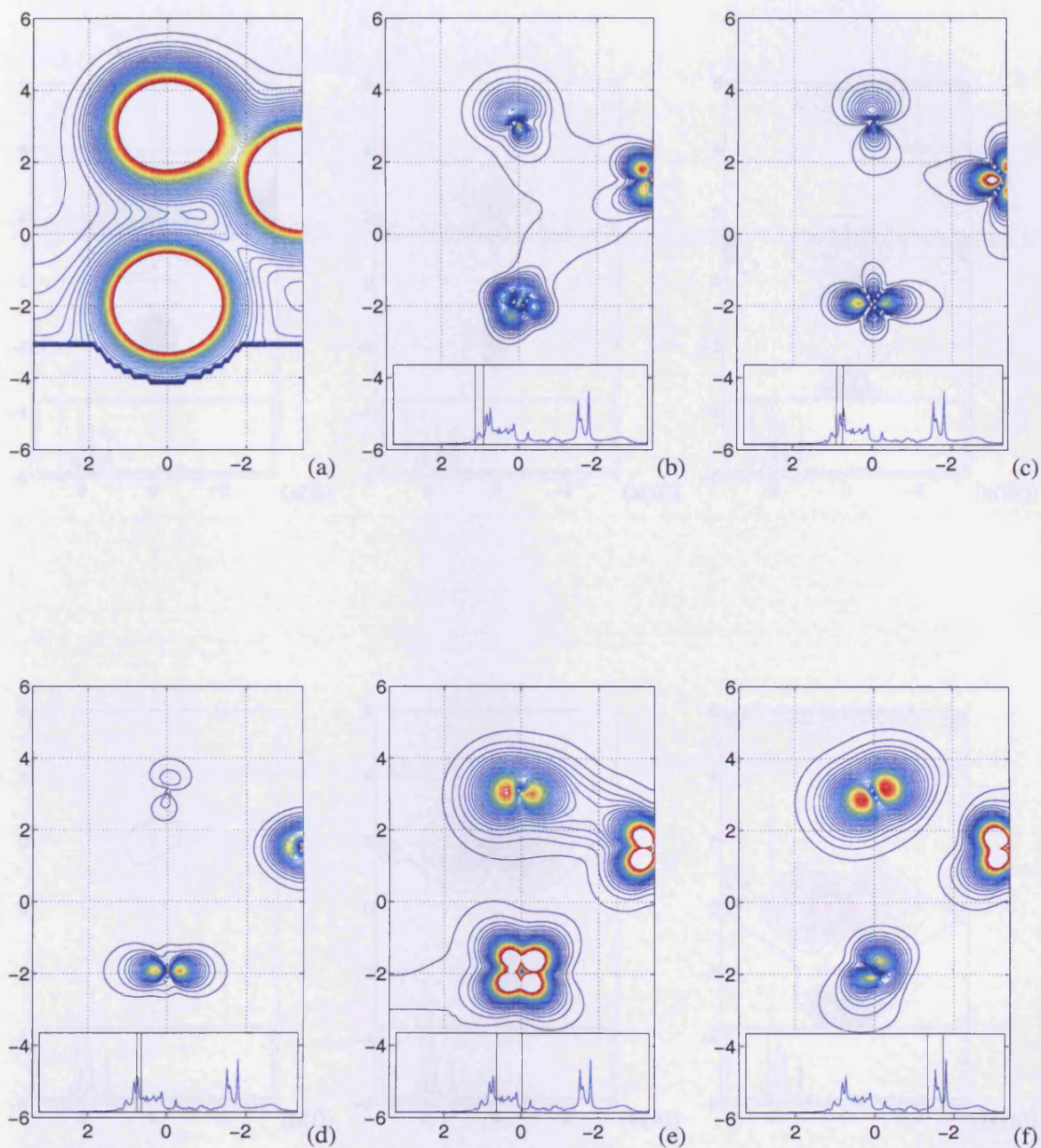


Figure 4.9: Contour maps of $\text{Cu}(001)-(2\sqrt{2} \times \sqrt{2})\text{R}45^\circ\text{-O}$ showing (a) the total charge density, and the valence charge density within energy range (b) $-4.75 < E(\text{eV}) < -4.42$, (c) $-4.42 < E(\text{eV}) < 4.18$, (d) $-4.18 < E(\text{eV}) < -4.0$, (e) $-4.0 < E(\text{eV}) < -3.0$, and (f) $-1.0 < E(\text{eV}) < -0.39$, on a vertical cut-plane normal to the line of the missing Cu row. The contour plots show O centred on zero in the surface parallel direction, a surface layer Cu atom and the second layer Cu atom directly beneath O. Cu–O interlayer spacing is 1.5 a.u. Contour spacings are 2.5×10^{-4} a.u. with a maximum cut-off at 0.01 a.u. except for (a), for which contour spacings are 2.5×10^{-4} a.u. with a maximum cut-off at 0.2 a.u. See Fig. 4.4 for a description of the embedding surface. Inset – DOS of O atom as shown in Fig. 4.8 giving energy range from which local-energy valence charge density was obtained.

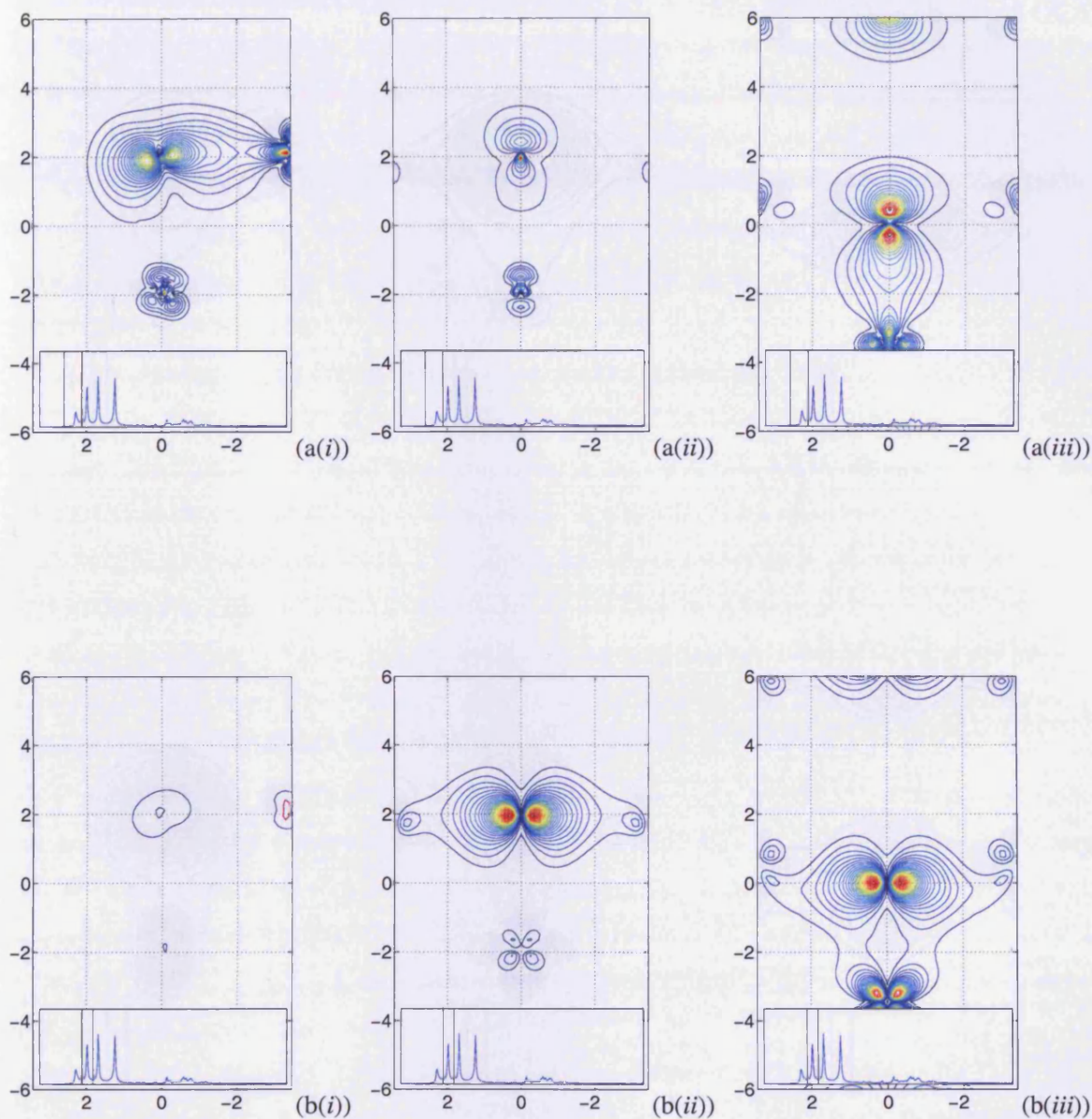


Figure 4.10: Part I. Contour map of $\text{Cu}(001)-(2\sqrt{2} \times \sqrt{2})\text{R}45^\circ\text{-O}$ of the valence charge density within energy range (a) $-7.0 < E(\text{eV}) < -6.27$, and (b) $-6.27 < E(\text{eV}) < -5.83$ using the surface geometry of Woodruff *et al.* [3]. The contour plots show O centred on zero in the surface parallel direction for a vertical cut-plane (i) normal and (ii) parallel to the line of the missing Cu rows, and (iii) a surface parallel plane cutting the O centre. See Fig. 4.4 for a description of the embedding surface and contour layers. Inset - DOS of O atom as shown in Fig. 4.8 giving energy range from which local-energy valence charge density was obtained.

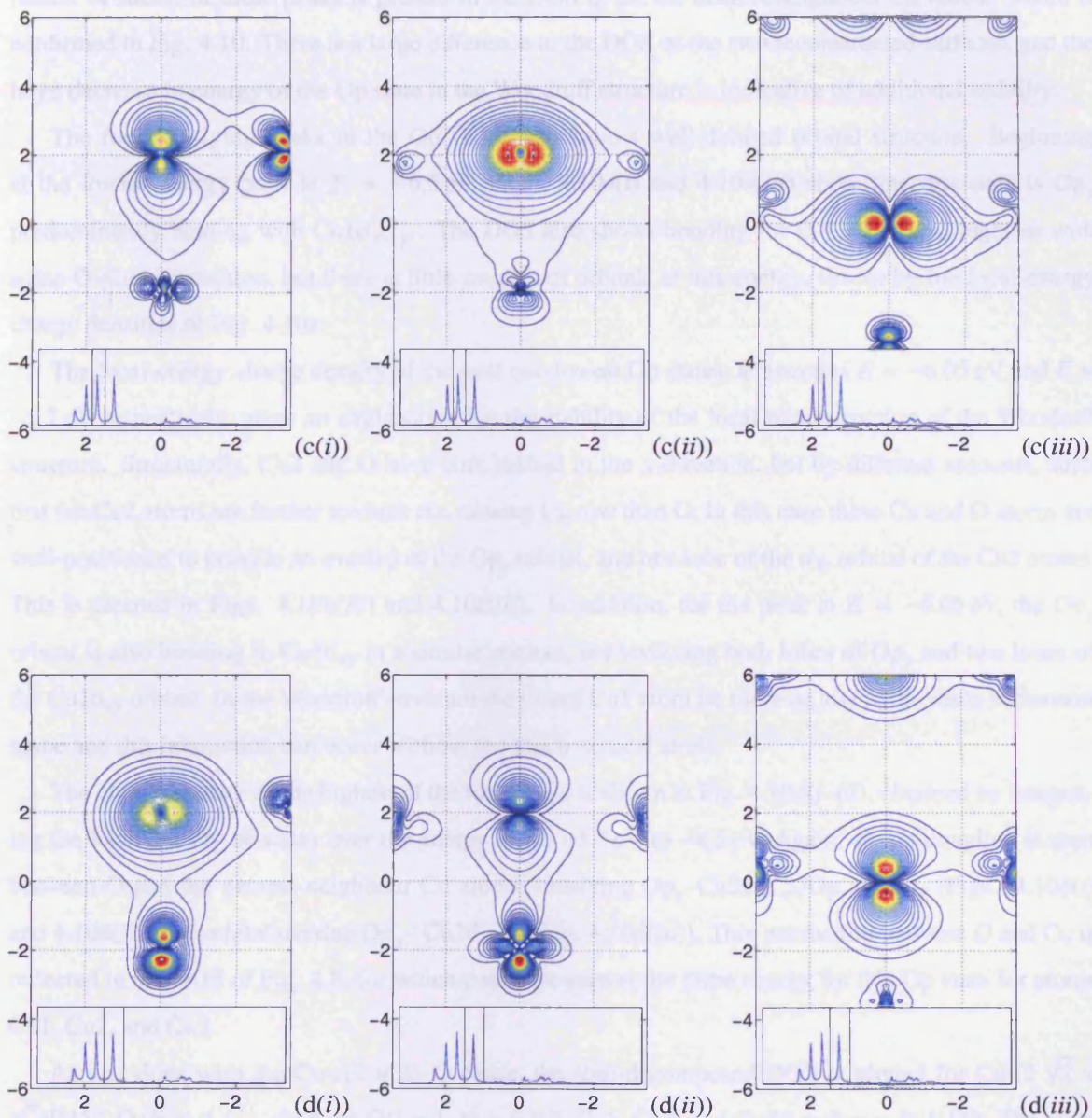


Figure 4.10: Part II. Contour map of $\text{Cu}(001)-(2\sqrt{2} \times \sqrt{2})\text{R}45^\circ\text{-O}$ of the valence charge density within energy range (c) $-5.83 < E(\text{eV}) < 5.3$, and (d) $-5.3 < E(\text{eV}) < -4.5$, using the surface geometry of Woodruff *et al.* [3]. The contour plots show O centred on zero in the surface parallel direction for a vertical cut-plane (i) normal and (ii) parallel to the line of the missing Cu rows, and (iii) a surface parallel plane cutting the O centre. See Fig. 4.4 for a description of the embedding surface and contour layers. Inset - DOS of O atom as shown in Fig. 4.8 giving energy range from which local-energy valence charge density was obtained.

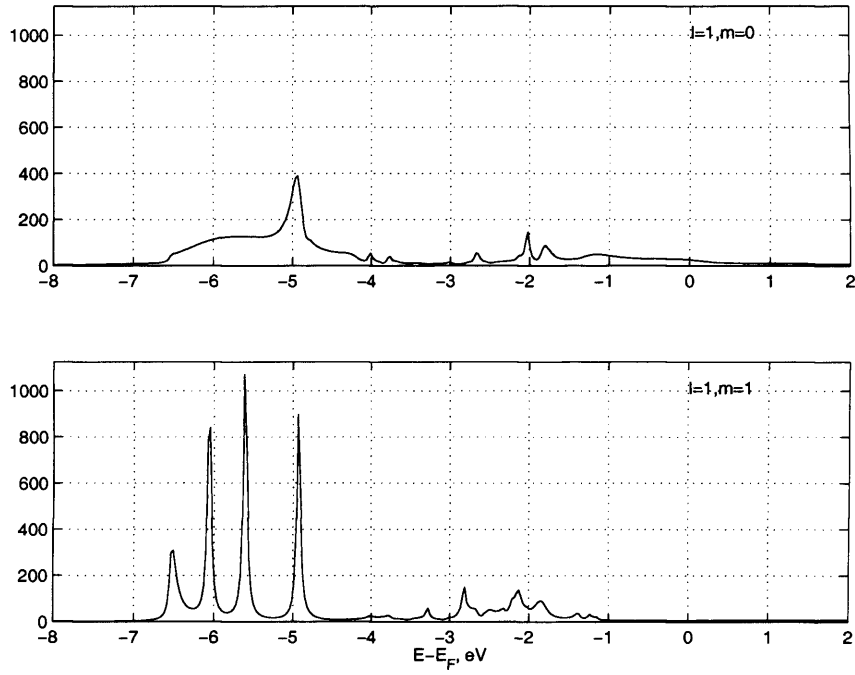
DOS for particular atoms. At the low energy of -7 eV to -4 eV (low in comparison to the energies of the O p-states shown for the other surface structures presented) the Op state shows four distinct, sharp peaks. A subset of these peaks is present in the DOS of all the nearest-neighbour Cu atoms, which is confirmed in Fig. 4.10. There is a large difference in the DOS of the two reconstructed surfaces, and the large decrease in energy of the Op state in the Woodruff structure is indicative of additional stability.

The four low-lying peaks in the Op DOS each have a well-defined orbital structure. Beginning at the lowest energy peak at $E = -6.5$ eV, Figs. 4.10a(i) and 4.10a(iii) show that this state is Op_x predominantly bonding with $\text{Cu1d}_{x^2-y^2}$. The DOS also shows bonding for O–Cu2 atoms, together with some O–Cu3 interaction, but there is little overlap of orbitals at this energy, shown by the local-energy charge densities of Fig. 4.10a.

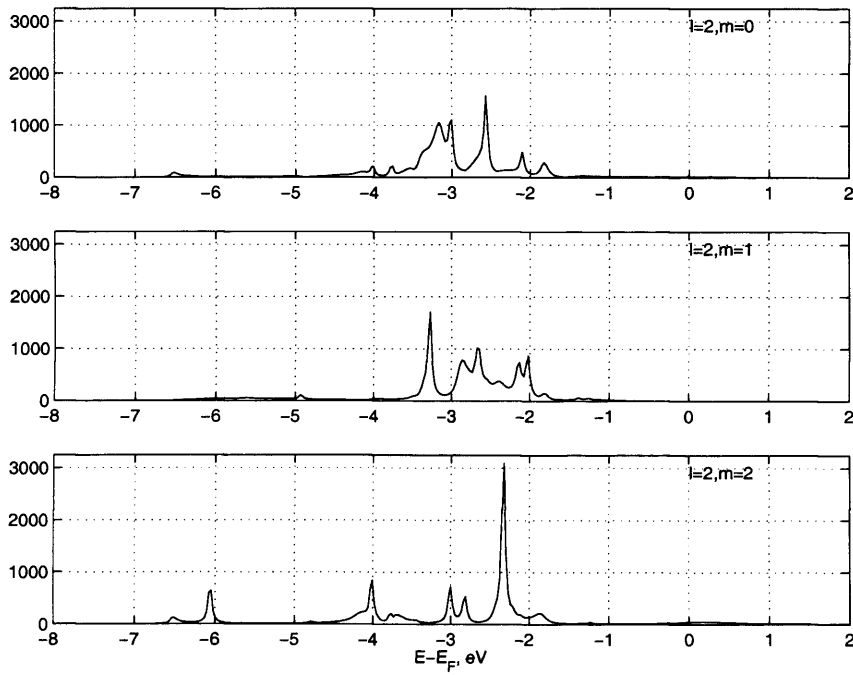
The local-energy charge density of the next two lowest Op states, at energies $E = -6.05$ eV and $E = -5.7$ eV respectively, gives an explanation for the stability of the local reconstruction of the Woodruff structure. Structurally, Cu2 and O have both shifted in the x -direction, but by different amounts, such that the Cu2 atoms are further towards the missing Cu row than O. In this case these Cu and O atoms are well-positioned to provide an overlap of the Op_y orbital, and one lobe of the d_{xy} orbital of the Cu2 atoms. This is clearest in Figs. 4.10b(iii) and 4.10c(iii). In addition, for the peak at $E = -6.05$ eV, the Op_y orbital is also bonding to Cu1d_{xy} in a similar manner, but involving both lobes of Op_y and two lobes of the Cu1d_{xy} orbital. In the Woodruff structure the O and Cu1 atom lie more or less in the same horizontal plane and this interaction can occur without too much vertical strain.

The charge density of the highest of the four peaks is shown in Fig. 4.10d(i–iii), obtained by integrating the local density of states over the energy range -5.3 eV to -4.5 eV. Again, strong coupling is seen between O and the nearest-neighbour Cu atoms, involving Op_z – $\text{Cu3d}_{y^2-z^2}/\text{Op}_z$ – Cu3p_z (Figs. 4.10d(i) and 4.10d(ii)) and orbital overlap Op_x – $\text{Cu2d}_{x^2-y^2}$ (Fig. 4.10d(iii)). This interaction between O and Cu is reflected in the DOS of Fig. 4.8, for which peaks are seen at the same energy for this Op state for atoms Cu1, Cu2, and Cu3.

As was done with the Cu-c(2 × 2)–O phase, the (lm)-decomposed DOS is plotted for Cu-(2√2 × √2)R45°–O (Fig. 4.11), showing O($l = 1, m = 0, |1|$), Cu1, Cu2, and Cu3($l = 2, m = 0, |1|, |2|$). The plots again reinforce the conclusion drawn from the contour maps of the local-energy valence charge densities (Fig. 4.10): all four of the low energy peaks of O show $p_{x/y}$ character, with the highest energy of these four peaks also having a Op_z contribution. The bonding apparent in the (lm)-decomposed DOS also gives a similar picture to the contour maps, shown by the alignment of peaks at similar energies between O and nearest-neighbour Cu atoms. These conclusions also maintain the symmetry requirements between bonding orbitals.

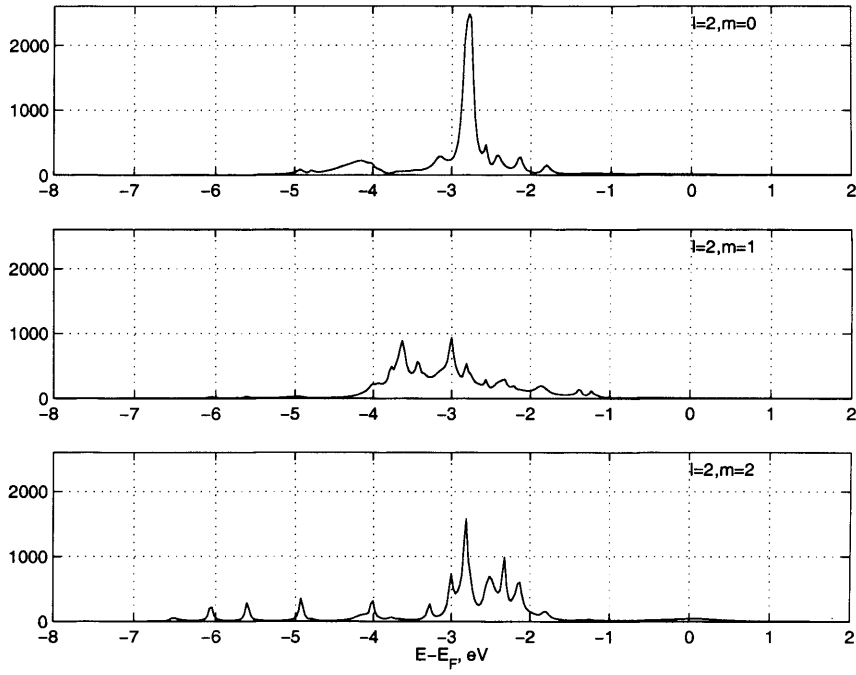


(a)

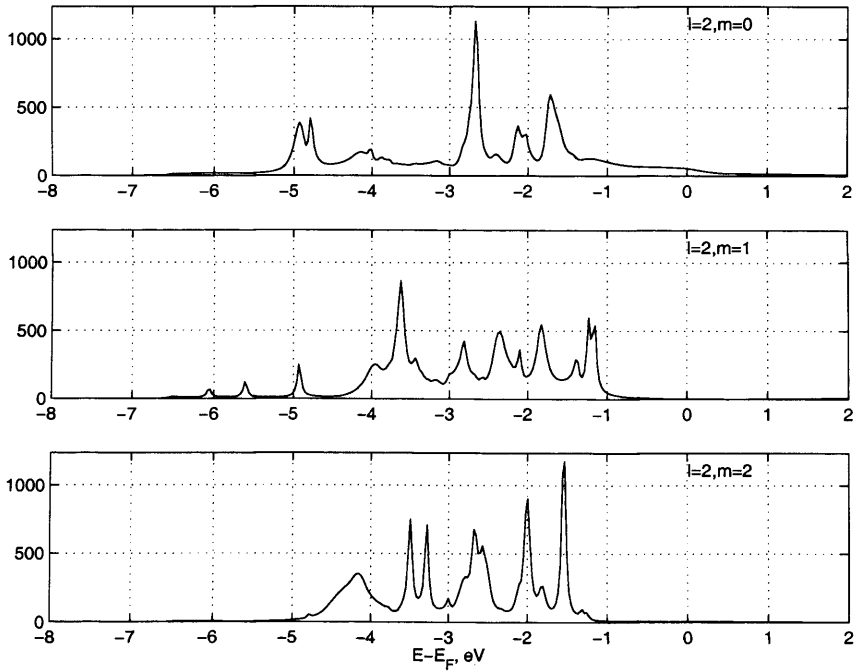


(b)

Figure 4.11: Part I. (lm)-decomposed density of states for the $(2\sqrt{2} \times \sqrt{2})\text{R}45^\circ$ phase of the $\text{O}/\text{Cu}(001)$ surface, showing DOS for (a) $\text{O}(l = 1, m = 0, |1|)$ and (b) $\text{Cu}(l = 2, m = 0, |1|, |2|)$. Surface structure as described by Woodruff *et al.* [3].



(c)



(d)

Figure 4.11: Part II. (lm)-decomposed density of states for the $(2\sqrt{2} \times \sqrt{2})\text{R}45^\circ$ phase of the $\text{O}/\text{Cu}(001)$ surface, showing DOS for (c) $\text{Cu}_2(l = 2, m = 0, |1|, |2|)$, and (d) $\text{Cu}_3(l = 2, m = 0, |1|, |2|)$. Surface structure as described by Woodruff *et al.* [3].

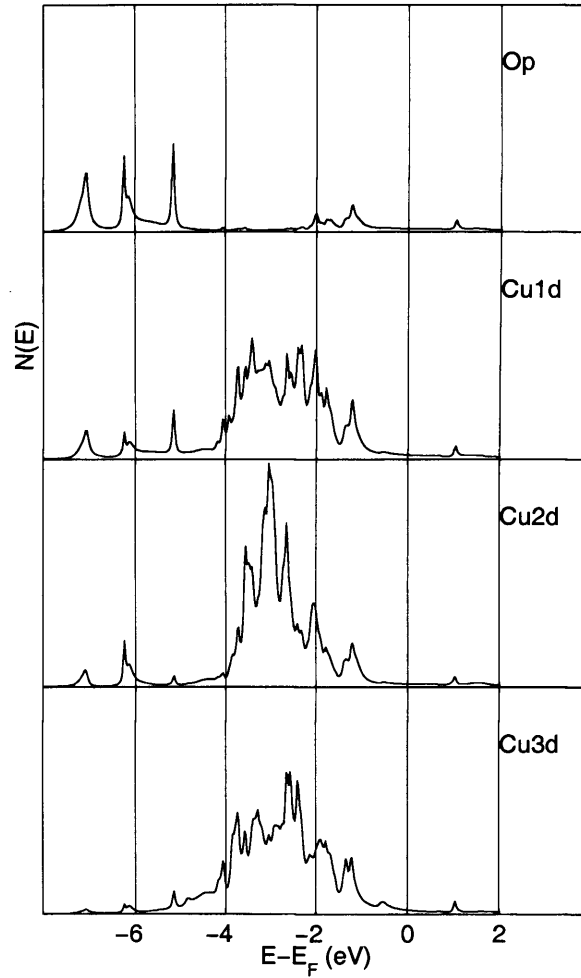


Figure 4.12: Projected density of states for atoms in the $(2\sqrt{2} \times \sqrt{2})R45^\circ$ phase of the O/Cu(001) surface. The DOS are shown for the locally reconstructed phase of Woodruff *et al.* [3]. The DOS is for $\mathbf{k} = \frac{\pi}{a}(\frac{2}{3}, 0)$. The DOS shown are for Op, Cu1d, Cu2d, and Cu3d. For a description of the atom labelling see text.

Although the results shown in Figs. 4.8–4.11 are calculated at $\bar{\Gamma}$, the bonding described for the $(2\sqrt{2} \times \sqrt{2})R45^\circ$ phase is not limited to zero wavevector. Although slight dispersion of the states occur, similar orbital overlap is seen for finite wavevectors, as shown by the DOS in Figs. 4.12–4.14. These figures give the DOS for the same atoms and their respective orbitals as in Fig. 4.8 but for $\mathbf{k} = \frac{\pi}{a}(\frac{2}{3}, 0)$, $\mathbf{k} = \frac{\pi}{a}(\frac{8}{9}, \frac{1}{9})$, and $\mathbf{k} = \frac{\pi}{a}(\frac{2}{3}, \frac{2}{3})$, respectively, in the irreducible part of the SBZ. Again, four peaks are seen for the Op state between -8 eV and -4 eV – in Fig. 4.12 the state at -6 eV contains a shoulder on the right hand (higher energy) side. The DOS of the neighbouring Cu atoms also shows the same subset of peaks of these four Op states as the DOS at $\bar{\Gamma}$.

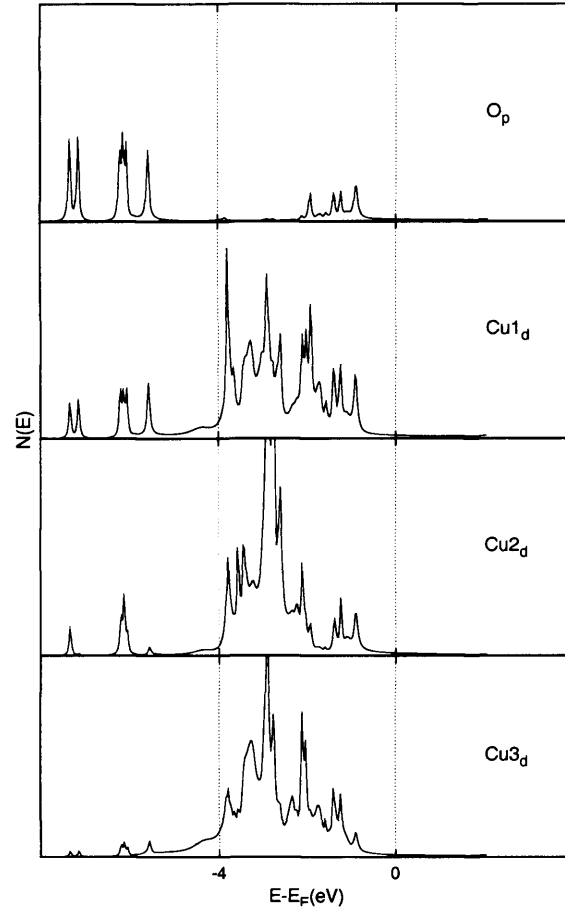


Figure 4.13: As in Fig. 4.12 but for $\mathbf{k} = \frac{\pi}{a} \left(\frac{8}{9}, \frac{1}{9} \right)$.

4.6 Conclusions

It is clear from the previous section that for the reconstructed phase, the Woodruff model is more stable than the ideal $(2\sqrt{2} \times \sqrt{2})R45^\circ$ structure – in particular, O-states have a much lower energy than for the ideal structure. This is quantified by calculating the centre of gravity of the O DOS, given by

$$\bar{E} = \frac{\int_{E_F}^{E_F} dE N_{\Gamma}(E) E}{\int_{E_F}^{E_F} dE N_{\Gamma}(E)}. \quad (4.3)$$

The values of \bar{E} are given in Table 4.2. The lowering of the centre of gravity shows the increased stability in the Woodruff reconstructed surface over the ideal reconstruction. The origin of this reduction in energy is the increased interaction between O and nearest-neighbour Cu atoms on reconstruction. Due to the missing Cu rows, the O atoms in the ideal reconstructed surface sit at asymmetric hollow sites. This has the effect of decreasing the symmetry of the Cu atoms around O, but the movement of O into the surface from its equilibrium $c(2 \times 2)$ position normal to the surface minimises this asymmetry. As a result, strong interactions are allowed between the chemisorbed O and the surface Cu atoms, which results in increased

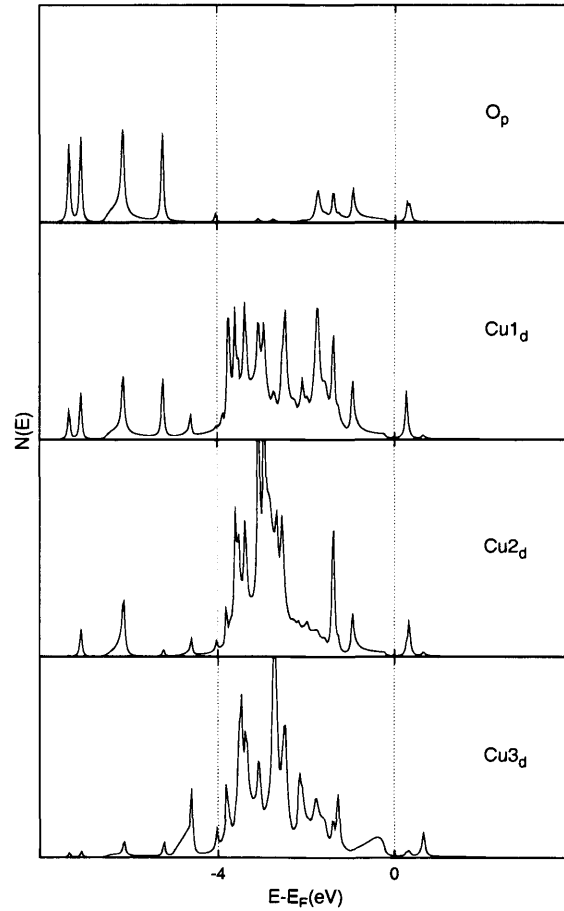


Figure 4.14: As in Fig. 4.12 but for $\mathbf{k} = \frac{\pi}{a} \left(\frac{2}{3}, \frac{2}{3} \right)$.

binding in the Woodruff structure. Because the O is firmly within the surface Cu layer, the bonding of the O_p state is optimised with little spatial distortion from the free atom spatial orientation. Examples of this are shown in Fig. 4.10, where in order of increasing energy, O_{p_x} binds with $Cu1d$ (4.10a(i)), O_{p_y} with $Cu2d$ (4.10b(ii–iii), c(ii–iii), d(iii)), and even O_{p_z} with $Cu2d$ (4.10c(i)), showing little orbital strain on visual inspection. Fig. 4.10 also shows O_{p_z} binding to $Cu3d$, as shown with all other systems under investigation. It seems that the O placement in this reconstructed phase has two influencing effects on the relative stability of the O/Cu(001) surface. Firstly, the electronic spatial overlap is optimised to achieve high symmetry between bonding orbitals, and secondly, the energy of the O_p state is lowered, presumably as a related effect of the higher symmetry.

The degree of hybridisation between O and Cu depends upon spatial considerations and also energetic overlap. Our results, for both $(2\sqrt{2} \times \sqrt{2})R45^\circ$ structures show greatest O–Cu hybridisation occurring between O and the nearest-neighbour Cu atoms in the surface. In other words, spatial proximity is the dominant factor in the O–Cu surface binding. This is in disagreement with Stolbov *et al.* [13], in whose

Table 4.2: Centre of gravity (in eV) relative to E_F of the DOS of chemisorbed O for varying surface structures of the O/Cu(001) system.

$d_{\text{Cu-O}}$ (a.u.)	$c(2 \times 2)$	$(2\sqrt{2} \times \sqrt{2})\text{R}45^\circ$
1.5	-3.26^\dagger	-2.08^\dagger
1.15	-4.26^\dagger	–
0.17	–	-4.43^\ddagger

[†] Bulk-terminated Cu atoms.

[‡] Structure of Fig. 4.1 with $d_{\text{Cu-O}}$ representing the minimum Cu–O layer spacing.

results O p bonds more strongly to Cu3d than to Cu1d or Cu2d. They conclude that spatial proximity of orbitals was not enough to explain the results of the DOS, and that energy overlap was dominant in determining the bonding between atoms. These authors suggest that the long-range Coulomb interaction influences the atomic energy levels, hence energy overlap and the degree of covalent bonding. However, their calculation uses a muffin-tin potential [18] which is likely to be less accurate than the full-potential method implemented within the embedding technique. Our embedding calculation, in particular, gives highly accurate densities of states.

When the centre of gravity calculations of the Woodruff structure are compared with $c(2 \times 2)$, it is seen that the reconstructed surface is slightly energetically favoured as far as the one-electron energy is concerned. The values of the centre of gravity in Table 4.2 are for the $\bar{\Gamma}$ point only, but are typical for the trend seen for a calculation over the full surface Brillouin zone. However, the energy difference of 0.17 eV on reconstruction seems very small (Jacobsen and Norskov obtain 0.3 eV [19]), which suggests that the change in the one-electron energy is not the whole story in driving the reconstruction. Amongst other possible effects, ionic and size effects may be considered, though these are unfortunately difficult to interpret from the point of view of densities of states.

Bibliography

- [1] C.L. Fu and K.M. Ho, Phys. Rev. Lett. **63**, 1617 (1989),
- [2] A.Y. Lozovoi and A. Alavi Phys. Rev. B **68**, 245416 (2003).
- [3] M. Kittel, M. Polcik, R. Terborg, J.-T. Hoeft, P. Baumgärtel, A.M. Bradshaw, R.L. Toomes, J.-H. Kang, D.P. Woodruff, M. Pascal, C.L.A. Lamont and E. Rotenberg, Surf. Sci. **470**, 311 (2001).
- [4] M. Wuttig, R. Franchy and H. Ibach Surf. Sci. **224**, L979 (1989).
- [5] T. Lederer, D. Arvanitis, G. Comelli, L. Tröger and K. Baberschke, Phys. Rev. B **48**, 15390 (1993).
- [6] T. Fujita, Y. Okawa, Y. Matsumoto and K.I. Tanaka, Phys. Rev. B **54**, 2167 (1996).
- [7] U. Döbler, K. Baberschke, J. Stöhr and D.A. Outka, Phys. Rev. B **31**, 2532 (1985).
- [8] D.D. Vvedensky, J.B. Pendry, U. Döbler and K. Baberschke, Phys. Rev. B **35**, 7756 (1987).
- [9] P.S. Bagus and F. Illas, Phys. Rev. B **42**, 10852 (1990).
- [10] J.E. Inglesfield and E.A. Colbourn, Phys. Rev. Lett. **66**, 2006 (1991).
- [11] T. Wiell, J.E. Klepeis, P. Bennich, O. Björneholm, N. Wassdahl and A. Nilsson, Phys. Rev. B **58**, 1655 (1988).
- [12] S. Stolbov and T.S. Rahman, Phys. Rev Lett. **89**, 116101 (2002).
- [13] S. Stolbov and T.S. Rahman, J. Chem. Phys. **117**, 8523 (2002).
- [14] S. Stolbov, A. Kara and T.S. Rahman, Phys. Rev. B **66**, 245405 (2002).
- [15] Ch. Wöll, R.J. Wilson, S. Chiang, H.C. Zeng and K.A.R. Mitchell, Phys. Rev. B **42**, 11926 (1990).
- [16] H.B. Michaelson, J. App. Phys. **48**, 4729 (1977).
- [17] Y. Wang, G.M. Stocks, W.A. Shelton, D.M.C. Nicholson, Z. Szotek and W.M. Temmerman, Phys. Rev. Lett. **75**, 2867 (1995).
- [18] L. Szunyogh, B. Újfalussy, P. Weinberger and J. Kollár, Phys. Rev. B **49**, 2721 (1994).
- [19] K.W. Jacobsen and J.K. Nørskov, Phys. Rev. Lett. **65**, 1788 (1990).

CHAPTER 5

Graphene/Ni(111) Surface Electronic Structure

Contents

5.1 Surface Structure of Graphene/Ni(111)	66
5.2 Results	69
5.3 Conclusions	75
Bibliography	76

It has long been known that a graphitic monolayer (graphene) can be grown spontaneously on transition metal and transition metal carbide surfaces [1, 2]. In particular, on Ni(111) the graphite monolayer is easily formed on exposure to C_2H_4 at 900K [3]. At lower temperatures, carbidic layers are formed. The graphene is commensurate with the Ni(111) surface, having high crystalline quality owing to the similar surface lattice parameters, and the carbon adsorption ceases once one monolayer coverage has been reached [3]. One of the first studies [4] of the graphitic overlayer was carried out when Rosei *et al.* [5] realised that the “coking” occurring during CO hydrogenation on Ni (used as a methanation catalyst) when the reaction runs too hot, was actually the graphitic monolayer. While the carbidic form of carbon coverage on Ni is active for CO methanation, the graphitic overlayer is not, behaviour characteristic of bulk graphite.

The graphene properties are those specifically investigated in this chapter. Being similar to bulk graphite, graphene and other graphite based materials are proving to have significant importance in microelectronic devices [6]. Here, we study the bonding of the graphene/Ni(111) surface using a spin-polarised electronic structure calculation. The work function, magnetic moments, and majority-spin band structures are investigated.

5.1 Surface Structure of Graphene/Ni(111)

Recently, structural studies of graphene on a Ni(111) substrate have been carried out, mostly indicating that the C atoms adsorb onto the Ni(111) substrate at the on-top (T) sites and fcc hollow (F) sites (Fig. 5.1) within a 1×1 surface structure (geometry I) [3, 4, 7]. Other geometries (geometry II and III) have been proposed [8, 9] (Fig. 5.2), but there is contradicting experimental evidence about these [3, 4].

This chapter will concentrate on geometry I, using the parameters described by Bertoni *et al.* [7] who used the Wien2k code to calculate the relaxed surface spin-polarised electronic structure of graphene/Ni(111). In all studies so far, there has been no reported alteration in the basal symmetry of the graphitic overlayer, although buckling of the carbon atoms is seen in some results [4, 7] but not reported

Table 5.1: C–Ni interlayer spacing (averaged over non-equivalent C atoms) and atomic spacing parameters as reported in the literature for different structural studies of the graphene/Ni(111) surface.

Ref.	d_{C-Ni} (averaged) (Å)	Reported structure
[4]	2.11 ± 0.07	I
[3]	2.1 ± 0.1	I
[7]	2.216	I
[5]	2.8 ± 0.08	III
bulk d_{C-C} (inter-graphene sheets)	3.35	—
bulk d_{Ni-Ni}	2.032	—

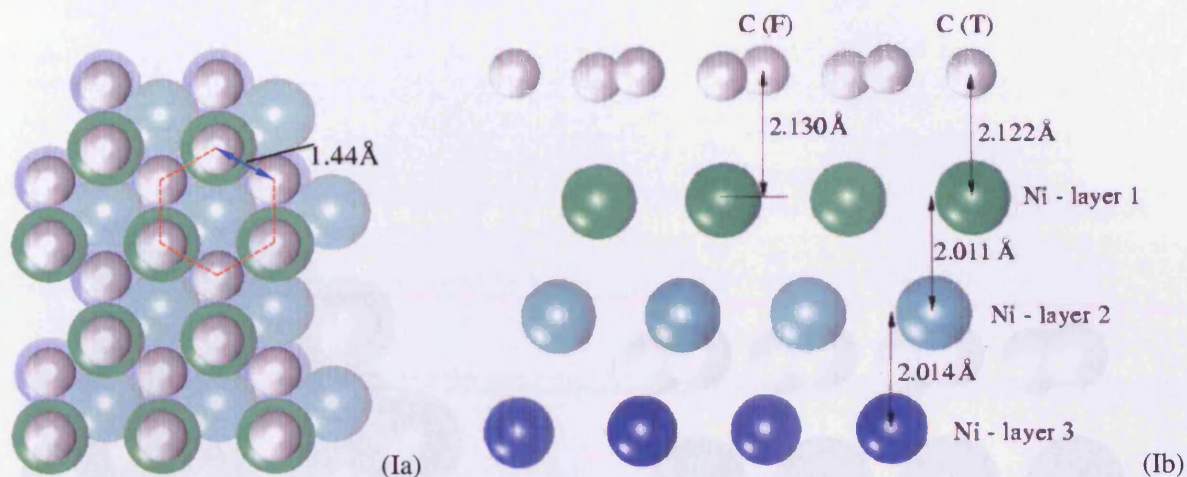


Figure 5.1: Proposed structure of graphene/Ni(111) – geometry I. (a) Top view, (b) side view. In (b), the top layer are the C atoms in the graphene overlayer, subsequent rows are Ni atoms in the 1st layer (surface), 2nd, and 3rd layers, respectively. The C atoms at the fcc hollow site (F) are positioned further away from the Ni surface than those in the on-top (T) site. Structural parameters obtained from Bertoni [7] *et al.*

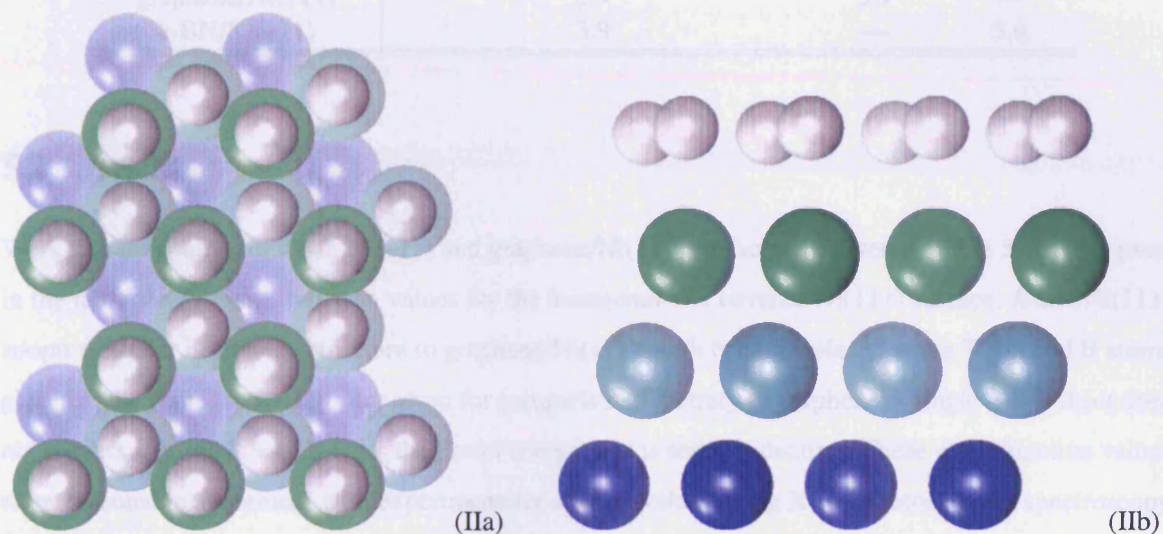
in others [3, 5, 8, 9]. Keeping with the results of the Wien2k code, the structure of our graphene/Ni(111) system incorporates the reported buckling, although the differences in distances of the two C atoms with the Ni(111) surface layer is minimal (C in the T site lies 2.122 Å above this Ni layer; C in the F site lies 2.13 Å above the outermost surface Ni layer). Gamo *et al.* [4], whose results also report the C buckling, show the same order of layering between the two C atoms, but again with minimal differences (Δd_{C-Ni} for the two C atoms is 0.05 Å, which is less than the associated positional error of 0.07 Å in the surface normal direction).

Detailed structural data, as described by ref. [7], is given in Fig. 5.1 and Table 5.1. The nearest-neighbour spacing within the graphene overlayer on Ni(111) is increased relative to the bulk graphite value due to the slightly larger spacing of the Ni(111) surface. The nearest-neighbour spacing of the C–C bulk is 1.42 Å [8], whereas the equivalent spacing on Ni(111) is 1.44 Å ($= a_{Ni}/\sqrt{6}$; $a_{Ni} = 3.52$ Å), increasing the *ideal* C–C bond distance by 0.02 Å ($\approx +1.4\%$). The small difference in spacing between the graphite interatomic spacing and the Ni(111) interatomic spacing is the reason why graphene overlayers can be grown on the Ni(111) substrate. It is also reported in the literature that graphene can be successfully grown on some other metal surfaces and metal carbide substrates: Ni(110), Ni(100), Pt(111), TiC(111), TaC(111), and TaC(100), with this list by no means conclusive. These results have been obtained by LEED [10]–[17], Auger spectroscopy [11]–[17], electron energy loss spectroscopy [10, 18], STM [19], and photoemission spectroscopy [11, 12, 20, 21].

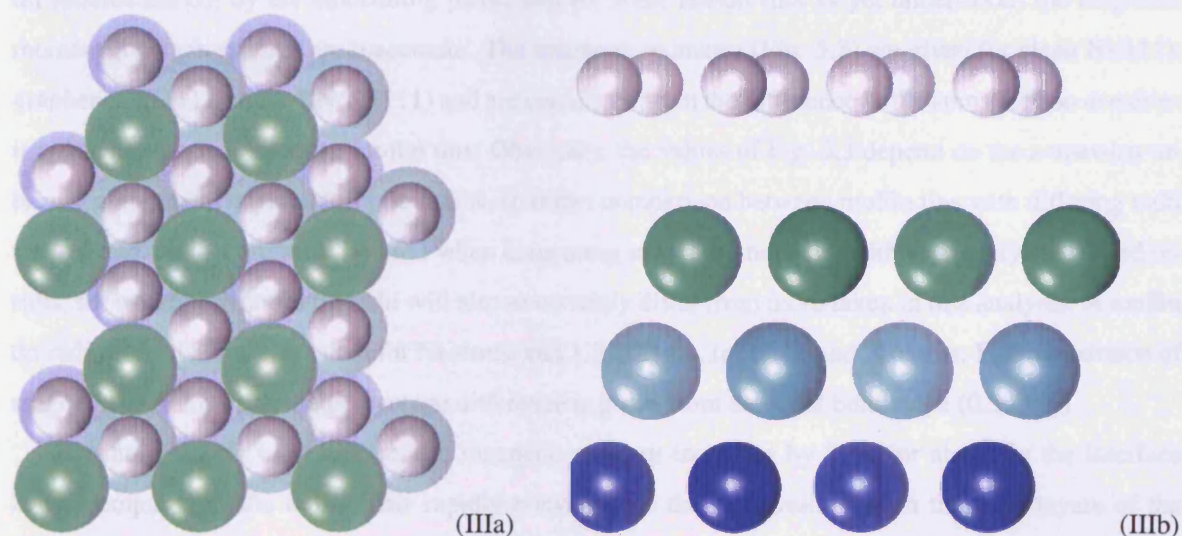
Figure 5.1: Proposed structure of graphene/Ni(111) – geometry I and II. (a) Top view, (b) side view.

Table 5.2: Work function values (eV) of pure Ni(111), graphene/Ni(111), and $\sqrt{3}\times\sqrt{3}$ Ni/Ni(111) surfaces. A comparison is made between calculated work function values from the surface applied field model and experimentally obtained results [22, 27].

Surface	Work function (eV) obtained from:	
	Embedding model [22]	Ref. [27]
Ni(111) clean (6 layers)	5.3	5.3
graphene/Ni(111) SP	5.9	—
Ni/Ni(111) SP	5.9	5.6



Magnetic moments obtained from density-functional calculations for all atoms are given in the last column in Fig. 5.3. The μ_B atoms attached to the underlying graphene (indicated orange during our course) have smaller values than for the underlying atoms, and for some reason that is yet unknown, the magnetic moments are smaller.



Similar results have been seen elsewhere [27]. For the clean metal, the Ni magnetic moment of the graphene/Ni(111) surface becomes greatly reduced from the bulk value ($\sim 10.6\mu_B$). However, at 171 K, a similar peak ($\sim 10\mu_B$) with the magnetic moment of the third layer Ni atom suddenly becomes very close to bulk.

Figure 5.2: Possible structures of graphene/Ni(111) – geometries II and III. (a) Top view, (b) side view.

Table 5.2: Work function values (eV) of clean Ni(111), graphene/Ni(111), and *h*-BN/Ni(111) surfaces. A comparison is made between calculated work function values from the surface embedding code, and experimentally obtained results [22, 27].

Surface	Work function (eV) obtained from:		
	Embedding code / eV	Ref. [22]	Ref. [27]
Ni(111) clean (4 layer)	5.5	5.3	5.3
graphene/Ni(111)	3.9	3.9	—
<i>h</i> -BN/Ni(111)	3.9	—	3.6

5.2 Results

Work function values of clean Ni(111) and graphene/Ni(111) surfaces are given in Table 5.2. Also given in the table are the work function values for the *hexagonal*-BN covered Ni(111) surface. *h*-BN/Ni(111) adopts a similar hexagonal structure to graphene/Ni(111), with N atoms placed at the T site and B atoms placed at the F site, and results are given for comparison. Contrary to graphene, a single *h*-BN sheet does not possess any bands which cross the Fermi energy, and is semiconducting. These work function values show reasonable agreement with experimentally derived values using X-ray photoelectron spectroscopy [27], and angle-resolved ultraviolet photoelectron spectroscopy (ARUPS) [22].

Magnetic moments obtained from the embedding code for Ni atoms are given in the bar chart in Fig. 5.3. The Ni atoms adjacent to the embedding plane are omitted since, during run-time, these muffin tin spheres are cut by the embedding plane, and for some reason (not as yet understood) the magnetic moments on such spheres are inaccurate. The magnetic moments (Fig. 5.3) are given for clean Ni(111), graphene/Ni(111), and *h*-BN/Ni(111) and are calculated from the difference in the spin electron densities integrated over the respective muffin tins. Obviously, the values of Fig. 5.3 depend on the somewhat arbitrary assignment of the muffin tin radius, so direct comparison between muffin tins with differing radii are avoided. Also, care must be used when comparing magnetic moments with separately calculated results, for which the muffin tin radii will almost certainly differ from those taken in this analysis. A muffin tin radius of 2.1855 a.u. is taken for Ni atoms and 1.32557 a.u. for C, B, and N atoms. For comparison of magnetic moment values, a percentage difference is given from the ideal bulk value ($0.593\mu_B$).

For the clean Ni(111) surface, the magnetic moment increases by 20% for atoms in the interface layer, compared to the bulk. This rapidly converges to the bulk value within three Ni layers of the surface. Similar results have been seen elsewhere [7]. On the other hand, the Ni magnetic moment of the graphene/Ni(111) surface seems greatly reduced from the bulk value (-16.6%). Bertoni *et al.* [7] find a similar result (-16%), with the magnetic moment of the third layer Ni atom suddenly becoming very close to the bulk value of $0.593\mu_B$. It is expected that a similar situation arises for the embedding code, but this will not be known until a further calculation is performed with more Ni layers. *h*-BN/Ni(111) Ni

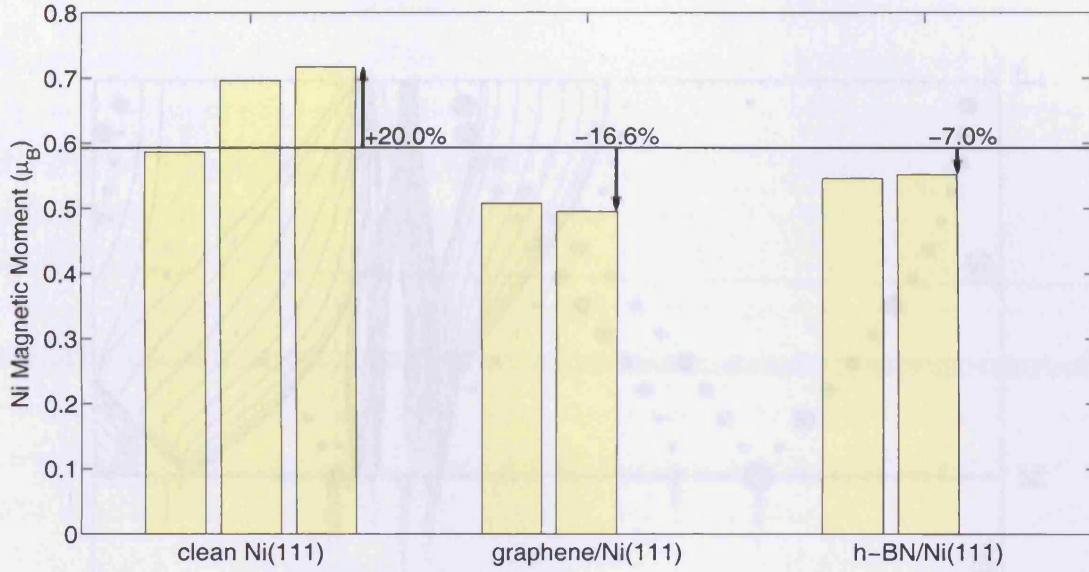


Figure 5.3: Spin magnetic moments of Ni atoms at various surfaces, obtained from the surface embedding code. The right of each block of data is the spin magnetic moment of the outermost Ni surface layer. The solid horizontal line is the bulk spin magnetic moment. All values are calculated from the difference in the spin density integrated over the Ni muffin tin. Muffin tin radius of all Ni atoms is 2.1855 a.u. Shown are the Ni atom magnetic moments of clean Ni(111), graphene/Ni(111) and *h*-BN/Ni(111).

atoms show a similar reduction in magnetic moment at the surface (7.0% reduction from the bulk value). The reduced magnetic moments for these surfaces (graphene and *h*-BN covered Ni(111)) is presumably due to electron transfer from the Ni(111) surfaces to the overlayers, with different affinities for different spin states.

We now move on to the surface band structures and density of states for graphene/Ni(111). Figure 5.4 shows a collection of results for bulk Ni and the surface graphene/Ni(111) majority spin electronic structures. Of the six plots in Fig. 5.4, 1, 3, and 5 each show the density of states of the surface Ni atom and the two non-equivalent C atoms integrated through the respective muffin-tins at $\bar{\Gamma}$, \bar{M} and \bar{K} respectively. Plots 2, 4 and 6 show the Ni bulk band structure (solid lines) along $\bar{\Gamma}\bar{M}$, $\bar{M}\bar{K}$ and $\bar{K}\bar{\Gamma}$ respectively. The continuous lines show the bands at various values of k_z as a function of $k_{||}$.

The dispersion of the prominent features in the density of states associated with the C atoms is shown by the filled circles on plots 2 and 6, giving the dispersion along the $\bar{\Gamma}\bar{M}$ and $\bar{K}\bar{\Gamma}$ symmetry directions. The size of the circles indicates the relative magnitude of the density of states within the C muffin-tins. The surface related features can be described as Shockley and image surface states, and also graphene-Ni(111) interface states.

Starting with $\bar{\Gamma}$, the small peak in the density of states at 3.7 eV, shown on plot 1 of Fig. 5.4, can be described as an image state. This has been observed by experiment [28] on clean Ni(111) and in other theoretical calculations [7] of graphene/Ni(111). Inverse-photoemission spectroscopy [28] puts

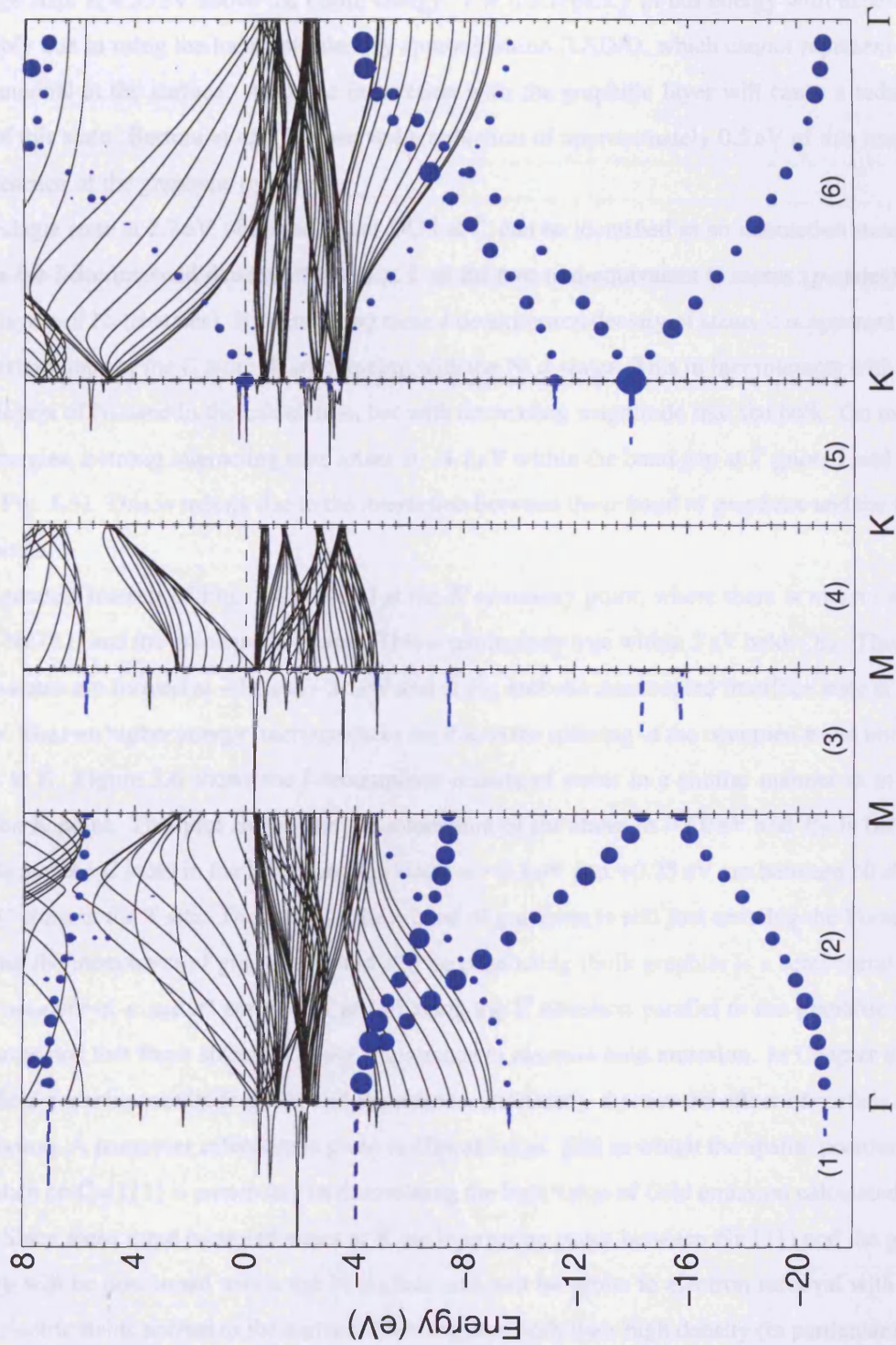


Figure 5.4: Bulk band structure of Ni (solid lines on plots 2, 4, and 6), surface band structure of the graphene monolayer on Ni(111) (filled circles on plots 2 and 6), and the surface density of states of the C atoms (dashed lines) and surface Ni atoms (solid lines) of the graphene/Ni(111) surface at certain high symmetry points (plots 1, 3, and 5). All quantities are for majority spin.

this image state at 4.55 eV above the Fermi energy. The discrepancy in our energy with experiment is presumably due to using the local spin-density approximation (LSDA), which cannot represent the true image potential at the surface. Also, the interaction with the graphitic layer will cause a reduction in energy of this state. Bertoni *et al.* [7] observed a reduction of approximately 0.5 eV of this image state in the presence of the graphene overlayer.

The single state at 2.2 eV, observed in our DOS at $\bar{\Gamma}$, can be identified as an interaction state. Figure 5.5 gives the l -decomposed density of states at $\bar{\Gamma}$ of the two non-equivalent C atoms (p -states) and the top two layers of Ni (d -states). By comparing these l -decomposed density of states it is apparent that this is an interface state of the C atom (F site) mixing with the Ni d -states. This in fact interacts with all three surface layers of Ni used in the calculation, but with decreasing magnitude into the bulk. On moving to bound energies, a strong interacting state arises at -4.1 eV within the band gap at $\bar{\Gamma}$ (plots 1 and 2 of Fig. 5.4, and Fig. 5.5). This is mainly due to the interaction between the σ band of graphene and the top layer Ni d -orbitals.

The greatest interest of Fig. 5.4 is found at the \bar{K} symmetry point, where there is much interaction between Ni(111) and the graphene overlayer. This is particularly true within 3 eV below E_F . Three bound interface states are formed at -3.0 eV, -2.1 eV and at E_F , and one unoccupied interface state is found at $+0.25$ eV. The two higher energy interface states are due to the splitting of the occupied π and unoccupied π^* states at \bar{K} . Figure 5.6 shows the l -decomposed density of states in a similar manner as in Fig. 5.5 but for the \bar{K} point. This plot shows that the interaction of the states at -3.0 eV and E_F is between Ni d -orbitals and the C atom in the F site, and the states at -2.1 eV and $+0.25$ eV are between Ni d -orbitals and the C atom in the T site. The fact that the π band of graphene is still just crossing the Fermi energy means that the monolayer of graphite should still be conducting (bulk graphite is a semi-metal because of the cross-over of π and π^* states at \bar{K} at E_F) along the \bar{K} direction parallel to the graphitic sheet. It is also suspected that these states will have importance in electron field emission. In Chapter 8 we will present field emission results from Pd and Pt surfaces, and briefly discuss the effect of surface states in field emission. A particular reference is given to Ohwaki *et al.* [30] in which the spatial positioning of a surface state on Cu(111) is paramount in determining the high value of field emission calculated for this surface. Since these three occupied states at \bar{K} are interacting states between Ni(111) and the graphene layer they will be positioned above the Ni surface and will be prone to electron removal with applied external electric fields normal to the surface. This, together with their high density (in particular the state on E_F) and their high energy, means that electron transmission may increase for graphene/Ni(111) over clean Ni(111). However, it may be that field emission from this state will be limited, because of its high surface parallel wavevector component. In Chapter 8 we will see that transmission is highly dependent

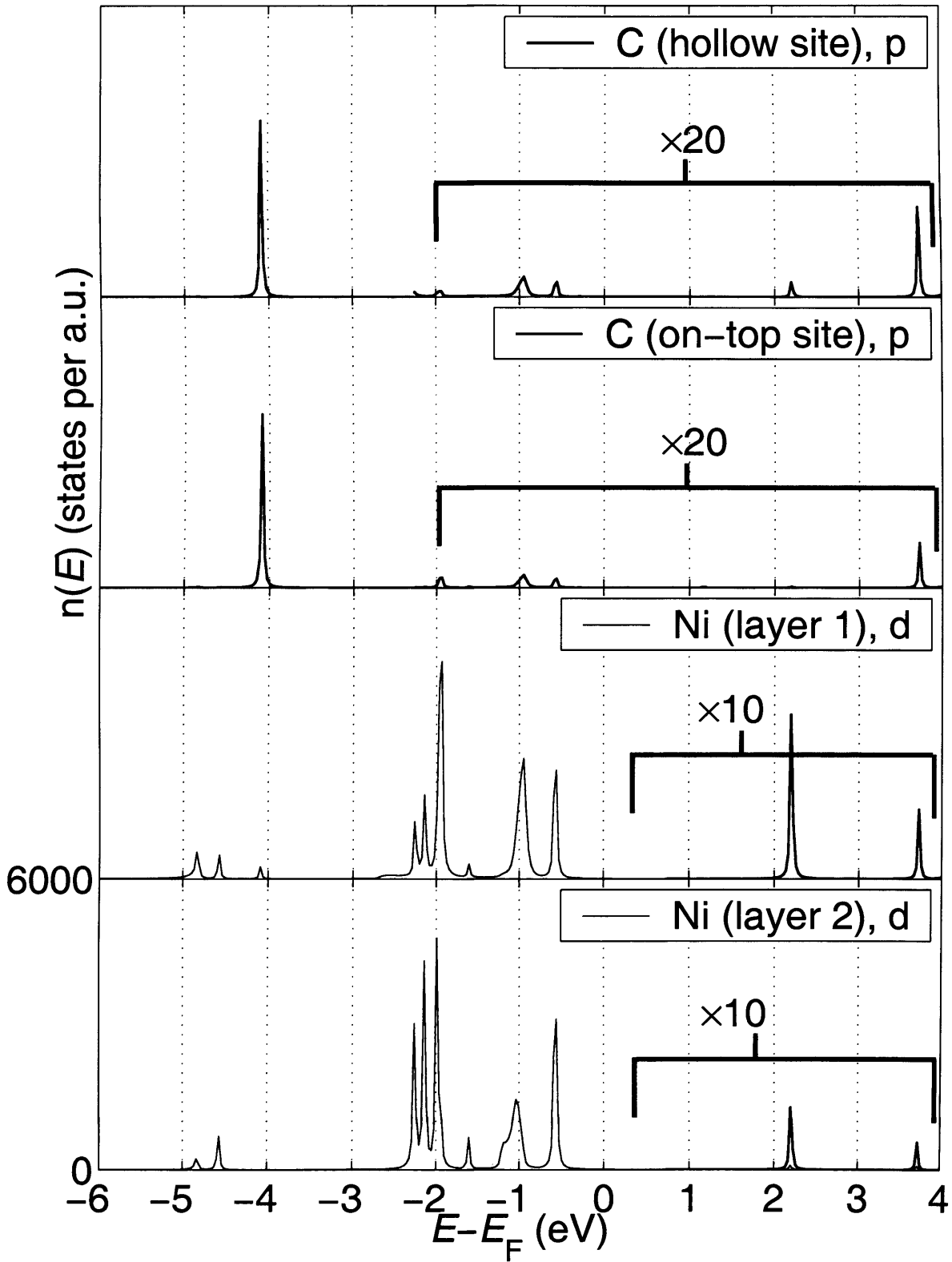


Figure 5.5: l -decomposed density of states integrated through the muffin-tins of atoms in the graphene/Ni(111) surface at the Γ point. The top panel is the C atom in the hollow site (p -states), the second panel is the C atom in the on-top site (p -states). The third and fourth panels are the Ni DOS (d -states) of the surface and second row respectively.

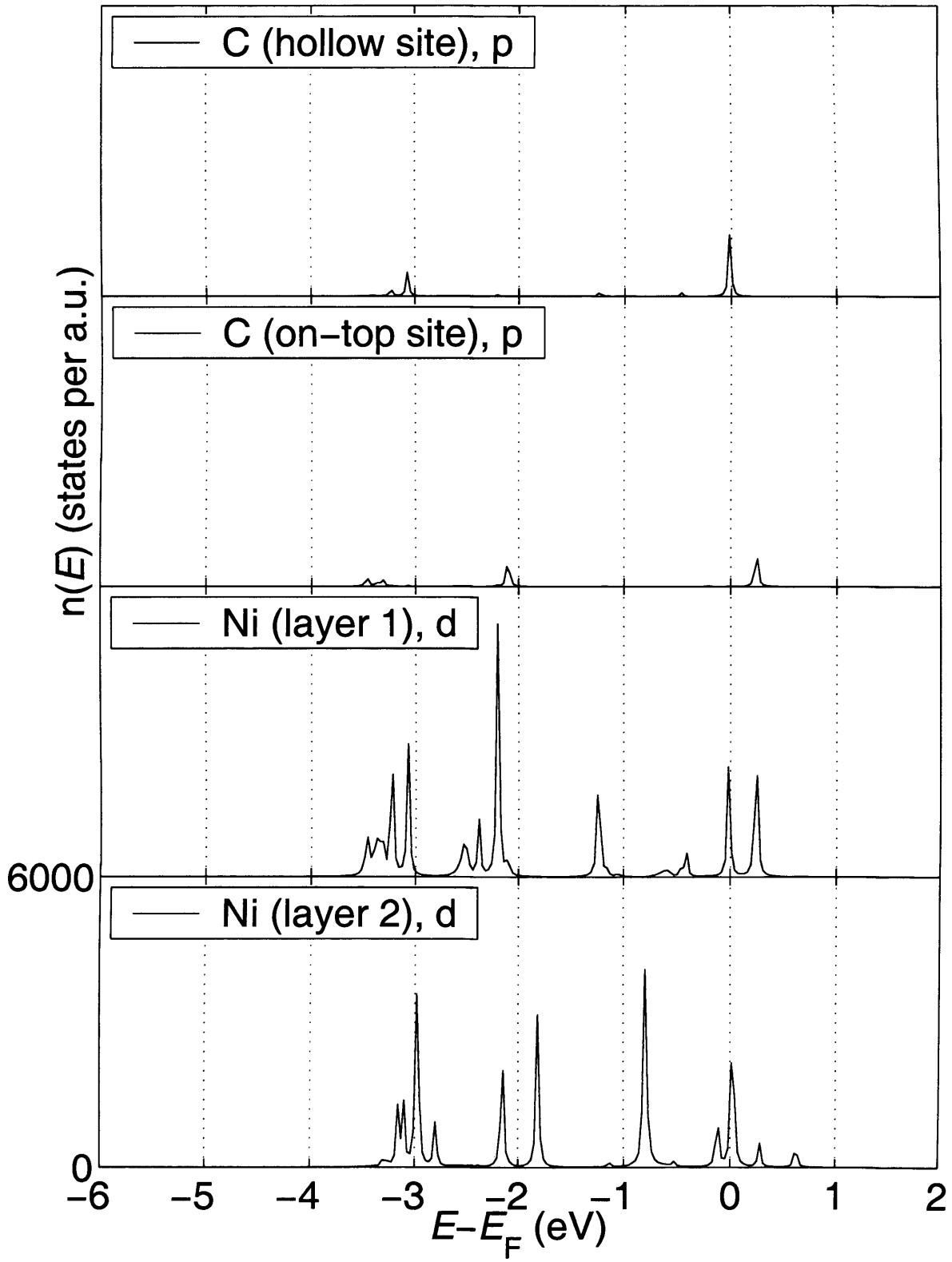


Figure 5.6: l -decomposed density of states integrated through the muffin-tins of atoms in the graphene/Ni(111) surface at the \bar{K} point. The top panel is the C atom in the hollow site (p -states), the second panel is the C atom in the on-top site (p -states). The third and fourth panels are the Ni DOS (d -states) of the surface and second row respectively.

on surface parallel wavevector, and decreases with increasing parallel component.

5.3 Conclusions

In this chapter the electronic structure of a single overlayer of graphite on a Ni(111) substrate has been investigated. Results were compared to a similar calculation of Bertoni *et al.* [7] who used the Wien2k code in their analysis, and our structural parameters were obtained from their results. Consequently, results should be in excellent agreement with these researchers' results, and this was found to be the case.

The graphene/Ni(111) system is of interest because of the close connection to carbon nanotubes on metal substrates. A single-walled carbon nanotube is constructed by rolling a graphene sheet into a cylinder [29]. These structures are becoming of increased importance because of their applications in microelectronic devices [6]. Since graphite is a semi-metal, the carbon nanotube is conducting for certain structures and has been found to be an extremely efficient field emitter [31]. From our results, we suggest that an interesting scenario may arise with carbon nanotubes on the Ni(111) substrate. If rolled correctly, with the \bar{K} wavevector directed normal to the surface [32], the interaction (specifically the interacting state at E_F) between the C atoms and Ni(111) substrate could have significant applications in field emission. However, although conductance of C nanotubes has been proven, and their importance in field emission has already been established, whether or not the C nanotube/Ni(111) interaction will have any significance on field emission remains to be seen. The question remains though, whether the interface states would still exist if the symmetry of the graphene / carbon nanotube were to alter on the Ni(111) surface.

Bibliography

- [1] A. Nagashima, N. Tejima and C. Oshima, Phys. Rev. B **50**, 17487 (1994).
- [2] N.J. Wu, V. Kumykov and A. Ignatiev, Surf. Sci. **163**, 51 (1985).
- [3] H. Kawanowa, H. Ozawa, T. Yazaki, Y. Gotoh and R. Souda, Jpn. J. Appl. Phys. **41**, 6149 (2002).
- [4] Y. Gamo, A. Nagashima, M. Wakabayashi, M. Terai and C. Oshima, Surf. Sci. **374**, 61 (1997).
- [5] R. Rosei, M. De Crescenzi, F. Sette, C. Quaresima, A. Savoia and P. Perfetti, Phys. Rev. B **28**, 1161 (1983).
- [6] P.G. Collins and A. Zettl, Phys. Rev. B **55**, 9391 (1997).
- [7] G. Bertoni, L. Calmels, A. Altibelli and V. Serin, Phys. Rev. B **71**, 075402 (2004).
- [8] Y. Souzu and M. Tsukada, Surf. Sci. **326**, 42 (1995).
- [9] K. Yamamoto, M. Fukishima, T. Osaka and C. Oshima, Phys. Rev. B **45**, 11358 (1992).
- [10] T. Aizawa, R. Souda, S. Otani and Y. Ishizawa, Phys. Rev. B **42**, 11469 (1990).
- [11] L.C. Isett, Surf. Sci. **161**, 373 (1985).
- [12] C.F. McConville, D.P. Woodruff and S.D. Kevan, Surf. Sci. **171**, L447 (1986).
- [13] M. Eizenberg and J.M. Blakely, Surf. Sci. **82**, 228 (1979).
- [14] J.C. Shelton, H.R. Patil and J.M. Blakely, Surf. Sci. **43**, 493 (1974).
- [15] J.C. Hamilton and J.M. Blakely, Surf. Sci. **91**, 199 (1980).
- [16] H. Zi-pu, D.F. Ogletree, M.A. Van Hove, and G.A. Somorjai, Surf. Sci. **180**, 433 (1987).
- [17] N.A. Kholin, E.V. Rut'kov, and A. Y. Tontegode, Surf. Sci. **139**, 155 (1984).
- [18] L. Papagno and L.S. Caputi, Phys. Rev. B **29**, 1483 (1984).
- [19] H. Itoh, Surf. Sci. **254**, 437 (1991).
- [20] F.J. Himpsel, K. Christmann, P. Heimann and D.E. Eastman Surf. Sci. **115**, L159 (1982).
- [21] R. Rosei, S. Modesti, F. Sette, C. Quaresimam, A. Savoia and P. Perfetti, Phys. Rev. B **29**, 3416 (1984).
- [22] C. Oshima and A. Nagashima, J. Phys.: Condens. Matter **9**, 1 (1997).

- [23] G.B. Grad, P. Blaha, K. Schwarz, W. Auwärter and T. Greber, *Phys. Rev. B* **68**, 085404 (2003).
- [24] M. Muntwiler, W. Auwärter, F. Baumberger, M. Hoesch, T. Greber and J. Osterwalder, *Surf. Sci.* **472**, 125 (2001).
- [25] E. Rokuta, Y. Hasegawa, K. Suzuki, Y. Gamou and C. Oshima, *Phys. Rev. Lett.* **79**, 4609 (1997).
- [26] W. Auwärter, T.J. Kreutz, T. Greber and J. Osterwalder, *Surf. Sci.* **429**, 229 (1999).
- [27] A. Nagashima, N. Tejima, Y. Gamou, T. Kawai and C. Oshima, *Phys. Rev. Lett.* **75**, 3918 (1995).
- [28] S. Yang, K. Garrison and R.A. Bartynski, *Phys. Rev. B* **43**, 2025 (1991).
- [29] C. Dekker, *Physics Today*, May, 22 (1999).
- [30] T. Ohwaki, H. Ishida and A. Liebsch, *Phys. Rev. B* **68**, 155422 (2003).
- [31] J.M. Bonard, M. Croci, C. Klinke, R. Kurt, O. Noury and N. Weiss, *Carbon* **40**, 1715 (2002).
- [32] The conductance of carbon nanotubes was theoretically established separately by Mintmire *et al.* [33] and Hamada *et al.* [34] in 1992. The conductance is dependent on the tube diameter and helical arrangement.
- [33] J.W. Mintmire, B.I. Dunlap and C.T. White, *Phys. Rev. Lett.* **68**, 631 (1992).
- [34] N. Hamada, S. Sawada and A. Oshiyama, *Phys. Rev. B* **68**, 1579 (1992).

CHAPTER 6

Surface Steps – Jellium Model

Contents

6.1	The Jellium Model	79
6.2	Electron Density	80
6.3	Work Function Reduction	82
	Bibliography	85

The study of stepped surfaces, for both characterisation of defects and understanding their useful properties such as increased reactivity, has been carried out extensively over the last two to three decades. This work has mainly been based on vicinal surfaces, in which the surface normal direction is close to that of low index planes. Experimentally, investigations have used photoemission of adsorbed Xe (PAX) [1, 2], scanning tunneling microscopy (STM) [3, 4] and electrochemical techniques [5]. These have all helped to explain the relevance of steps on surface effects, such as the reduced work function, increased reactivity, and also crystal growth. This has been reproduced by theory within the last decade, and although recent calculations have considered more sophisticated *ab-initio* techniques on stepped surfaces, such as the pseudopotential method [6], we can still learn much from jellium calculations [7]. In the jellium model the atomistic structure is smeared out into a smooth positive background charge in which the electrons move self-consistently. Later chapters will involve atomistic models of stepped surfaces, but for now we shall concentrate on jellium, giving an account of the work function dependence on the step density.

6.1 The Jellium Model

The simplicity of the jellium model of stepped surfaces means that surfaces of low step density are able to be modelled (here we calculate surfaces with terrace lengths equivalent to 10 lattice spacings). This is in contrast to the LAPW method employed in later chapters (Chapters 7 and 8), in which calculations are limited to surfaces with terrace lengths of just three lattice spacings. The stepped jellium surface is the first stage in calculating the electronic structure at stepped surfaces. The details of solution are described in Appendix B.

The jellium model was used in early surface electronic structure calculations [9] as a model of simple metals (*sp*-bonded) such as Al and Na. Rather than dealing with the complex atomistic structure of *real* materials, the jellium model smears out the nuclear charge, forming a constant positive charge density of magnitude $|n|$. The electrons move in the electrostatic potential of the positive background, and the Hartree and exchange-correlation potential of the electron density.

At the surface, the background charge density ρ_b stops abruptly at the jellium edge z_s :

$$\rho_b = \begin{cases} |n| & z \leq z_s \\ 0 & z > z_s \end{cases} \quad (6.1)$$

taking z as the positive surface normal distance directed away from the bulk. Equation (6.1) describes a flat jellium surface. The more complicated stepped surface structure is given in Appendix B together with the computational details of the basis functions and embedding potentials. Within this background positive charge density, the electron density is variationally calculated to self-consistency.

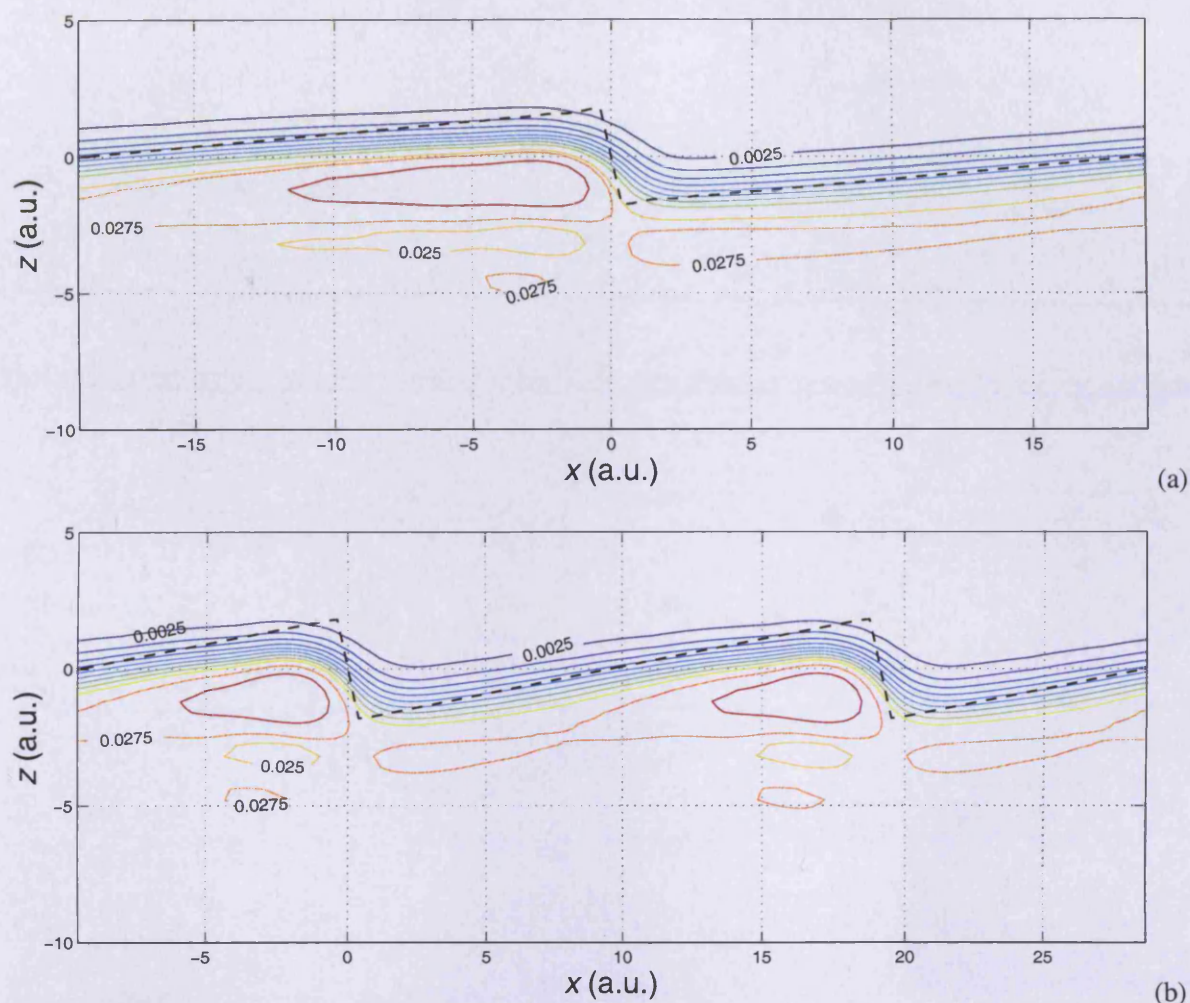


Figure 6.1: Contour maps of electron density for (a) Al(10,1) and (b) Al(5,1) stepped surfaces. For surface nomenclature, see text. Plots are taken over a vertical-cut plane. Contour spacings are 0.0025 a.u. The dashed line in each plot represents the jellium edge of the stepped surface.

The calculation uses a plane-wave basis set embedded between the jellium and vacuum embedding planes (see Appendix B). The local density approximation to the exchange-correlation functional is used, implementing the Ceperley-Alder-Perdew-Zunger parametrisation [11, 12].

6.2 Electron Density

Contour maps of the charge density are shown for Al jellium stepped surfaces in Fig. 6.1. The nomenclature used is Al(t,s) where t is the length of the surface terrace, given in integral numbers of lattice spacings (for Al the lattice spacing a_{Al} is taken as 3.83 a.u.), and s is the height of the step. The step height is nominally taken as one lattice spacing. These figures demonstrate how the electron charge smoothes itself over the surface, creating charge dipoles at the step as it does so. This is the well-known

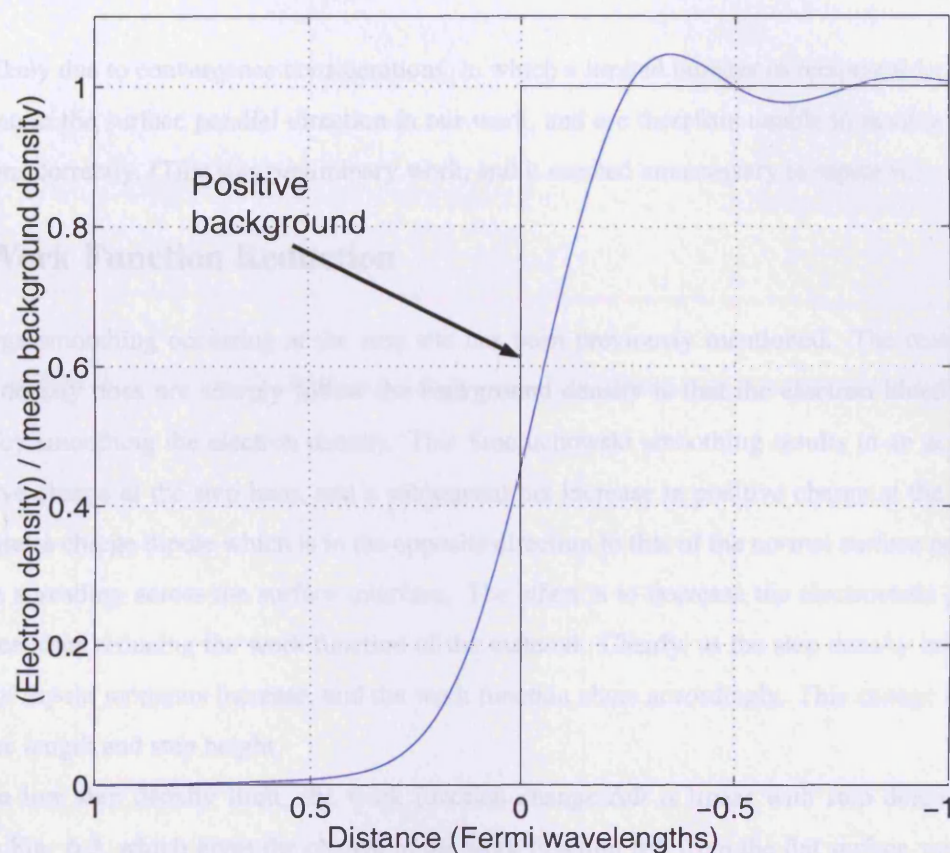


Figure 6.2: Charge density along a vertical line perpendicular to the Al(10,1) stepped surface, crossing a central position in the terrace. The positive background charge is also shown. The unit of length is the Fermi wavelength ($= \pi/k_F$, where $k_F = (3\pi^2 n)^{1/3}$). n is the positive background charge density deep within the bulk.

Smoluchowski effect [13]. The abrupt edge of the positive background charge is also represented on these diagrams. The main conclusion which can be drawn from these density plots is the local nature of the charge smoothing. The electron density transition from the upper to the lower terrace seems to be confined to within a few atomic units on either side of the step site. Outside this region, the electron density follows the jellium edge precisely and is reminiscent of the charge plots of Lang and Kohn [9] from 1970 of flat surfaces. As an example, Fig. 6.2 shows the electron density along a vertical line perpendicular to a stepped surface. The line is taken at a central position of the Al(10,1) terrace.

Further interesting aspects of the plots of Fig. 6.1 are the Friedel oscillations. The 2-dimensionality of the stepped surfaces gives rise to electron scattering from the abrupt potential change at the jellium edge in two directions. The usual Friedel oscillations [9] in the surface normal direction can be seen from Fig. 6.2, whereas the extra oscillations resulting from the step edges are apparent in Fig. 6.1. The overall effect is the superposition of the Friedel oscillations in the two directions. We note however, that the charge oscillations due to the step sites are not as clear as in the earlier work of Ishida [7] *et al.* This

is most likely due to convergence considerations, in which a limited number of reciprocal lattice vectors were taken in the surface parallel direction in our work, and are therefore unable to resolve the Friedel oscillations correctly. (This was preliminary work, and it seemed unnecessary to repeat it.)

6.3 Work Function Reduction

The charge smoothing occurring at the step site has been previously mentioned. The reason that the electron density does not sharply follow the background density is that the electron kinetic energy is reduced by smoothing the electron density. This Smoluchowski smoothing results in an accumulation of negative charge at the step base, and a subsequent net increase in positive charge at the step ledge. This creates a charge dipole which is in the opposite direction to that of the normal surface potential due to charge spreading across the surface interface. The effect is to decrease the electrostatic potential at the surface, thus reducing the work function of the material. Clearly, as the step density increases, the number of dipole moments increase, and the work function alters accordingly. This change depends on the terrace length and step height.

In the low step density limit, the work function change $\Delta\Phi$ is linear with step density. This is shown in Fig. 6.3, which gives the change in the work function $\Delta\Phi$ from the flat surface value, plotted against the step density. $\Delta\Phi$ can therefore be associated with the dipole moment μ associated with the steps. From the slope of Fig. 6.3, we find the dipole moment associated with each step site (per a_{Al} ledge-length in the y-direction) is -0.046 Debye. This is in reasonable agreement to that obtained by Ishida *et al.* [7], who gives μ_{Al} as -0.057 D per unit cell ledge length. However, recent pseudopotential calculations by Stumpf *et al.* [6] on atomistic Al surfaces give contradicting results. These authors find that the (001) step facets on a Al(111) surface give rise to a dipole moment of $+0.045$ D/step atom – a dipole moment which actually *increases* the work function. This result is explained by the attraction of electrons towards the less coordinated edge atoms, in which case the electron density smoothing does not follow the Smoluchowski model. Even though the Smoluchowski effect may not be descriptive of the physics at Al steps, according to Stumpf *et al.*, this is still likely to be an accurate description of the effects at more polarisable metals, such as the transition metals. For highly polarisable metals, the screening length due to the electronic charge will decrease, and should therefore be more effective compared to the *sp* electrons described by the jellium model. This is in fact a conclusion of the following chapter using an LAPW model of stepped surfaces.

Returning to Fig. 6.3, for high step density the reduction in work function becomes less than linear. This is because the charge redistribution at the step overlaps with neighbouring sites, and the step dipole is modified.

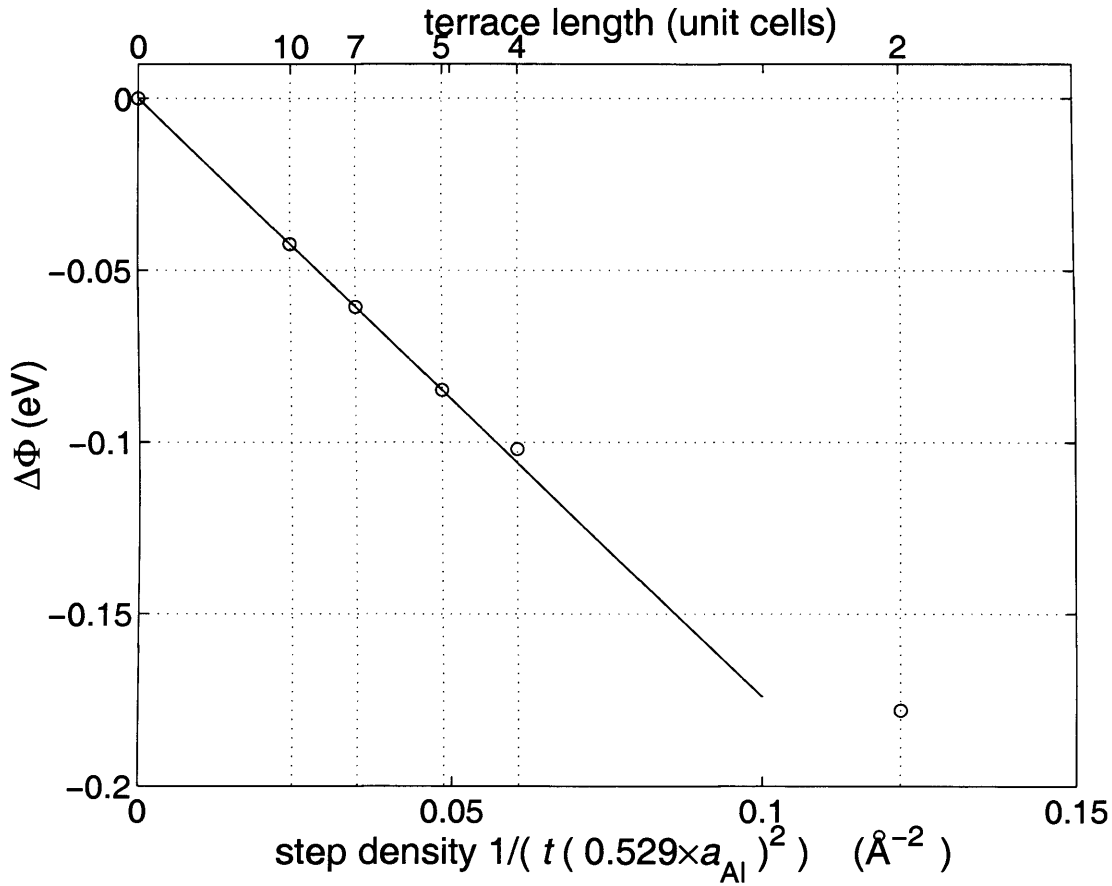


Figure 6.3: Calculated work function change for Al jellium stepped surfaces as a function of step density.

In conclusion, it has been shown that the jellium model predicts a reduction in work function with increasing step density, in accordance with experimental [14, 15] and theoretical [7] results. The linear relationship between step density and work function reduction observed in the literature has also been reproduced. The linear dependence suggests a localised charge redistribution at the step site. Even though separate work has been carried out which discredits the Smoluchowski effect for Al, the results of Stumpf *et al.* [6] still show the linear relationship between step density and work function. This means that the electronic effects at step sites remain localised.

Literature results of work functions of stepped surfaces provide evidence that the Smoluchowski effect is valid for transition metals, confirmed by our results based on Pd and Pt in later chapters. As an example, steps on Au(111) and Pt(111) show dipole moments of -0.25 D and -0.6 D, respectively [14]. These dipole moments lower the work function on increasing step density. A linear relationship is also seen for these results, suggesting the charge redistribution is a local effect for these surfaces.

This chapter has introduced the concept of how local aspects of surface physics may influence macroscopic properties. In this case, the local charge redistribution found at step sites on the jellium model was

able to reduce the work function. In the following chapters we shall build on this result and investigate the precise effects of the effective potential at the step site, and its influence on surface properties.

Bibliography

- [1] K. Wandelt, Appl. Surf. Sci. **111**, 1 (1997).
- [2] J. Küppers, K. Wandelt and G. Ertl, Phys. Rev. Lett. **43**, 928 (1979).
- [3] J.F. Jia, K. Inoue, Y. Hasegawa, W.S. Yang and T. Sakurai, Phys. Rev. B **58**, 1193 (1998).
- [4] Ph. Avouris, I.-W. Lyo and P. Molinàs-Mata, Chem. Phys. Lett. **240**, 423 (1995).
- [5] G.A. Attard, O. Hazzazi, P.B. Wells, V. Climent, E. Herrero and J.M. Feliu, J. Electroanal. Chem. **568**, 329 (2004).
- [6] R. Stumpf and M. Scheffler, Phys. Rev B **53**, 4958 (1996).
- [7] H. Ishida and A. Liebsch, Phys. Rev. B **46**, 7153 (1992).
- [8] K. Hermann, B. Gumhalter and K. Wandelt, Surf. Sci. **251/252**, 1128 (1991), and references therein.
- [9] N.D. Lang and W. Kohn, Phys. Rev. B **1**, 4555 (1970).
- [10] D.J. Singh, *Planewaves, Pseudopotentials, and the LAPW method*, Kluwer Academic, Norwell (1994).
- [11] J.P. Perdew and A. Zunger, Phys. Rev. B **23**, 5048 (1981).
- [12] D.M. Ceperley and B.J. Alder, Phys. Rev. Lett. **45**, 566 (1980).
- [13] R. Smoluchowski, Phys. Rev. **60**, 661 (1941).
- [14] K. Besocke, B. Krah-Urban and H. Wagner, Surf. Sci. **68**, 39 (1977).
- [15] G.E. Rhead, Surf. Sci. **68**, 20 (1977).

CHAPTER 7

Surface Steps – Atomic Model

Contents

7.1	Computational Aspects	87
7.2	The Work Function Φ	88
7.3	The Local Work Function Φ_{loc}	90
7.4	Applied Electric Fields at Flat Surfaces	96
7.5	Applied Electric Fields at Stepped Surfaces	100
7.6	Conclusions	103
	Bibliography	107

In the previous chapter the surface electronic structure of a stepped jellium surface was calculated. The present chapter deals with a more realistic model of stepped surfaces using the embedding technique, described in detail in Chapter 2. Using this highly accurate method, the work function and the change in the local effective potential and exchange-correlation potential at steps on well-defined Pd and Pt surfaces are studied. Subsequently the stepped surfaces are considered in the presence of applied electric fields in order to study the effect of steps on the screening charge at the surface.

7.1 Computational Aspects

In this work, the electronic structure of stepped surfaces of Pd and Pt is calculated, involving different combinations of (001) and (111) steps and terraces. In particular, the (311) vicinal surface is calculated. This is in fact the highest Miller index surface which can be studied with our present computer resources, with consideration to accuracy and CPU time. This is because high Miller index surfaces have large surface unit cells, and a much reduced interlayer spacing, both of which lead to larger calculations. Moreover, the plane along which the embedding potential is calculated intersects many more atoms, and this gives a richer structure to the embedding potential. Consequently, a larger plane wave basis is needed to represent the embedding potential accurately. Therefore, vicinal surfaces with lower step density than (311) are modelled by low index surfaces on which we put one-dimensional islands (hetero-islands). This was discussed extensively in Chapter 3.2, and is illustrated in Fig. 3.6. These structures involve a surface unit cell 6 times larger than the low Miller index counterparts of (001) or (111), and hence are termed $6\times(001)$ and $6\times(111)$, respectively. The bulk lattice parameters of Pd (7.35 a.u.) and Pt (7.41 a.u.), taken from experiment [1], are used throughout this thesis.

In this calculation, we treat explicitly a region extending approximately 12 a.u. beyond the outermost surface plane of atoms, into the vacuum. At this point, it is embedded onto the flat vacuum potential using the embedding potential of equation (2.74). The self-consistent potential in the surface region enables us to study the surface potential variation and the work function, within the LDA exchange-correlation approximation. An external electric field can also be applied by putting a plane of charge σ at the vacuum embedding plane, which gives an electric field perpendicular to the surface of $F = -4\pi\sigma$ (our convention is that positive charge at the vacuum embedding plane gives negative F). The embedding method is ideally suited for treating the screening of external electric fields: the surface is joined onto the semi-infinite substrate, with the Fermi energy of the bulk determining the charge density, and the number of electrons at the surface has the freedom to vary to reach perfect screening.

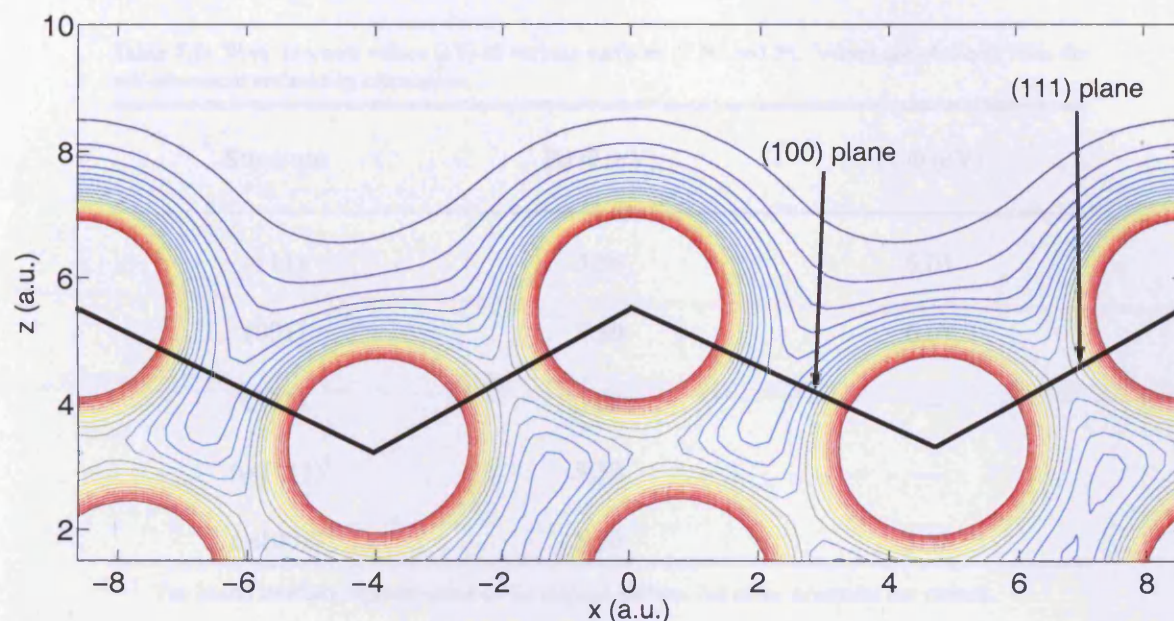


Figure 7.1: Linear-averaged valence electron density of a three layer Pd(311) vicinal surface. The (001) and (111) planes are shown on the map. Contour spacings are 5×10^{-3} a.u. with a charge cut-off on the atoms of 0.1 a.u.

7.2 The Work Function Φ

One of the most obvious effects of steps on surface properties is a change in the work function as we saw in Chapter 6 for the jellium surface. Figure 7.1 gives the results for the charge density at the Pd(311) surface, showing how the charge contours flatten out in comparison with the local surface plane of atoms. This smoothing has the effect of reducing the work function Φ compared with the (001) and (111) facets of which the (311) surface is comprised. The values for the work functions of these three surfaces are given in Table 7.1, and show that the work function reduction is significant. Separate pseudopotential calculations on different surfaces of W have shown similar results [2]. Table 7.1 also presents work functions for the $6 \times (111)$ and $6 \times (001)$ hetero-island stepped surfaces, and similarly for Pt. Again the trend of decreasing work function with the introduction of steps is apparent. We saw in Chapter 6 that the work function was no longer linear with step density for the Al(2,1) stepped surface, and a similar relationship is shown here for Pd(311). Although the $6 \times (111)$ and $6 \times (001)$ stepped surfaces of Pd have a lower step density than the Pd(311) surface, they show a larger reduction in work function. This is presumably because the facets of Pd(311) are too narrow for Smoluchowski smoothing to have its full effect. For the Pt structures, although a decrease in the work function is seen for the $6 \times (001)$ stepped surface, the reduction is rather small (0.14 eV below the (001) surface). However, this reduction is in reasonably good agreement with the results of Besocke *et al.* [3], who obtain a 0.2 eV reduction for similar Pt surfaces.

Table 7.1: Work function values (eV) of various surfaces of Pd and Pt. Values are obtained from the self-consistent embedding calculation.

Structure	Pd Φ (eV)	Pt Φ (eV)
(111)	5.86	6.01
(001)	5.80	6.07
(311)	5.64	—
$6\times(111)^\dagger$	5.53	—
$6\times(001)^\dagger$	5.50	5.93

[†] The island structure representation of the stepped surface. All other structures are vicinal.

The results of Table 7.1 give, as expected, a slightly greater work function for the close-packed Pd(111) than the more open Pd(001) surface. However, literature results for these work function values are contradictory. Inverse-photoemission experiments give Φ for Pd(001) as 5.80 eV [4] and separate two-photon photoemission experiments give the work function as 5.55 eV [5] and 5.44 eV [6] for Pd(111). However, the embedding results for the work functions are similar to the values obtained by Heinrichsmeier *et al.* [7] in a slab calculation using a local density approximation for the exchange-correlation potential V_{xc} . These workers obtained 5.75 eV and 5.68 eV, for Pd(111) and Pd(001) respectively, with the difference in the work function being very close to the difference found in Table 7.1. Heinrichsmeier *et al.* also calculated the Pd(001) and Pd(111) work function values using a non-local exchange-correlation potential. Although the values obtained using non-local exchange-correlation were considerably higher (by about 0.4 eV) than those found for the local exchange-correlation potential, the difference in the work function still remains as 0.07 eV.

The work function values of Pt however, are a little surprising. It is evident that the more open Pt(001) work function is slightly higher than that found for the Pt(111) surface, contradicting that measured experimentally: Wandelt *et al.* find $\Phi = 5.85$ eV for Pt(001) [8, 9] (though this decreases to 5.75 eV for the more stable *hex*-rot surface) using a Kelvin probe [10]; Lehmann *et al.* obtain Φ for Pt(111) = 5.97 eV [11] (remarkably close to the value obtained via embedding) using a photoemission technique. However, caution should be used when comparing with the experimentally obtained value for Pt(001), since the structure of Wandelt *et al.* [8, 9] involves hydrogen adsorption. It may also be the case that local phases of the *hex*-rot structure were present in this investigation; clean Pt(001) reconstructs readily to the *hex*-rot

Table 7.2: Work functions values (eV) of (111) and (001) faces of Pd for different numbers of layers within the surface region.

Pd surface structure	1 layer	2 layer	3 layer
(111)	5.76	5.86	5.86
(001)	5.72	5.80	5.82

structure. However, the Pt(001) surface can be prepared from H adsorption of *hex*-rot Pt(001), as used by Wandelt *et al.* in his investigations, but this exhibits a low degree of perfection [8, 9]. For elucidation, the *hex*-rot reconstruction of Pt(001) involves a re-organisation of the surface layer of Pt atoms, forming a hexagonal structure. The driving force for this reconstruction is mainly considered to be due to the increased coordination of the surface atoms.

The values for the work function given in Table 7.1 for the close-packed surfaces are converged with respect to the number of layers treated self-consistently in the surface region. This is apparent from Table 7.2, which shows the values of Φ for Pd(001) and Pd(111) for different numbers of layers. From this table we see that convergence is essentially achieved in a two-layer calculation. Even the one-layer calculation is accurate to about 0.1 eV, with differences given very accurately. This property of the rapidly converging Φ is due to the high screening ability of metals. The perturbation of the potential due to the surface is quickly screened by the high electron density, and within two or three layers the potential becomes bulk-like. In the case of the hetero-island structures, the layer number in the surface region is limited by computational considerations, and as such the structures comprise a single layer calculation with a hetero-island adlayer. This means that for part of the surface the effective number of layers is limited to one. From the work function convergence shown in Table 7.2 it is therefore expected that a maximum error of 0.1 eV would occur in the effective potential above the one-layer region of the surface, and an error of at most 0.1 eV in the work functions given in Table 7.1 for the adatom structures.

7.3 The Local Work Function Φ_{loc}

The work function values discussed so far are defined as the energy required to remove an electron from the Fermi energy of the metal to just outside the surface. The term “just outside” refers to where the effective potential becomes flat. In practice, we take this value from the Hartree potential at the vacuum embedding plane. However, for many purposes it is useful to define a local work function Φ_{loc} at some point \mathbf{r} fairly close to the surface, as

$$\Phi_{loc}(\mathbf{r}) = V_{eff}(\mathbf{r}) - E_F. \quad (7.1)$$

$V_{eff}(\mathbf{r})$ is the effective potential. This local work function varies over the surface, depending on the local coverage of adsorbates, or proximity to defects like surface steps – the topic of this section. Φ_{loc} can be probed experimentally using photoemission of adsorbed Xe (PAX) [12, 13], two-photon photoemission spectroscopy [14], or with the scanning tunnelling microscope (STM) [15]. PAX and STM measurements have shown that Φ_{loc} is reduced at monatomic step sites by as much as 1.9 eV on Cu(111) [15], 1.3 eV on Ru(001) [16], and 0.9 eV on Au(111) [15], presumably due to the Smoluchowski electron smoothing effect. This can have important consequences for surface reactivity: the local potential barrier to electron removal from the substrate is reduced at this site, promoting reactivity [17]. In this section, we describe our calculation of the variation of $\Phi_{loc}(\mathbf{r})$ over the surfaces of monatomically stepped Pd surfaces. The effective potential $V_{eff}(\mathbf{r})$ used in (7.1) is found from the solution of the Poisson equation using the self-consistent charge density over the whole space of the surface unit cell, including the top few layers of the substrate and extending approximately 12 a.u. into the vacuum, as described in section 7.1. For the most part, the remainder of this chapter deals with Pd stepped surfaces, owing to the closely similar trends between Pd and Pt.

To investigate the local work function an average of $V_{eff}(\mathbf{r})$ is taken along a line parallel to the step face to give a function of x , the coordinate parallel to the surface, and z , the perpendicular coordinate:

$$V_{eff}(x, z) = \frac{1}{a_y} \int_{a_y} V_{eff}(x, y, z) dy \quad (7.2)$$

where a_y is the side of the surface unit cell in the y -direction. Figure 7.2 shows the effective potential at our hetero-island structures, mimicking 3(001) \times (111), 3(111) \times (001), and 3(111) \times (111) stepped Pd surfaces (using microfacet notation [18]), in both step density and step geometry. The different curves show $V_{eff}(x, z)$ as a function of z for different values of x . It is noted that the z -origin for each curve corresponds to the local surface atomic plane, as indicated in the figure. In each of these plots (Fig. 7.2a–c) at least one curve clearly shows a reduced local effective potential within the range $z = 3$ –12 a.u. above the local plane of surface atoms. This local reduction in the effective potential is found on the lower terrace, in close proximity to the step and is presumably a result of the Smoluchowski smoothing of the charge density.

There are two possible contributions to this reduction in the local work function in the region surrounding the step base. The first is best explained using a jellium model: the smoothing effect of the electron density causes a charge dipole at the step site, with the appearance of a more positive charge at the top of the step, and a more negative charge close to the step base. This step dipole has a surface normal component opposite in direction to the usual charge spreading at the metal surface caused by the spill-over of the electron cloud into the vacuum [19], and as a result will reduce the effective potential at the step site. The second contribution to the reduced local work function is due to an increase in the

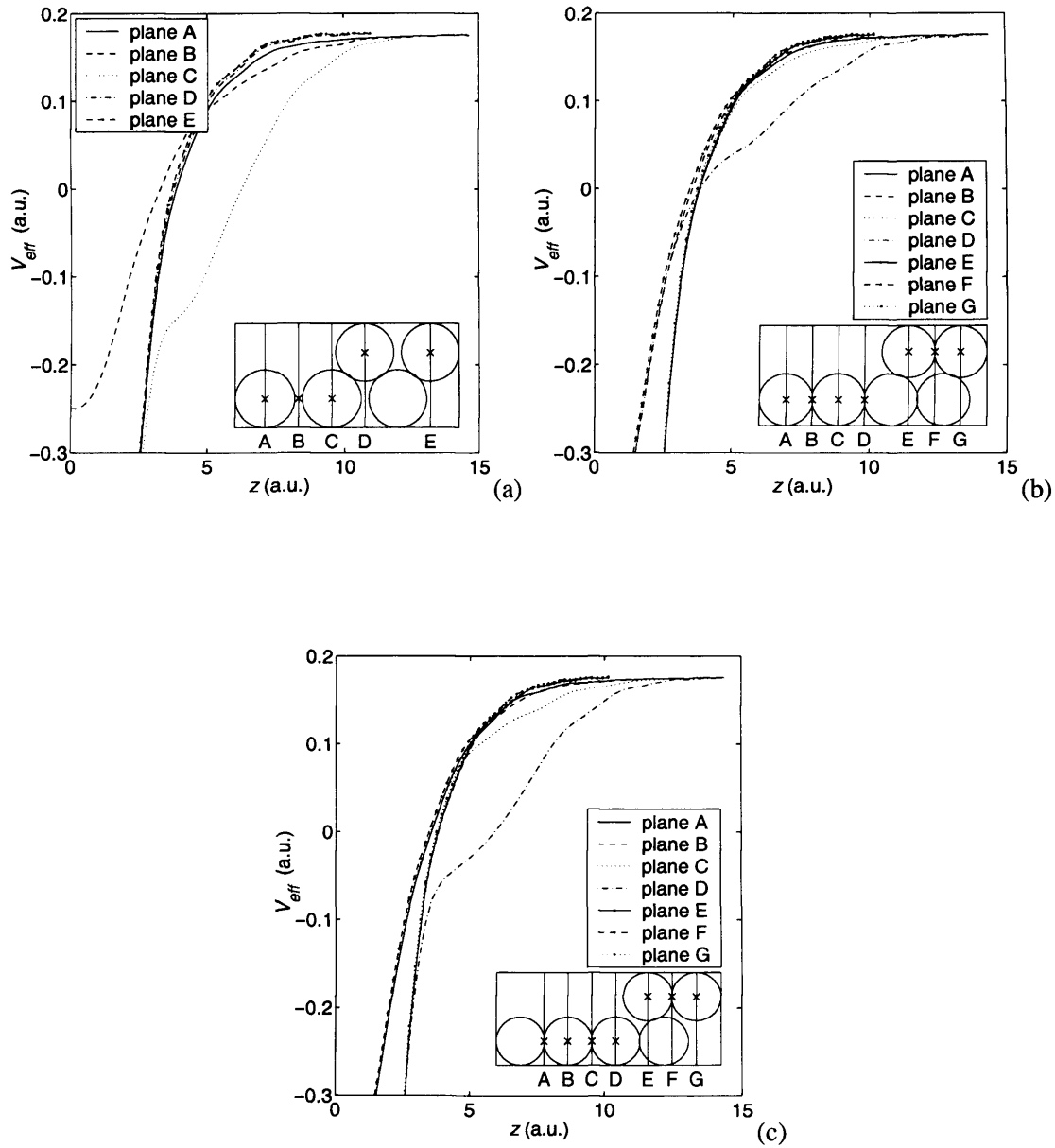


Figure 7.2: Total potential $V_{eff}(x, z)$ surrounding the hetero-island equivalent (a) 3(001) \times (111), (b) 3(111) \times (111), and (c) 3(111) \times (001) stepped surfaces. The z -direction is normal to the terrace plane for each surface and zeroed on the local surface plane (indicated by the \times , inset). The effective potential $V_{eff}(\mathbf{r})$ is measured relative to E_F . Inset, vertical planes of the stepped surface perpendicular to the step, showing the projection of the muffin tins onto the plane. Letters A–G signify different planes over which $V_{eff}(x, z)$ is plotted.

exchange-correlation effects due to the increased electron density at the step base. The result is to reduce the effective potential at the step base.

To distinguish between the dipole and the exchange-correlation effects, the exchange-correlation potential $V_{xc}(x, z)$ is plotted in Fig. 7.3, in the same form as Fig. 7.2. Almost the same reduction in the potential is seen near the step base, indicating that the major cause of the reduction in the local work function is indeed the exchange-correlation effect. This is not to say that the dipole effects are unimportant, but rather that the change in the local work function, which is only defined within the immediate vicinity of the surface, is almost entirely dependent on the change in exchange-correlation potential. The dipole effects resulting from the charge smoothing are of course important in determining the reduction of the actual work function Φ for stepped surfaces – the exchange-correlation effect is local and gives no long-range contribution to the potential. These results go against the conventional wisdom concerning the local work function, in particular the dipole moment argument frequently used to interpret experimental results on stepped surfaces. However, they do not contradict the literature ([3, 20, 21, 22, 23] to name but a few) pertaining to the actual work function, which explains the reduction of the metal work function in terms of dipole moments associated with edge atoms.

The variation of the local work function parallel to the surface is given in Fig. 7.4, which shows how $\Phi_{loc}(x, z)$ changes along a path at a constant distance of 6 a.u. from the local surface plane of atoms. The surface parallel direction, perpendicular to the steps, is taken relative to the centre of the upper step atom and the local work function difference is relative to the central atom on the upper terrace of our stepped structures. The results clearly show the valley of the local work function which resides adjacent to the step on the lower terrace. This reduction in $\Phi_{loc}(x, z)$ is found for Pd to be typically 0.4 eV. Pt stepped surfaces give a similar reduction, with $\Delta\Phi_{loc} = -0.6$ eV at its deepest point for Pt6 \times (001).

The curves of Fig. 7.4 show that the effect of the step perturbation is limited to within one or two terrace unit cells from the step site, affecting the lower terrace atoms, and to a lesser extent the upper step atom. This is in contrast to scanning tunnelling microscopy results of Au–Au and Cu–Cu monatomic steps by Jia *et al.* [15], whose results suggest that the effect of the step perturbation extends by as much as 6.5 Å and 10 Å, respectively. Avouris *et al.* [24] found similar ranges for the perturbed region for step defects on Au(111) and Ag(111) using STM techniques. These are much larger than the results shown in Fig. 7.4, in which the valley has a width of about 2 a.u., or 1 Å. The reason for the discrepancy seems likely to be that in STM experiments, the electric field present between tip and surface is greatly perturbed by the step, as we shall see in section 7.5. However, PAX experiments [25] suggest a smaller range for the reduction in surface potential than is found in STM. These experiments show that the reduced local work function is limited to within one Xe atom diameter on the lower terrace, adjacent to the step atom

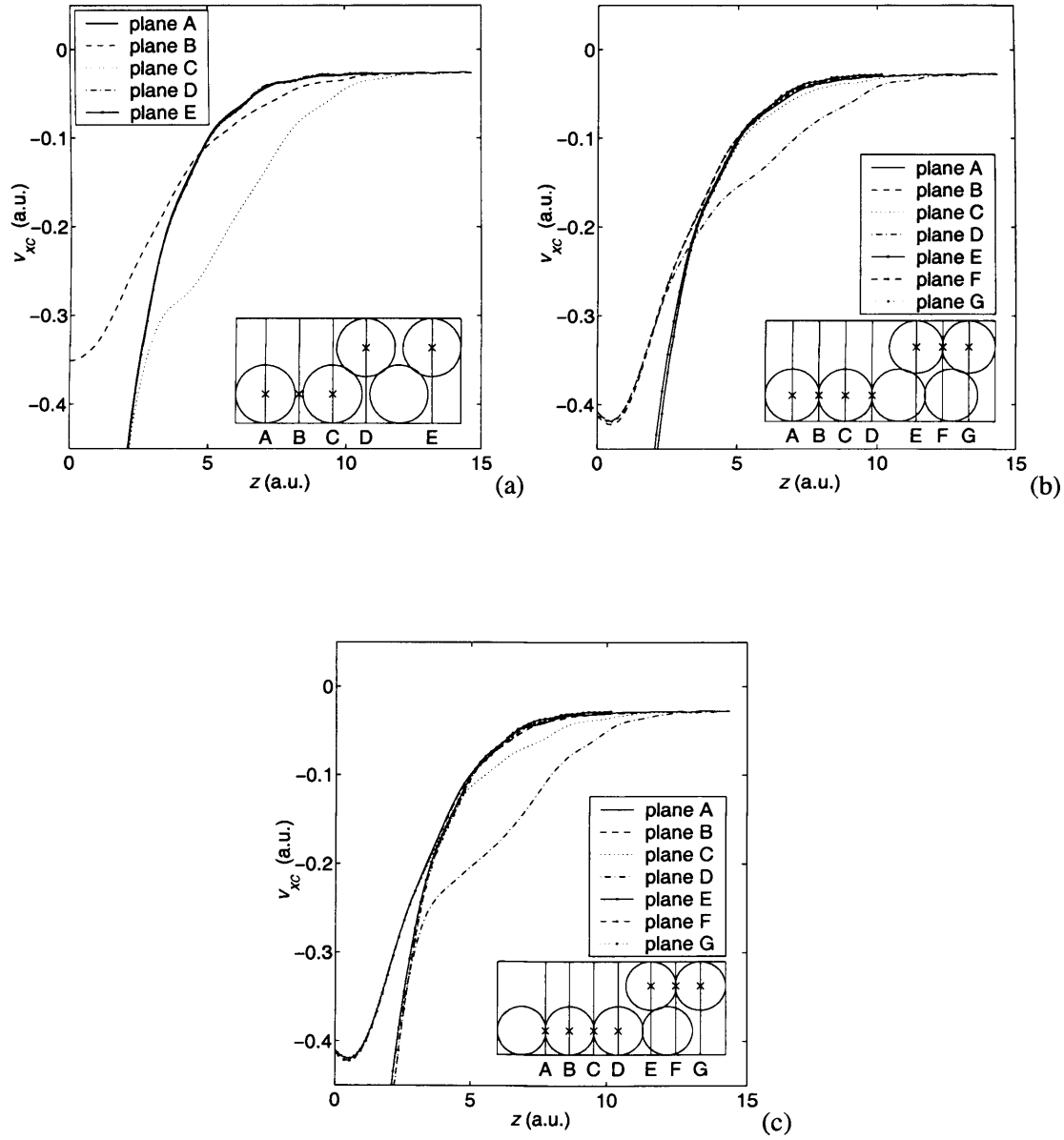


Figure 7.3: The same as in Fig. 7.2 but for the exchange-correlation potential $V_{xc}(x, z)$.

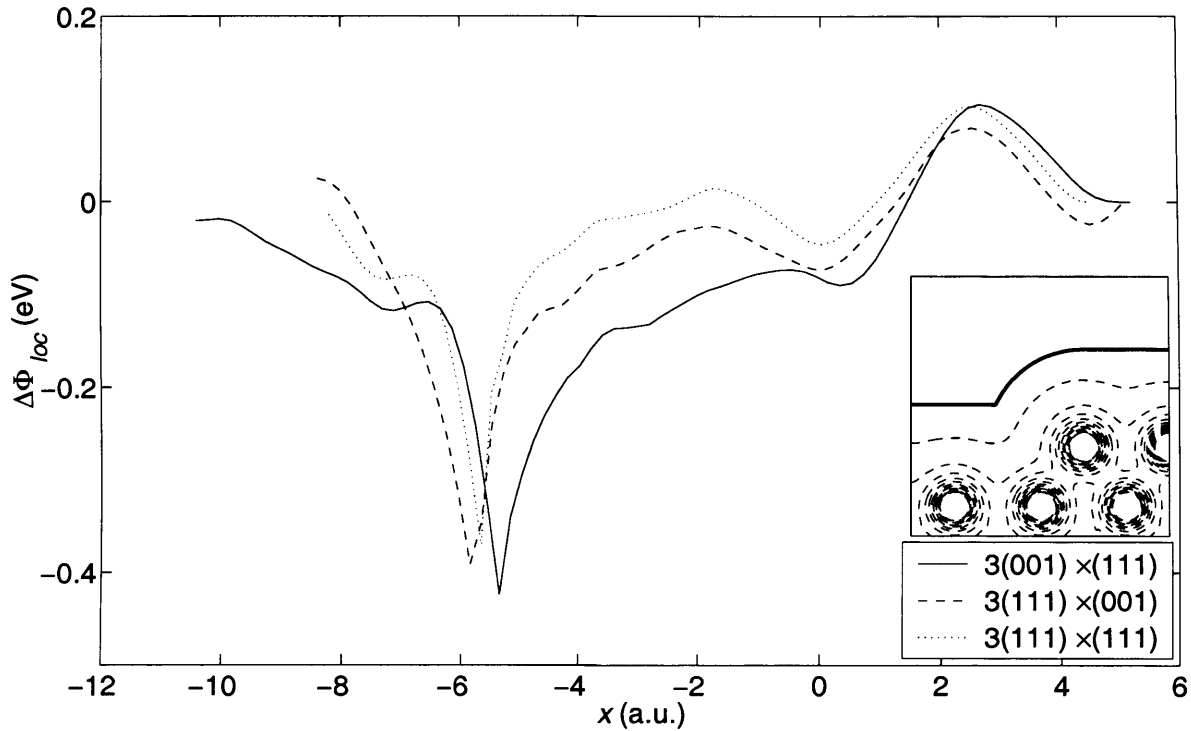


Figure 7.4: The change in the local work function along one-half surface unit cell of the hetero-island equivalent of Pd 3(001) × (111) (—), 3(111) × (001) (---) and 3(111) × (111) (...) stepped surfaces, relative to the upper central terrace atom. Values of $V_{eff}(x, z)$ are taken at 6 a.u. above the local plane of surface atoms. Inset, contour plot of the effective potential $V_{eff}(x, z)$ for the 6 × (001) stepped surface used as an example to indicate the line at which the potential is taken (—).

– a distance of the order of 4.5 Å [12].

We have stated that the reduction in $\Phi_{loc}(x, z)$ using the present embedding technique is 0.4 eV for Pd. However, this value depends upon the position of the probing line along the surface. So far, this probing line has been taken at a value of 6 a.u. above the local surface plane of atoms. This is similar in position to that which is probed experimentally using PAX. The Xe–metal interatomic spacing is typically 6 a.u. [12], with Xe–Ag having a spacing of 6.7 a.u. [26]. Our results show that all the stepped surface structures have a similar maximum depth of $\Delta\Phi_{loc} \approx 0.4$ eV, but the positioning of the line above the step, from which the $V_{eff}(x, z)$ values are taken at 6 a.u., is somewhat arbitrary. This will affect both the width and the depth of the local work function valley. At a distance of 5 a.u. from the local surface plane of atoms, a similar $\Delta\Phi_{loc}$ curve is found, but giving a Φ_{loc} reduction of about 0.6 eV for Pd, and 0.9 eV for Pt, at the deepest point of the curves. The results are in better agreement with the PAX experiments [27] than the 6 a.u. results, which give $\Delta\Phi_{loc}$ for Ru(001) as 0.9 eV [16].



7.4 Applied Electric Fields and Screening Effects at Flat Surfaces

We now turn our attention towards Pd surfaces in the presence of applied electric fields. This is relevant to the electrode surface in the electrochemical cell, in which the large field across the Helmholtz double layer is typically of the order of 1 V \AA^{-1} . As we described in Sec. 7.1, the field is induced by placing a charge σ [28, 29] at the vacuum embedding plane. The application of this external electric field results in a screening charge positioned just above the surface plane of atoms [30, 31, 32] equal in magnitude to the inducing charge σ but opposite in sign, ensuring that no field can penetrate the metal.

We shall first consider the screening charge density $\rho_{\text{scr}}^\sigma(\mathbf{r})$, the change in the 3-dimensional charge due to the externally applied electric field,

$$\rho_{\text{scr}}^\sigma(\mathbf{r}) = \rho^\sigma(\mathbf{r}) - \rho^0(\mathbf{r}). \quad (7.3)$$

$\rho_{\text{scr}}^\sigma(\mathbf{r})$ is then averaged over the y -direction (for stepped surfaces, this is parallel to the step face and surface) to obtain $\rho_{\text{scr}}^\sigma(x, z)$, in the same way that we average the potential in (7.2). Figures 7.5a and 7.5b show the screening charge density $\rho_{\text{scr}}^\sigma(x, z)$ averaged in this way on the Pd(111) and Pd(001) surfaces, with an electric field of 0.65 V \AA^{-1} , and we see clearly that the screening charge is positioned mostly on top of the surface atom. For the (111) surface this is brought out more clearly by plotting the screening density on a single y -plane centred on the surface atom (Fig. 7.6). The solid lines at about 2.7 a.u. above the surface atom planes (Fig. 7.5–7.6) are the centres of gravity of the screening charge:

$$z_{\text{scr}}^\sigma(x) = \frac{\int z \rho_{\text{scr}}^\sigma(x, z) dz}{\int \rho_{\text{scr}}^\sigma(x, z) dz}. \quad (7.4)$$

The image plane z_{im} is then given as

$$z_{\text{im}} = \frac{1}{a_x} \int_{a_x} z_{\text{scr}}^\sigma(x) dx. \quad (7.5)$$

where a_x is a distance spanning the surface unit cell in the x -direction. z_{im} is the distance from which the asymptotic image potential is measured [33] and is equivalent to the electrostatic surface. This image plane is field dependent and is the averaged surface normal centre of gravity of the change in the electron density when the external electric field is applied.

The image plane for a metal surface depends on the surface structure as well as the strength of the applied field F . The upper panel of Fig. 7.7 shows the variation of z_{im} as a function of applied external electric field for Pd(111) and Pd(001). The image plane is measured relative to the outermost surface plane of atoms for each face. We see that z_{im} lies further outside the metal for the (001) surface than for the (111) surface. A general trend is also seen for the image plane to move into the surface with an increasing positive applied field. The anomalous value in Fig. 7.7 for the image plane for the Pd(111)

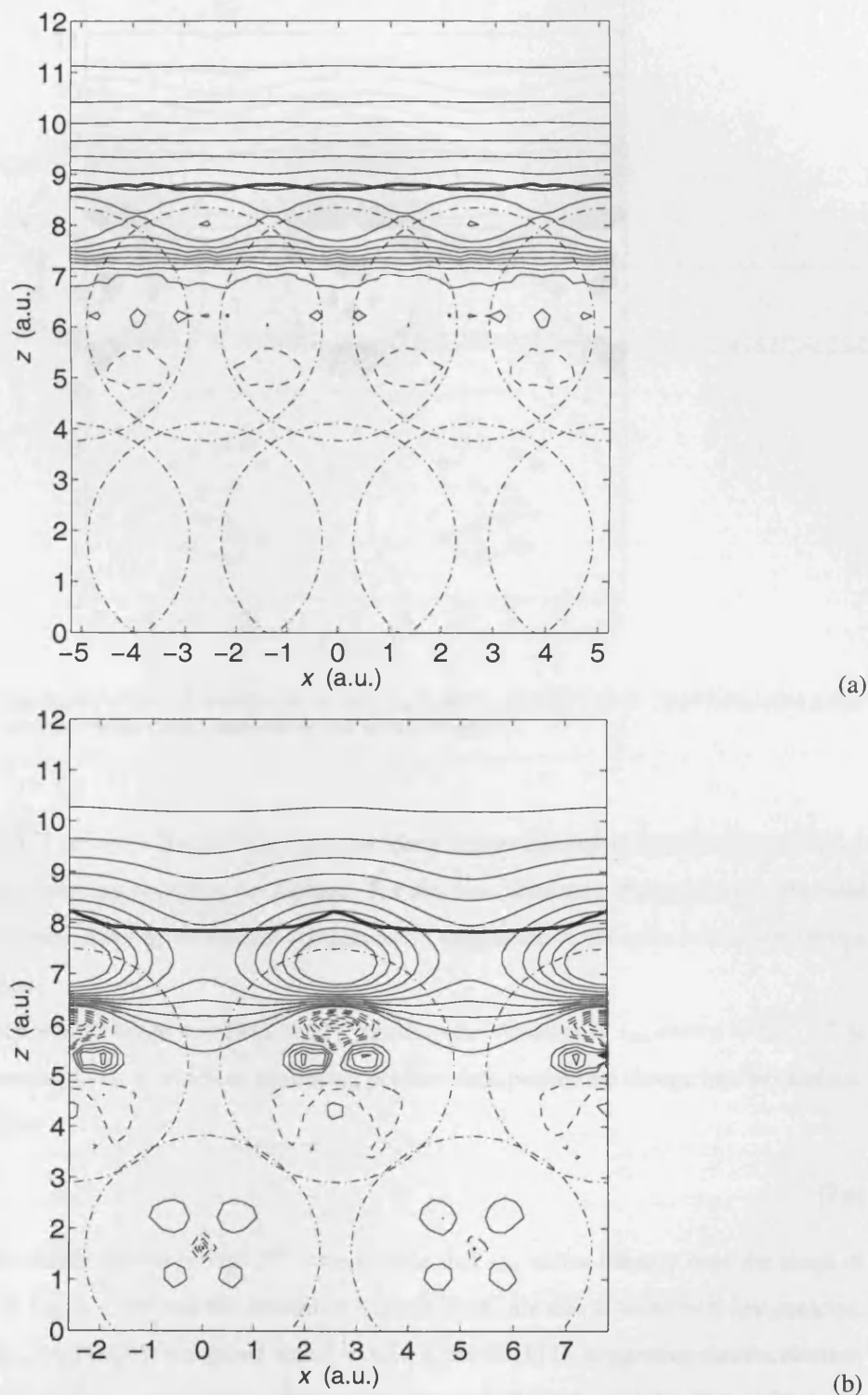


Figure 7.5: Screening charge density $\rho_{scr}^\sigma(x, z)$ of (a) Pd(111) and (b) Pd(001) surfaces in an externally applied positive electric field ($F = 0.65 \text{ V}\text{\AA}^{-1}$, $\sigma = -1 \times 10^{-3} \text{ a.u.}$). Solid contour lines represent positive screening charge, dashed contour lines represent negative screening charge. Contour spacings are $5 \times 10^{-5} \text{ a.u.}$ The dot-dashed circles represent the muffin tin boundaries mapped onto a plane. The origin in the surface normal direction is the bulk-side embedding plane.

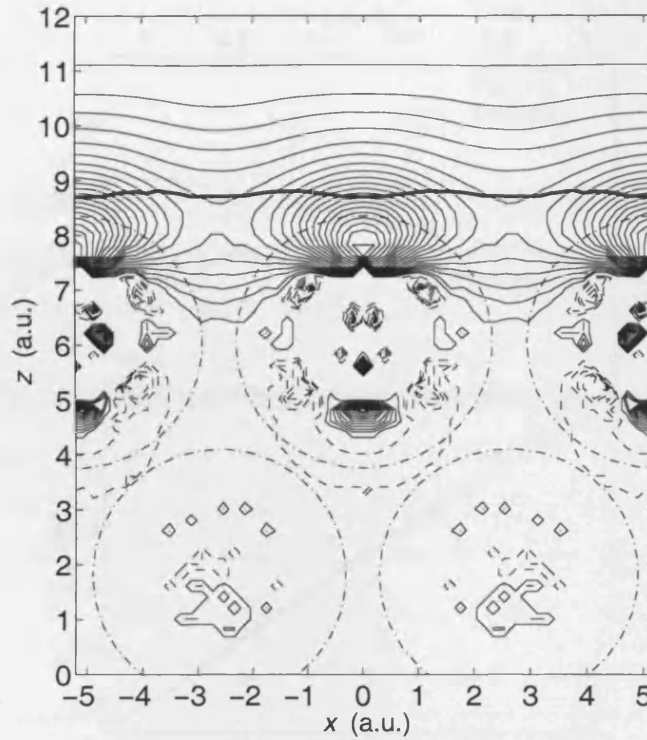


Figure 7.6: Screening charge density of Pd(111) produced by an inducing field $F = 0.65 \text{ V}\text{\AA}^{-1}$ ($\sigma = -1 \times 10^{-3} \text{ a.u.}$). For clarity, this plot shows $\rho_{\text{scr}}^{\sigma}(\mathbf{r})$ on a single y -plane, cutting the centres of the surface Pd atoms.

surface at $F = 0.065 \text{ \AA}^{-1}$ ($\sigma = -1.0 \times 10^{-4} \text{ a.u.}$) is most likely due to numerical inaccuracies resulting from the low value of screening charge at the surface. For this low screening charge density, the total charge in the surface region alters by an amount comparable in magnitude to the error in the total charge imbalance in this region.

The variation in screening charge with field, which results in the variation in z_{im} shown in Fig. 7.7, is due to non-linear screening [34], in which an increasing positive field pushes the charge into the surface. We calculate the gradient

$$\xi = \left| \frac{dz_{\text{im}}}{dF} \right|, \quad (7.6)$$

from a linear fit to the results shown in Fig. 7.7 – we assume that z_{im} varies linearly over the range of field strengths taken in Fig. 7.7 and that the deviations from linearity are due to numerical inaccuracies. We find that $\xi = 6.9 \text{ a.u.}$ for Pd(001) compared with $\xi = 3.3 \text{ a.u.}$ for Pd(111), suggesting that the electron density on the close-packed Pd(111) is “stiffer” than on the more open Pd(001) surface. We would expect the electrons to be stiffer on surfaces with a high work function, and as we have already seen, Pd(111) has a slightly higher work function than Pd(001). However, the difference in work function is only 0.06 eV , and this suggests that other electronic structure effects are at work, binding the electrons more tightly on

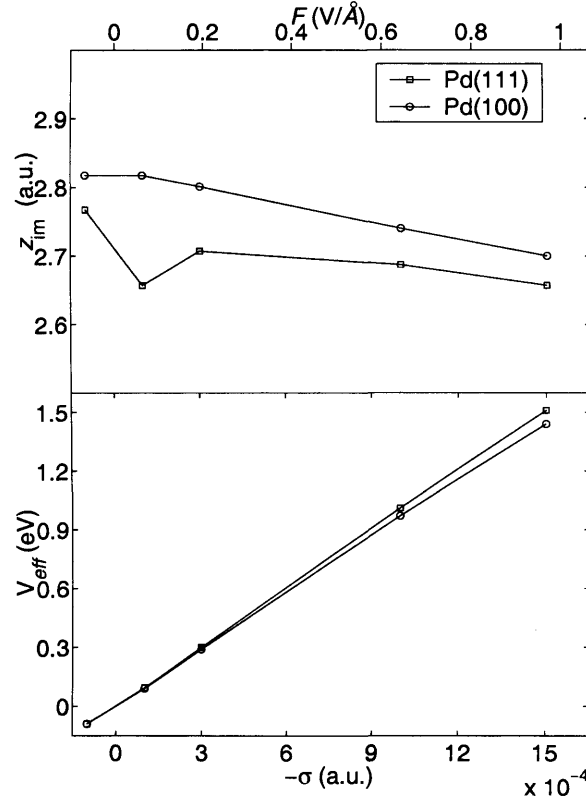


Figure 7.7: (Upper panel) Image plane position z_{im} as a function of the applied external electric field for Pd(111) and Pd(100). (Lower panel) Planar averaged effective potential at 5 a.u. from the outermost surface plane of atoms for Pd(111) and Pd(100) surfaces.

Pd(111). From the results of Aers and Inglesfield [35], ξ is found to be 8.8 a.u. for Ag(001), considerably larger than on Pd(001), and this does correlate with the work function variation: Φ for Ag(001) is 4.9 eV, compared with 5.8 eV for Pd(001). The stiffness is also connected with the value of z_{im} in the limit of zero field, where it is found that z_{im} follows the order for the different surfaces as: Ag(001), 2.9 a.u.; Pd(001), 2.83 a.u.; and Pd(111), 2.72 a.u., relative to the nuclear centres of the outermost surface plane.

The variation in z_{im} leads to changes in the capacitance of the surface, since z_{im} gives the electrostatic surface [33, 34] from which the distance between capacitance plates is measured. The concept of capacitance appears useful in electrochemistry [36, 37, 38]. We calculate the potential at a distance z above the surface, beyond the screening charge (here we take 5 a.u. above the surface plane of atoms), and with this we calculate the surface capacitance per unit area in the zero field limit:

$$C(z) = \left. \frac{d\sigma}{dV_{scr}(z)} \right|_{\sigma=0}. \quad (7.7)$$

σ is now the screening charge on the surface ($-1 \times$ the field-inducing external charge), and $V_{scr}(z)$ is the planar averaged effective potential resulting from the screening charge probed at a distance z above the plane of surface atoms. Integrating Poisson's equation twice we can obtain an expression for the

capacitance of the surface in the zero field limit, given as

$$C(z) = \frac{1}{4\pi} \{z - z_{im}(\sigma)\}^{-1}. \quad (7.8)$$

The effective potential outside the surface in the presence of an applied electric field can now be expressed in terms of the image plane [33] by combining (7.7) and (7.8). As z_{im} is a function of the field strength, in principle we should take the value for C in the limit of zero field, though in practice we make a linear fit to the results shown in the lower panel of Fig. 7.7. For Pd we obtain a capacitance of $(3.3 \pm 0.1) \times 10^{-2}$ a.u. ($5.6 \pm 0.2 \mu\text{F cm}^{-2}$) and $(3.60 \pm 0.03) \times 10^{-2}$ a.u. ($6.0 \pm 0.05 \mu\text{F cm}^{-2}$) for (111) and (001) respectively, using (7.7) and $z = 5$ a.u. This means that for a given applied voltage across parallel plates consisting of Pd(001) surfaces and Pd(111) surfaces, the *effective* surfaces, i.e. the image planes, are closer together for Pd(001) than for the (111) case. So for a given bias across the capacitor the more open (001) surface has a larger screening charge compared with the (111) surface. It seems then, that screening of an external field is more effective on the (001) surface.

Here we should point out that it is only for z close to the surface that the difference in capacitance between the (111) and (001) surfaces is apparent. However, this may be measurable in scanning probe measurements, and further studies of the variation of z_{im} with surface structure would be interesting.

7.5 Applied Electric Fields and Screening Effects at Stepped Surfaces

We now turn our attention to stepped surfaces in the presence of applied electric fields. Figures 7.8 and 7.9 show the screening charge density $\rho_{scr}^\sigma(x, z)$ for different Pd surfaces: (311) and the $3(001) \times (111)$ equivalent hetero-island structure, respectively. $\rho_{scr}^\sigma(x, z)$ is seen to accumulate primarily on top of the step atom in all cases. This is not surprising since, at the step edge, a more intense electric field is present due to edge effects [39].

Interestingly, the screening charge density of Fig. 7.9 shows a large difference in magnitude between the central positions of the lower and upper terraces. In Fig. 7.9, these positions lie on the extreme left and right of the contour map, respectively. This must be a feature of the hetero-island structure, as on a truly vicinal surface every terrace is equivalent. We suggest that our results accurately describe the electronic structure in the step region, although the fact that the screening density at the two different terrace sites (Fig. 7.9) differ so much suggests limitations of the hetero-island structure as an approximation to vicinal stepped surfaces in the presence of applied electric fields.

The electric field is greatly influenced by the steps, as we see from Figs. 7.10–7.11. These figures show the vector gradient of the averaged potential $V_{eff}(x, z)$ – the electric field ($\times -1$) averaged along the line perpendicular to the plot. Note that in all these figures the field is set equal to zero when the

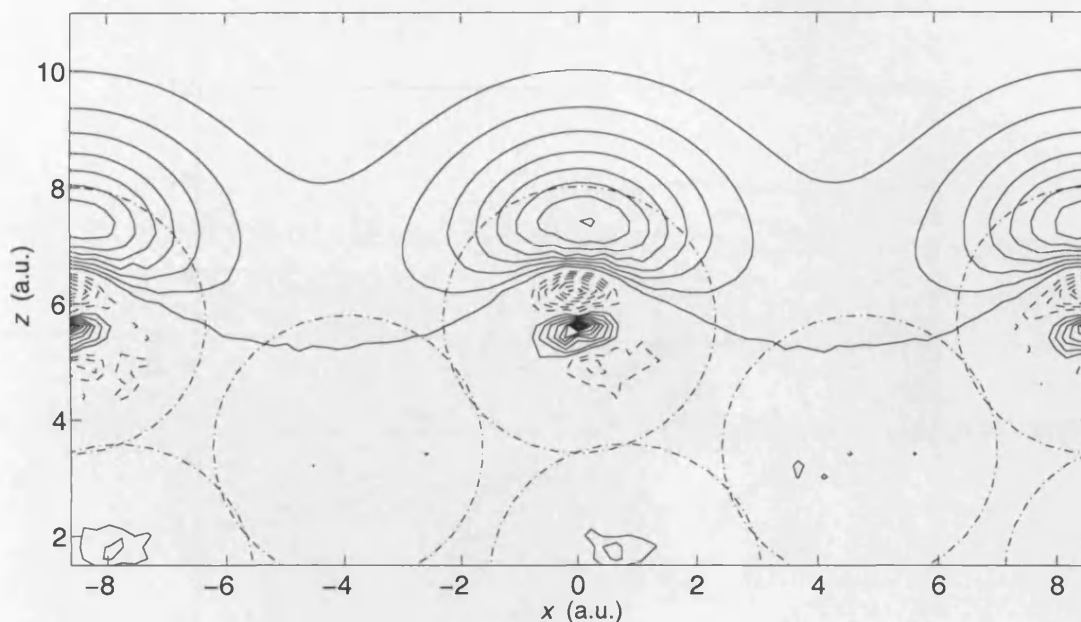


Figure 7.8: Linear-averaged screening density of the Pd(311) vicinal surface in an externally applied positive electric field ($F = 0.07 \text{ V}\text{\AA}^{-1}$). Solid contour lines represent positive screening charge, dashed contour lines represent negative screening charge. Contour spacings are $1 \times 10^{-5} \text{ a.u.}$ The dot-dashed circles represent the muffin tin boundaries mapped onto a plane. The origin in the surface normal direction is the embedding plane.

potential is below a certain limit. Figure 7.10 is the electric field for the hetero-island equivalent to the $3(001) \times (111)$ surface, with zero externally applied field, superimposed onto the surface charge density. Figures 7.11a and 7.11b are for the same surface as Fig. 7.10 but in an external field of $0.97 \text{ V}\text{\AA}^{-1}$. These show the change in the electric field at the surface due to the applied external field. The fields of both Fig. 7.11a and Fig. 7.11b are superimposed on to the corresponding screening charge. These figures show very clearly the way that screening is dominated by the edge atom, and it is at this atom where the electric field is largest. Similar effects of the screening charge build-up at prominences on the surface have been found by Lozovoi and Alavi [40].

We also see that an applied electric field influences the surface lateral field near to the step. With zero field (Fig. 7.10) there is already a significant component of the inherent electric field parallel to the surface. Wandelt *et al.* discussed this in connection with the increased surface reactivity of CO molecules on various transition metal stepped surfaces [25, 27, 41]: it was suggested that Stark splitting accounted for an increase in the occupation of an antibonding state, causing instability in the C–O bond. With an externally applied field, the increase in the surface-parallel field strength, shown in Fig. 7.11b, is not as large as the change in the surface-normal field, but nevertheless it is significant. This will have important consequences for chemisorption near steps in the electrochemical cell, and may affect atomic relaxation near steps. Moreover, the electric field between tip and surface in STM experiments will influence the

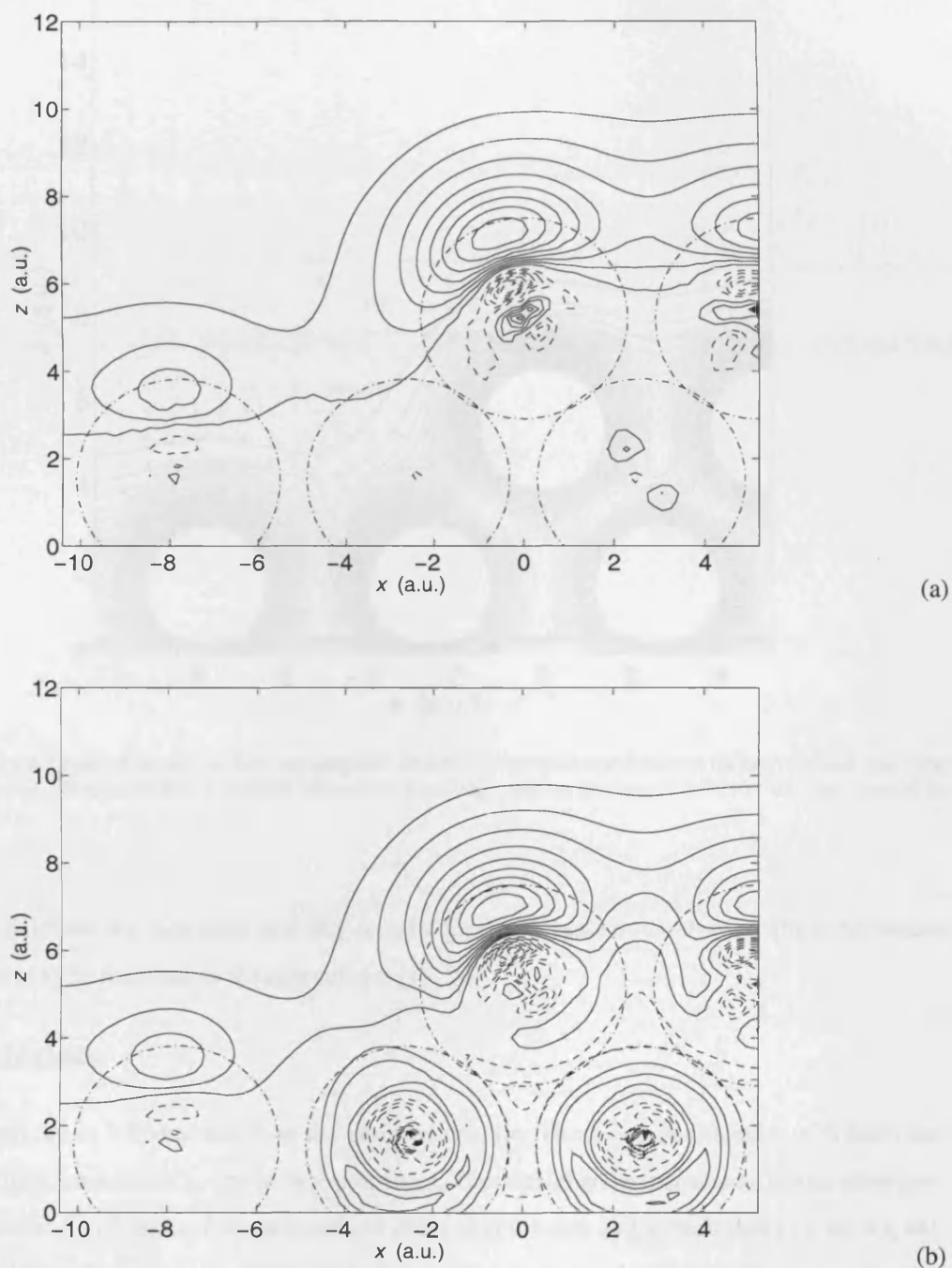


Figure 7.9: Linear-averaged screening density of a Pd hetero-island stepped surface (equivalent to the $3(001) \times (111)$ surface) in an externally applied positive electric field of (a) $F = 0.19 \text{ VÅ}^{-1}$ ($\sigma = -3 \times 10^{-4} \text{ a.u.}$), and (b) $F = 0.97 \text{ VÅ}^{-1}$ ($\sigma = -1.5 \times 10^{-3} \text{ a.u.}$). Solid contour lines represent positive screening charge, dashed contour lines represent negative screening charge. Contour spacings are (a) $3 \times 10^{-5} \text{ a.u.}$ and (b) $15 \times 10^{-5} \text{ a.u.}$. The dot-dashed circles represent the muffin tin boundaries mapped onto the plane. The origin in the surface normal direction is the embedding plane. The surface parallel origin is centred on the upper step atom.

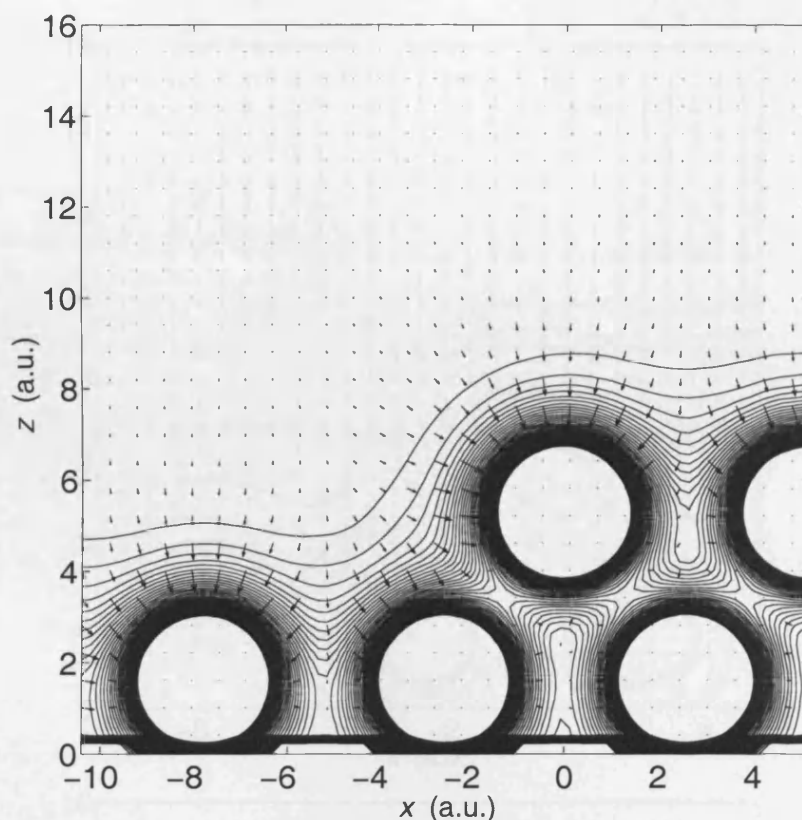
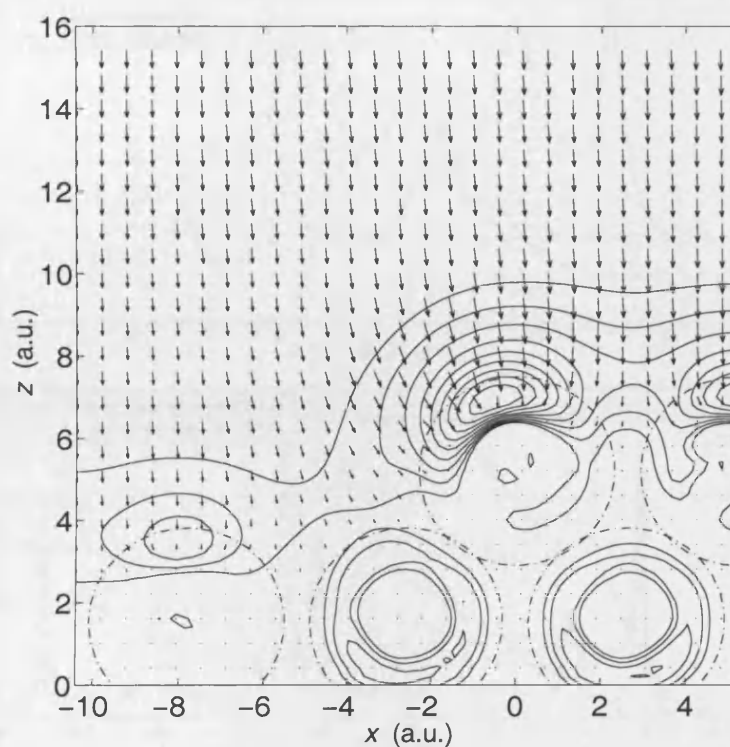


Figure 7.10: Vector field plot of the electric field superimposed onto the screening charge density at the hetero-island equivalent $3(001)\times(111)$ surface. No external field is applied. The charge density has contour spacings of 2.5×10^{-3} a.u. and a cut-off on the atoms of 0.1 a.u.

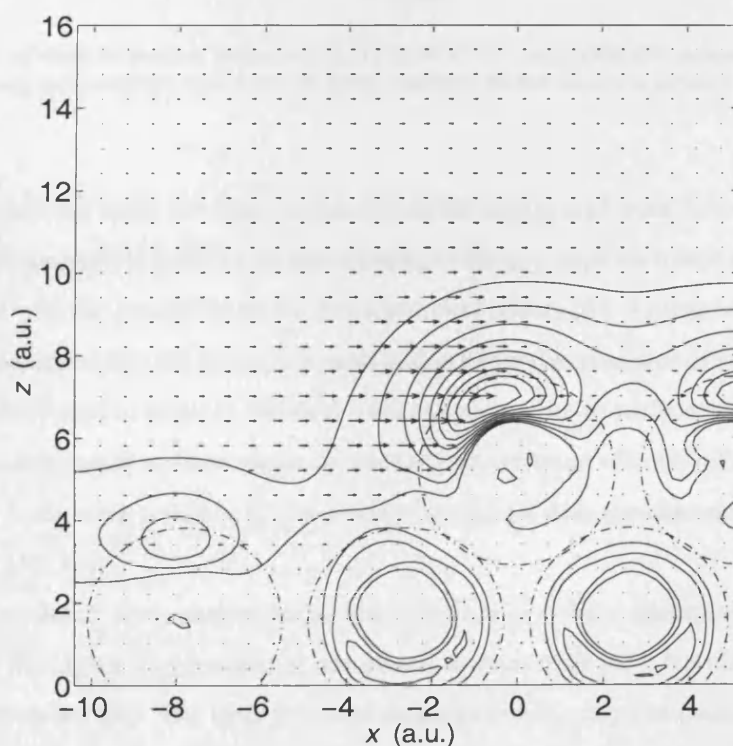
surface lateral field near the step edge, and may account for the increase in width over which the surface potential is found to be modified in the experiments [15, 24].

7.6 Conclusions

Steps on surfaces are an inherent defect on any surface in nature. These defects, together with kinks and vacancies, can have a marked effect on surface properties. Theoretical and experimental results show how the local attributes of well-defined stepped surfaces differ over the step and terrace sites [15, 42, 43, 44]. Recent electrochemical results have shown local variations in the induced screening charge and the site-specificity of adsorption. Furthermore, theoretical studies have shown how the charge smoothing due to the Smoluchowski effect [20] can give rise to a reduction in the work function at the step defect [21]. In fact, it is this charge redistribution at the step site, with a flow of electron density from the upper step edge to the step base, which is the main influence governing the differing properties between step and terrace. The dipole set up from this charge flow is opposite in direction to that of the normal surface potential, and consequently reduces the work function.



(a)



(b)

Figure 7.11: Vector field plot of the change in the electric field between the hetero-island equivalent $3(001) \times (111)$ surface due to an externally applied field. The field plot is superimposed on to the screening charge density for the same surface with the same external field as in Fig. 7.9. The external field strength is $F = 0.97 \text{ V \AA}^{-1}$ ($\sigma = -1.5 \times 10^{-3} \text{ a.u.}$). The dot-dashed circles are the projection of the muffin tins onto the vertical cut-plane. Plot (a) shows the full field difference, whereas plot (b) shows only the surface parallel component to the field difference, to a different scale.

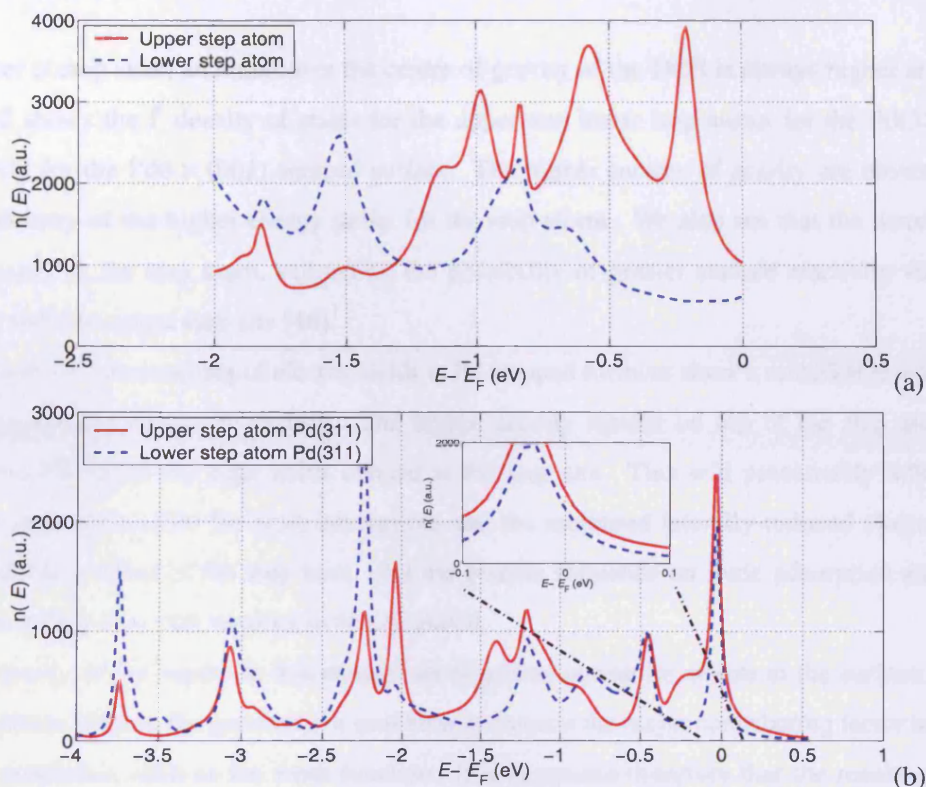


Figure 7.12: Density of states of separate surface atoms of (a) Pt6 x (001) and (b) Pd(311) stepped surfaces. The solid line represents the upper step atoms, and the dashed line the lower step atom, for the respective surfaces.

In our investigation, a study has been carried out on the variation of work function and the screening of electric fields on stepped Pd surfaces. In the presence of surface steps we found a work function reduction, in agreement with the prediction of the Smoluchowski effect [20]. As this involves the asymptotic potential at large distances into the vacuum, it must be due to the electrostatics of surface steps. However, a reduction was also found to occur in the local work function close to surface steps. The work demonstrated that this is dominated at short range by exchange-correlation effects, rather than electrostatics. This reduction in local work function is presumably connected with the changes in energy probed by PAX experiments [12, 13].

The presence of defect sites, such as steps, has relevance to surface adsorption and reactivity. This is not only due to the higher coordination of adsorbates at step edges [45], but also the reduction of the local potential, which we find. The local potential properties of the step can cause increased binding of surface adsorbates [14] and increased reactivity via Stark effects [27, 41], together with the reduction in the potential barrier for electron removal. Further analysis of the electronic structure of stepped surfaces suggests the possibility of increased reactivity via increased DOS at energies close to E_F . Comparing the density of states integrated over the muffin-tins along a particular surface, it is apparent that the DOS near

E_F is greater at step sites, and moreover the centre of gravity of the DOS is always higher at these sites. Figure 7.12 shows the $\bar{\Gamma}$ density of states for the upper and lower step atoms for the Pd(311) surface, and similarly for the Pd6 \times (001) stepped surface. The higher centres of gravity are obvious from the increased density of the higher energy peaks for the step atoms. We also see that the density of states at E_F is greater at the step atom, suggesting the possibility of greater surface reactivity via electronic interaction with the upper step site [46].

The results of the screening of electric fields at Pd stepped surfaces show a remarkable site specificity of screening density along the surface. The higher density resides on top of the step atom in order to screen the effects of the edge fields created at the step site. This will presumably influence field-adsorption sites, favourable for ionic adsorption, and the increased laterally-induced electric field will increase the Stark effect at the step base. But the precise influence on ionic adsorption and increased reactivity at defect sites still remains to be calculated.

The majority of the results in this chapter are based on geometric effects at the surface, rather than chemical effects. That is, the geometry of step defects remains the major contributing factor to the change in surface properties, such as the work function. It is suggested therefore that the results presented in this chapter would carry over to other transition metal surfaces. We should note, however, that both Pd and Pt have partially filled d -shells, whereas the d -shells in the noble metals like Ag and Au are completely filled, and are likely to be less polarisable [47]. This is apparent from the work of Besocke *et al.* [3], whose results show the differing dipole moments associated with monatomic steps on Au(111) and Pt(111) surfaces, -0.25 Debye and -0.6 Debye respectively.

Bibliography

- [1] D.R. Lide, Ed., *CRC Handbook of Chemistry and Physics 74th ed*; CRC Press, Boca Raton, FL (1993).
- [2] C.J. Fall, N. Binggeli and A. Baldereschi, *Phys. Rev. B*, **65**, 045401 (2001).
- [3] K. Besocke, B. Krahl-Urban and H. Wagner, *Surf. Sci.* **68**, 39 (1977).
- [4] S.C. Wu, D.M. Poirier, M.B. Jost and J.H. Weaver, *Phys. Rev. B* **45**, 8709 (1992).
- [5] G. D. Kubiak, *J. Vac. Sci. Technol. A* **5**, 731 (1987).
- [6] R. Fischer, S. Schuppler, N. Fischer, Th. Fauster and W. Steinmann, *Phys. Rev. Lett.* **70**, 654 (1993).
- [7] M. Heinrichsmeier, A. Fleszar, W. Hanke and A.G. Eguluz, *Phys. Rev. B* **57**, 14974 (1998).
- [8] B. Pennemann, K. Oster and K. Wandelt, *Surf. Sci.* **251/252**, 877 (1991).
- [9] B. Pennemann, K. Oster and K. Wandelt, *Surf. Sci.* **249**, 35 (1991).
- [10] D.P. Woodruff and T.A. Delchar, *Modern Techniques of Surface Science — Second Edition*, Cambridge Solid State Science Series, CUP, Sec. 7.5, p. 747 (1999).
- [11] J. Lehmann, P. Roos and E. Bertel, *Phys. Rev. B* **54**, R2347 (1996).
- [12] K. Wandelt in: P. Wissmann (Ed.), *Thin Metal Films and Gas Chemisorption*, Elsevier, Amsterdam, Sec. 2.8 and 3.2 of Chap. 7 (1987), and references therein.
- [13] K. Wandelt, J. Hulse and J. Küppers, *Surf. Sci.* **104**, 212 (1981).
- [14] K. Wandelt, *Appl. Surf. Sci.* **111**, 1 (1997).
- [15] J.F. Jia, K. Inoue, Y. Hasegawa, W.S. Yang and T. Sakurai, *Phys. Rev. B* **58**, 1193 (1998).
- [16] J. Küppers, K. Wandelt and G. Ertl, *Phys. Rev. Lett.* **43**, 928 (1979).
- [17] S. Daiser and K. Wandelt, *Surf. Sci. Lett.* **128**, L213 (1983).
- [18] M.A. Van Hove and G.A. Somorjai, *Surf. Sci.* **92**, 489 (1980).
- [19] N.D. Lang and W. Kohn, *Phys. Rev. B* **1**, 4555 (1970).
- [20] R. Smoluchowski, *Phys. Rev.* **60**, 661 (1941).

- [21] H. Ishida and A. Liebsch, Phys. Rev. B **46**, 7153 (1992).
- [22] G.E. Rhead, Surf. Sci. **68**, 20 (1977).
- [23] B. Krahl-Urban, E.A. Niekisch and H. Wagner, Surf. Sci. **64**, 52 (1977).
- [24] Ph. Avouris, I.-W. Lyo and P. Molinàs-Mata, Chem. Phys. Lett. **240**, 423 (1995).
- [25] K. Wandelt, Surf. Sci. **251/252**, 387 (1991).
- [26] J. Unguris, L.W. Bruch, E.R. Moog and M.B. Webb, Surf. Sci. **87**, 415 (1979).
- [27] K. Hermann, B. Gumhalter and K. Wandelt, Surf. Sci. **251/252**, 1128 (1991), and references therein.
- [28] We use the convention that a positive field induces a positive screening charge density, lying just above the surface plane of atoms. As an example a negative inducing charge $-|\sigma|$ induces a positive field normal to the surface.
- [29] 1 a.u. of electric field is equivalent to 51.376 VÅ^{-1} .
- [30] H. Ishida and A. Liebsch, Phys. Rev. B **66**, 155413 (2002).
- [31] C.L. Fu and K.M. Ho, Phys. Rev. Lett. **63**, 1617 (1989).
- [32] S. Clarke, M. Nekovee, P.K. de Boer and J.E. Inglesfield, J. Phys.: Condens. Matter **10**, 7777 (1998).
- [33] N.D. Lang and W. Kohn, Phys. Rev. B **7**, 3541 (1973).
- [34] A.K. Theophilou and A. Modinos, Phys. Rev. B **6**, 801 (1972).
- [35] G.C. Aers and J.E. Inglesfield, Surf. Sci. **217**, 367 (1989).
- [36] A.N. Frumkin, O.A. Petrii, and B.B. Damaskin in: J.O.M. Bockris, B.E. Conway, E. Yeager (Eds.), *Comprehensive Treatise of Electrochemistry*, vol. 1, Plenum Press, New York, Sec. 3.5 of Chap. 5 (1980).
- [37] X. Crispin, V.M. Geskin, C. Bureau, R. Lazzaroni, W. Schmickler and J.L. Brédas, J. of Chem. Phys. **115**, 10493 (2001).
- [38] G.A. Attard, O. Hazzazi, P.B. Wells, V. Climent, E. Herrero and J.M. Feliu, J. Electroanal. Chem. **568**, 329 (2004).
- [39] H.J. Kreuzer, L.C. Wang and N.D. Lang, Phys. Rev. B **45**, 12050 (1992).
- [40] A.Y. Lozovoi and A. Alavi, Phys. Rev. B **68**, 245416 (2003).
- [41] B. Gumhalter, K. Hermann and K. Wandelt, Vacuum **14**, 192 (1990).
- [42] H. Ibach and W. Schmickler, Phys. Rev. Lett. **91**, 016106 (2003).
- [43] V. Climent, R. Gómez and J.M. Feliu, Electrochim. Acta **45**, 629 (1999).
- [44] H. Ibach, M. Giesen and W. Schmickler, J. Electroanal. Chem. **544**, 13 (2003).
- [45] Jee-Ching Wang, Surf. Sci. **540**, 326 (2003).
- [46] P.J. Feibelman and D.R. Hamann, Phys. Rev. Lett. **52**, 61 (1983).
- [47] R. Stumpf and M. Scheffler, Phys. Rev. B **53**, 4958 (1996).

CHAPTER 8

Electron Field Emission From Pd and Pt Surfaces

Contents

8.1 Computational Aspects	111
8.2 Tunneling Current Density	114
Bibliography	120

Field emission from surfaces has recently received renewed attention, because of modern device applications. For instance, poly-atomic protrusions from surfaces, such as Spindt-type emitters and carbon nanotubes, are of particular interest because of their use in flat panel displays [1, 2] and vacuum microelectronic devices [3]. In all cases the current density of tunneling electrons is strongly dependent on the material, its work function, and the external field at the surface. Field emission is of course an old subject, and early evidence of surface states came from field emission experiments on W(001) [4]. The theory of field emission similarly has a long history: Fowler-Nordheim theory, based on a simplified surface potential leads to the famous Fowler-Nordheim plot of $\ln(J/F^2)$ against $1/F$, where J is the current and F is the applied field. This generally shows a straight line for a small range of F . There remain relatively few absolute calculations of J using first-principles methods [5], despite the continual experimental interest. This interest is mainly based on increasing emitter functionality, such as field-enhancement [6] at the surface via Spindt-type emitters or carbon nanotube modified surfaces – both of which involve high curvature tips to increase the effects of the external field at the surface [1, 2, 7, 8, 9]. Other work involves the reduction of the emitter work function via material coatings or annealing, in order to reduce the barrier to electron transport [10, 11, 12].

The emission of electrons from metallic surfaces occurs when an external negative field is applied to the surface. The negative field is opposite in direction to that considered in Chapter 7, and has the effect of reducing the potential above the surface and allows electron transmission through the surface barrier. The possibility of electron tunneling has an adverse affect on the convergence of the self-consistent calculation, and a limit has to be imposed on the maximum field strength. For large, negative fields ($\leq -1.5 \text{ V\AA}^{-1}$), the effective potential towards the vacuum embedding plane drops to a value below the metal Fermi level. This allows for a high level of electron penetration from the metal into the vacuum, beyond the vacuum embedding plane. As such, the electron count during self-consistency is highly oscillatory, and convergence is difficult. This imposes the limit of maximum negative field strength to $\approx -1.3 \text{ V\AA}^{-1}$ ($\sigma \approx 2 \times 10^{-3} \text{ a.u.}$ [13]). This limit is demonstrated graphically in Fig. 8.1.

This chapter uses a new and accurate method for calculating field emission from flat and stepped Pd and Pt surfaces. In the following section, some computational aspects are considered regarding the surface structure, moving on to the electron transmission results in Sec. 8.2 in which the role of work function changes in modifying emission are considered. The emphasis in this chapter is on the role of steps in modifying the electron transport through the metal / vacuum interface. It will be seen that the effects at stepped surfaces contain the essential ingredients needed to increase emitter functionality – work function reduction and increased field effects.

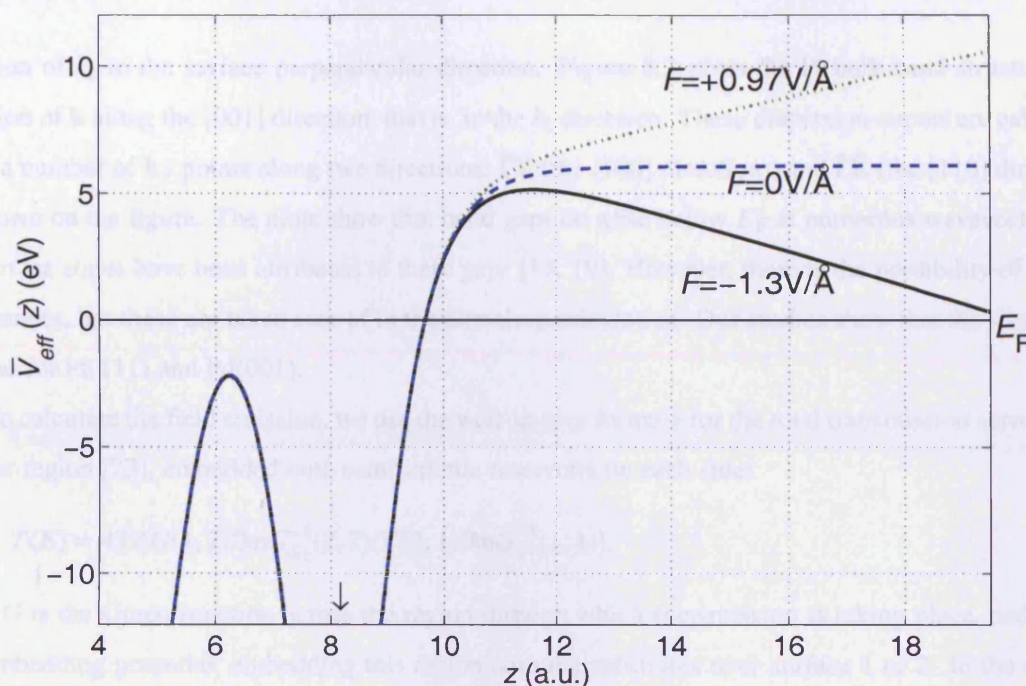


Figure 8.1: Planar averaged effective potential ($\bar{V}_{eff}(z)$) normal to the Pt(001) surface with three different applied external electric fields; $F = +0.97 \text{ V}\text{\AA}^{-1}$ (dotted), $F = 0 \text{ V}\text{\AA}^{-1}$ (dashed), $F = -1.3 \text{ V}\text{\AA}^{-1}$ (solid). The effective potential is taken relative to the Fermi level of the metal. The arrow indicates the position of the outermost surface atoms. The calculation involving the large negative field (solid line) is close to the field limit for which self-consistency can be reached. For any greater negative field, the calculation is likely to become unstable.

8.1 Computational Aspects

The calculations for field emission are again based on the embedding method [14], using codes developed by Ishida and his collaborators [15] with the tunneling formalism based on the Landauer-Büttiker equations [16]. The code first implements a self-consistent calculation of the electronic structure of the surface in a field, using full-potential linearised-augmented plane-waves (FLAPW). The tunneling current is found from a Green function expression, reformulated in the embedding scheme [5, 17]. The implementation only takes into account the current from extended bulk states, and the current from surface states is neglected. This is because lifetime effects are ignored, in which case the surface states are not in equilibrium with the semi-infinite electron gas; note that the current from surface resonances is included, so only states from band gaps are neglected. Fortunately, for the metal surfaces studied here, surface states are mainly confined to unoccupied energies [18, 19, 20, 21], and their role can be ignored. This is quite different from the (111) surfaces of the noble metals, where emission from the surface state which crosses the Fermi energy dominates [22].

To check the possibility of surface states, we consider, as an example, the Pt(001) surface. For a surface state to arise at a particular value of \mathbf{k}_{\parallel} , there must be a band gap in the band structure as a

function of k_z in the surface perpendicular direction. Figure 8.2 gives the Pt bulk band structure as a function of \mathbf{k} along the [001] direction, that is, in the k_z direction. These dispersion curves are calculated from a number of \mathbf{k}_{\parallel} points along two directions; $\bar{\Gamma}\bar{X}$ (the [100] direction), and $\bar{\Gamma}\bar{K}$ (the [110] direction), as shown on the figure. The plots show that band gaps do arise below E_F at numerous wavevectors, but no surface states have been attributed to these gaps [18, 19]. However, there is the possibility of surface resonances, but these are taken care of in the tunneling calculation. Our studies show that the situation is similar for Pt(111) and Pd(001).

To calculate the field emission, we use the well-known formula for the total transmission across some barrier region [23], embedded onto semi-infinite reservoirs on each side:

$$T(E) = 4\text{Tr}[G(1, 2)\Im G_{S_2}^{-1}(2, 2)G^*(2, 1)\Im G_{S_1}^{-1}(1, 1)]. \quad (8.1)$$

Here G is the Green function across the region through which transmission is taking place, and G_S^{-1} is the embedding potential, embedding this region onto the substrates over surface 1 or 2. In the original literature on transmission, G_S^{-1} is described as the self-energy, and Wortmann *et al.* [17] realised that this is the same as the embedding potential. To apply this to the field emission problem, surface 1 is the embedding plane used in the surface calculation, that is, a plane one or two layers below the surface, beyond which the potential is essentially bulk-like. Transmission is through the surface layers and the near-surface region with the applied field, to a plane in the asymptotic region of the field. At this plane the embedding potential is calculated from the Green function in the uniform field.

The vacuum embedding potential for tunneling calculations is conveniently calculated using Airy functions [24]. These are solutions of the Schrödinger equation in a triangular potential. The potential at the vacuum boundary has long reached the asymptotic limit, and the triangular potential at the surface is easily justified.

The tunneling current can be formulated in terms of the transmission, and Ohwaki *et al.* [5] have shown that the current density J is given by:

$$J = \frac{e}{\pi^3 \hbar} \int_{\text{SBZ}} d\mathbf{k}_{\parallel} \int_{-\infty}^{E_F} d\epsilon \quad (8.2)$$

$$\times \int_{S_1} dS_1 \int_{S_2} dS_2 G(1, 2)\Im G_{S_2}^{-1}(2, 2')G^*(2', 1')\Im G_{S_1}^{-1}(1', 1).$$

The first integral is of the surface parallel wavevector \mathbf{k}_{\parallel} over the surface Brillouin zone, denoted by SBZ; the second integral is over energies up to the Fermi energy, starting from some energy below the bottom of the band. The inner integrals are over the two embedding planes, in the metal and vacuum.

Using this transmission technique, Ohwaki *et al.* have calculated field emission for Cu and Au (001) and (111) surfaces [5]. In this chapter we describe electron emission calculations for flat Pd(001), Pt(001) and Pt(111) surfaces, as well as stepped surfaces of Pt and Pd involving (001) terrace and (111)

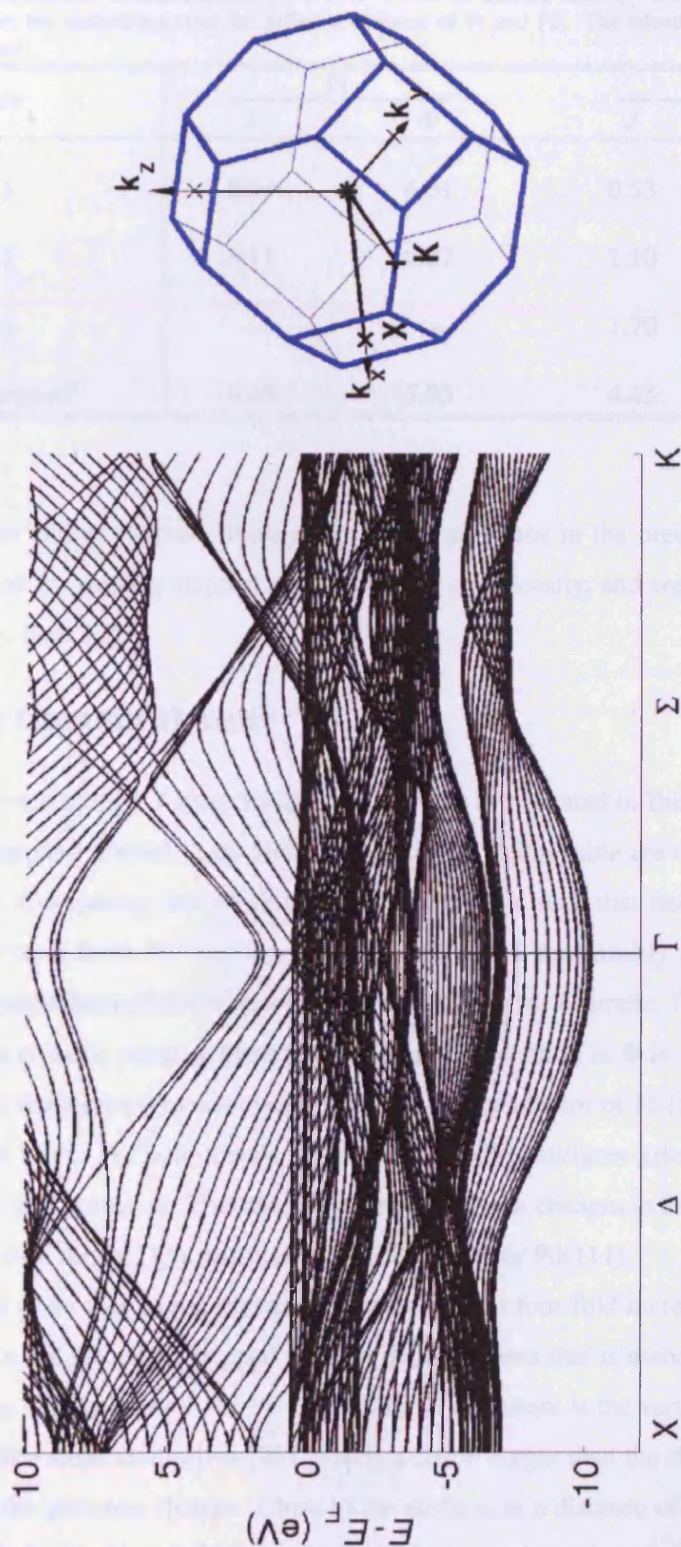


Figure 8.2: Pt bulk band structure along $[001]$ direction for $k_{||}$ -points along $\bar{\Gamma}\bar{X}$ and $\bar{\Gamma}\bar{K}$. Also shown is the 3-d Brillouin zone of a face-centred-cubic crystal, indicating appropriate points.

Table 8.1: Bulk state transmission current densities ($\times 10^8 \text{ A m}^{-2}$) with an applied field of -0.65 V \AA^{-1} , and work function values (eV) obtained from the embedding code for different surfaces of Pt and Pd. The island structure representation is indicated where appropriate[†].

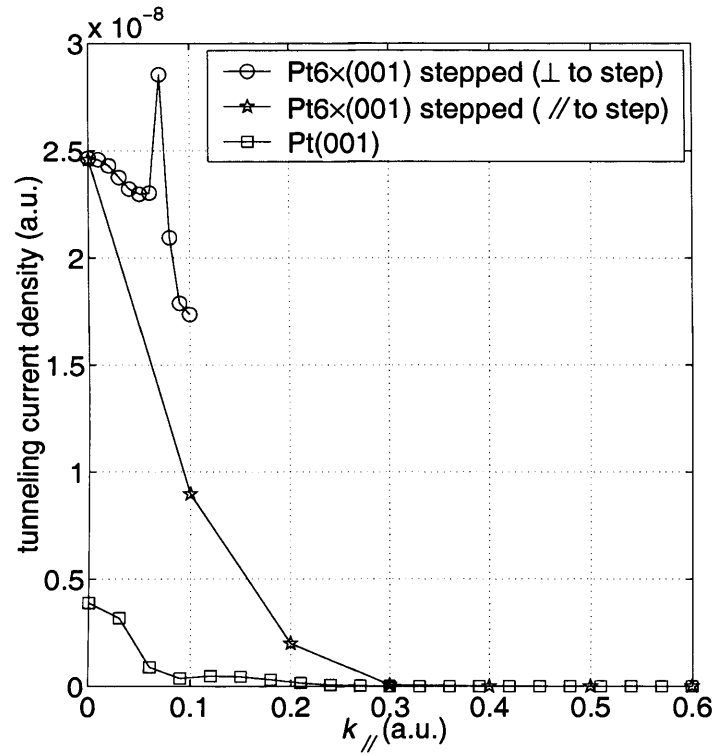
Surface	Pt		Pd	
	J	Φ	J	Φ
(111)	0.04	6.01	0.53	5.86
(001)	0.11	6.07	1.10	5.80
(311)	—	—	1.70	5.64
$6 \times (001)$ stepped [†]	0.49	5.93	4.45	5.50

step facets. As in the earlier chapters, there are practical problems in the present implementation of the embedding method for treating stepped surfaces of low step density, and we use the superstructure geometry described in Sec. 3.2.

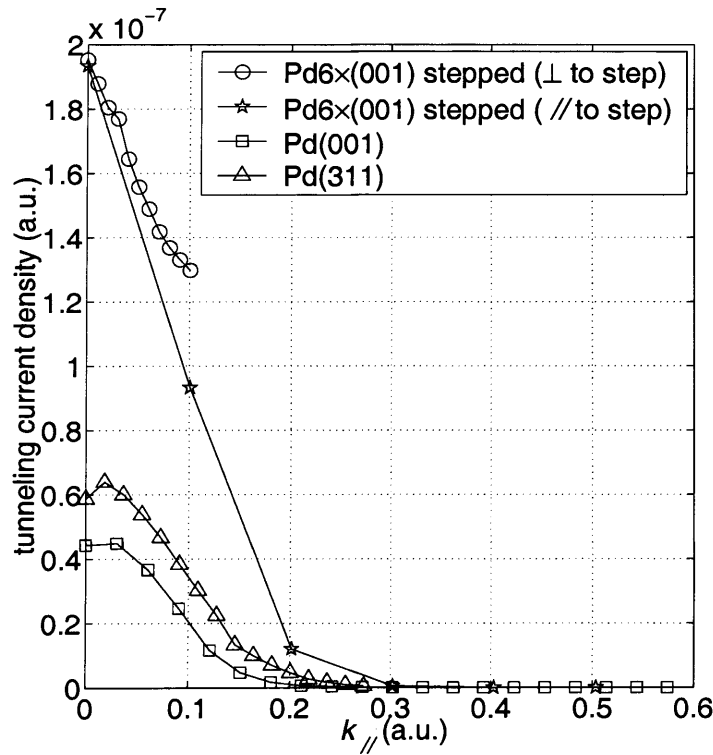
8.2 Tunneling Current Density

The field emission current density J from the different surfaces is presented in Table 8.1, with an external field of -0.65 V \AA^{-1} applied normal to the surface; also shown in this table are the calculated values of the work function Φ . Comparing first of all the flat surfaces, it is seen that field emission from Pd is a factor of 10 greater than from Pt. The work function difference presumably plays a role here, with the Pd(001) work function being 0.25 eV less than that of Pt(001) for example. However, there must be major material effects at work, because there is a much larger reduction in Φ in going from Au(001) to Cu(001), 0.66 eV, and the increase in calculated field emission is a factor of 15 [5], not so much greater than in going from Pd to Pt. For both metals, the more open (001) surfaces give greater field emission than the close-packed (111) surfaces. This cannot be associated with changes in the work function, which is greater for Pt(001) than for Pt(111), and less for Pd(001) than for Pd(111).

Surface steps lead to an increase in electron emission, with a four-fold increase for both Pd and Pt in going from (001) to the $6 \times (001)$ stepped surface. In both cases this is associated with a reduction in Φ , but the reduction is only 0.14 eV for Pt. Perhaps more important is the variation in the *local* work function near the surface steps themselves [25], which is much bigger than the change in Φ itself. This was demonstrated in the previous chapter. Close to the surface, at a distance of just 5–6 a.u. from the surface atomic layers, the local work function for Pd and Pt is reduced by as much as 0.9 eV close to the step site. Comparing this to the reduction in the actual work function of just 0.1–0.3 eV between the (001) and $6 \times (001)$ surfaces of Pt and Pd, then we see the possible significance of the local reduction in



(a)



(b)

Figure 8.3: Tunneling current density as a function of surface-parallel wavevector $k_{||}$ for (a) Pt(001) (\square) and stepped Pt6×(001) (parallel (\star) and perpendicular (\circ) to the step face) surfaces, and (b) Pd(001) (\square), Pd(311) (\triangle) and Pd6×(001) (parallel (\star) and perpendicular (\circ) to the step face). In each case the wavevector $k_{||}$ extends to the edge of the surface Brillouin zone. External field strength $F = -0.65 \text{ V \AA}^{-1}$.

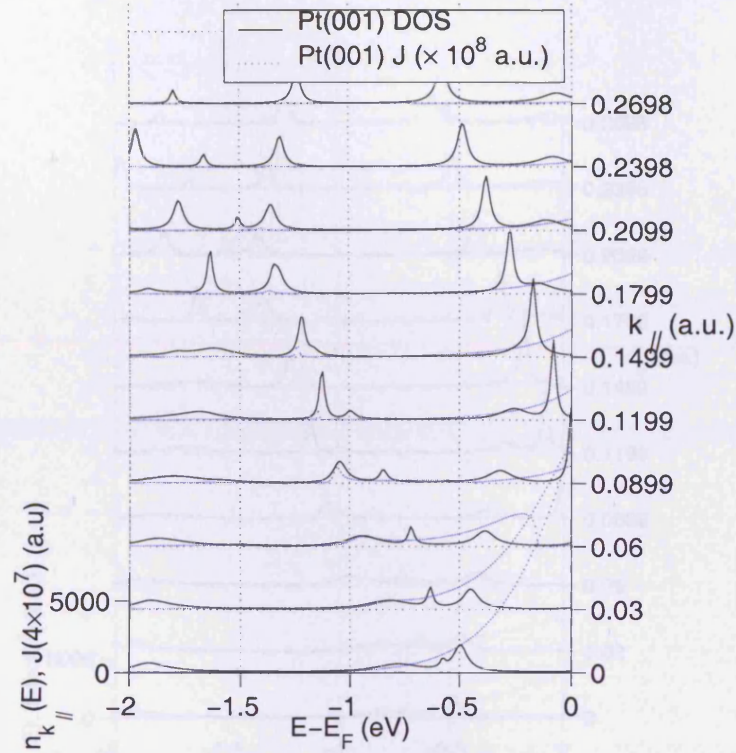


Figure 8.4: k_{\parallel} -resolved tunneling current density $J_{k_{\parallel}}(E)$ (dotted), and k_{\parallel} -resolved density of states $n_{k_{\parallel}}(E)$ (solid) for Pt(001) with external field strength $F = -0.65 \text{ V \AA}^{-1}$.

effective potential. This low potential path may provide a channel for electron emission from stepped surfaces.

The (311) surface consists of short (100) terraces, with (111) steps; even though there is a greater concentration of steps than on the $6 \times (001)$ surface, the reduction in work function is less, and there is a much smaller increase in electron emission. We speculate that both effects are due to the steps being so close together that the Smoluchowski charge smoothing [26] overlaps.

The wavevector-dependence of field emission shows interesting differences between the low-index and stepped surfaces. Figure 8.3 gives the surface tunneling current density as a function of k_{\parallel} , the surface-parallel component of the wavevector – in other words the integrand of the k_{\parallel} integral in (8.2). On the low-index surfaces, the current drops off very quickly with increasing k_{\parallel} , and as expected, the field emission originates mainly from the centre of the surface Brillouin zone. On Pd(311), the current is uniformly bigger than on Pd(001), but drops off similarly with increasing k_{\parallel} in the direction perpendicular to the steps. For Pd $6 \times (001)$, J is much bigger, and stays large over the whole range of k_{\parallel} in the narrow surface Brillouin zone in the direction perpendicular to the steps.

Pt $6 \times (001)$ is particularly striking, with a peak in current for k_{\parallel} away from the centre of the surface

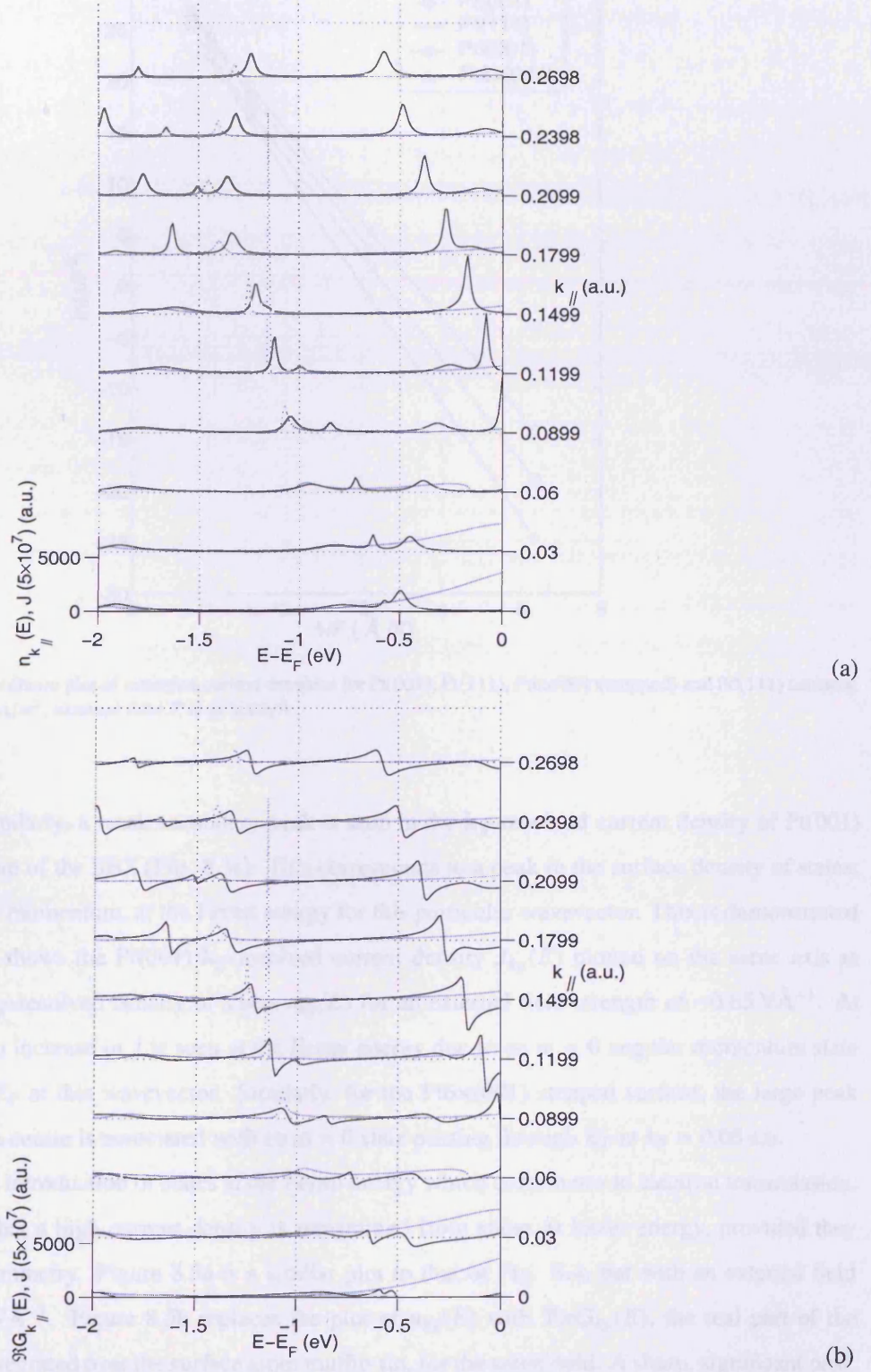


Figure 3.5: k_{\parallel} -resolved tunneling current density $J_{k_{\parallel}}(E)$ (dotted), and (a) k_{\parallel} -resolved density of states $n_{k_{\parallel}}(E)$ (solid), and (b) k_{\parallel} -resolved Green's function (real part only) $\Re G_{k_{\parallel}}(E)$ (solid) integrated through the surface muffin-tin of Pt(001). Applied external field strength $F = -0.97 \text{ V \AA}^{-1}$.

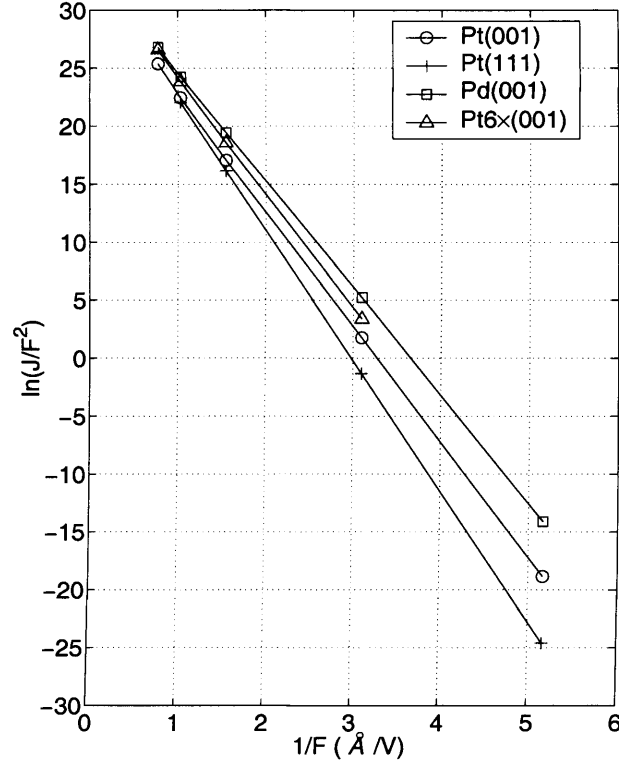


Figure 8.6: Fowler-Nordheim plot of emission current densities for Pt(001), Pt(111), Pt6x(001)(stepped) and Pd(111) surfaces. Current density J is in A/m^2 , external field F is in Volts/\AA

Brillouin zone. Similarly, a weak secondary peak is seen in the k_{\parallel} -resolved current density of Pt(001) away from the centre of the SBZ (Fig. 8.3a). This corresponds to a peak in the surface density of states, with $m = 0$ angular momentum, at the Fermi energy for this particular wavevector. This is demonstrated in Fig. 8.4 which shows the Pt(001) k_{\parallel} -resolved current density $J_{k_{\parallel}}(E)$ plotted on the same axis as the surface atom k_{\parallel} -resolved density of states $n_{k_{\parallel}}(E)$ for an external field strength of -0.65 V\AA^{-1} . At $k_{\parallel} = 0.1199 \text{ a.u.}$ an increase in J is seen at the Fermi energy due to an $m = 0$ angular momentum state dropping through E_F at this wavevector. Similarly, for the Pt6x(001) stepped surface, the large peak away from the zone centre is associated with an $m = 0$ state passing through E_F at $k_{\parallel} = 0.08 \text{ a.u.}$

It is not just the introduction of states at the Fermi energy which contributes to electron transmission. Figure 8.5 shows that a high current density is transmitted from states at lower energy, provided they have the correct symmetry. Figure 8.5a is a similar plot to that of Fig. 8.4, but with an external field strength of -0.97 V\AA^{-1} . Figure 8.5b replaces the plot of $n_{k_{\parallel}}(E)$ with $\Re G_{k_{\parallel}}(E)$, the real part of the Green's function integrated over the surface atom muffin-tin, for the same field. A sharp, significant peak appears in J at -1.2 eV below the Fermi energy for $k_{\parallel} = 0.1199 \text{ a.u.}$ This coincides with the introduction of an $m = 1$ state (Fig. 8.5a) – or more precisely, with the positive peak of $\Re G$ (Fig. 8.5b) for this state.

We now turn to the traditional Fowler-Nordheim plot. Figure 8.6 shows a plot of $\ln(J/F^2)$ against $(1/F)$ for field emission from our surfaces. This gives a clear demonstration of the linearity of such a plot over a wide range of external field strength F as is expected from the Fowler-Nordheim equation [27]. Cu and Au have been shown to exhibit a similar dependence [5]. However, for modified surfaces, i.e. surfaces involving regions of high aspect ratio such as carbon nanotube-modified surfaces [28], the classical Fowler-Nordheim relation has been shown in some cases to be no longer valid. It has been suggested [29] that this is due to changes in the shape of the surface barrier potential, from the form assumed by Fowler-Nordheim. As expected, the flat emitter surfaces show a linear Fowler-Nordheim plot in our calculations (Fig. 8.6). However, what is surprising is that the stepped surface, Pt6 \times (001), also shows linear behaviour (Fig. 8.6), even though the surface potential in this case must be very different from the Fowler-Nordheim model.

It would be interesting to calculate the spatially decomposed current density, which we believe can be formulated in terms of Green's functions and our embedding formalism, but this is left for future work. It would also be useful to find a relation between electron emission and step density. However, present limitations of computer resources prevent calculations on structures larger than those presented here.

Bibliography

- [1] A.A. Talin, K.A. Dean and J.E. Jaskie, Solid State Electronics **45**, 963 (2001).
- [2] M. Suzuki, T. Kusunoki, M. Sagawa and K. Tsuji, IEEE Trans Electron Dev. **49**, 1005 (2002).
- [3] P.R. Schwoebel and I. Brodie, J. Vac. Sci. Technol. B **13**, 1391 (1995).
- [4] E.W. Plummer and J.W. Gadzuk, Phys. Rev. Lett. **25**, 1493 (1970).
- [5] T. Ohwaki, H. Ishida and A. Liebsch, Phys. Rev. B **68**, 155422 (2003).
- [6] H.J. Kreuzer, L.C. Wang and N.D. Lang, Phys. Rev. B **45**, 12050 (1992).
- [7] Y. Gohda and S. Watanabe, Phys. Rev. Lett. **87**, 177601 (2001).
- [8] Y. Gotoh, M. Nagao, D. Nozaki, K. Utsumi, K. Inoue, T. Nakatani, T. Sakashita, K. Betsui, H. Tsuji and J. Ishikawa, J. Appl. Phys. **95**, 1537 (2004).
- [9] X. Zheng, G. Chen, Z. Li, S. Deng and N. Xu, Phys. Rev. Lett. **92**, 106803 (2004).
- [10] T. Sakata, M. Masutani and A. Sakai, Surf. Sci. **542**, 205 (2003).
- [11] S. Kitami, T. Nakane, A. Sakai and T. Sakata, Ultramicroscopy **73**, 37 (1998).
- [12] R. Ishii, K. Matsumura, A. Sakai and T. Sakata, Appl. Surf. Sci. **169-170**, 658 (2001).
- [13] σ is the field-inducing charge density placed at the vacuum embedding plane, and induces a field of strength $-4\pi\sigma$.
- [14] J.E. Inglesfield, J. Phys. C: Solid State Phys. **14**, 3795 (1981).
- [15] H. Ishida, Phys. Rev. B **63**, 165409 (2001).
- [16] M. Büttiker, Phys. Rev. Lett. **57**, 1761 (1986).
- [17] D. Wortmann, H. Ishida and S. Blügel, Phys. Rev. B **66**, 075113 (2002).
- [18] A.P.J. Stampfl, R. Martin, P. Gardner and A.M. Bradshaw, Phys. Rev. B **51**, 10197 (1995).
- [19] N.V. Smith, C.T. Chen and M. Weinert, Phys. Rev. B **40**, 7565 (1989).
- [20] S.L. Hulbert, P.D. Johnson and M. Weinert, Phys. Rev. B **34**, 3670 (1986).
- [21] N. Memmel and E. Bertel, Phys. Rev. Lett. **75**, 485 (1995).

- [22] H. Ishida, D. Wortmann and T. Ohwaki, Phys. Rev. B **70**, 085409 (2004).
- [23] A. Levy Yeyati and M. Büttiker, Phys. Rev. B **52**, R14360 (1995).
- [24] J.W. Gadzuk and E.W. Plummer, Rev. Mod. Phys. **45**, 487 (1970).
- [25] K. Wandelt, Applied Surf. Sci. **111**, 1 (1997).
- [26] R. Smoluchowski, Phys. Rev. **60**, 661 (1941).
- [27] A. Modinos, *Field, Thermionic and Secondary Electron Emission Spectroscopy*, Plenum Press, New York (1984).
- [28] P.G. Collins and A. Zettl, Phys. Rev. B **55**, 9391 (1997).
- [29] D.P Woodruff and T.A. Delchar, *Modern Techniques of Surface Science – Second Edition*, Cambridge University Press, Cambridge, England (1994).

CHAPTER 9

Conclusions and Outlook

Contents

Bibliography	125
-------------------------------	------------

In this thesis we have presented surface electronic structure calculations using a newly adapted embedding method [1]. Investigations were based on adsorbates and step defects on various transition metal surfaces. The embedding method allows for highly accurate results using full-potential LAPW basis functions.

The investigation of surface adsorbates is based on fully relaxed structures. The results show detailed bonding between substrate and adsorbate. For O/Cu(001) the missing row of the reconstructed surface permits relaxation of Cu and O atoms into the vacant sites, which position themselves in order to optimise bonding symmetry. The investigation of graphene/Ni(111) also shows some interesting bonding, in particular involving the interface states between the graphitic layer and the Ni substrate. It was proposed that these states may have significance in electron field emission.

Calculations on step defects have concentrated on the local aspects of surface properties. The local work function was described and shown to have significant reductions near the step site. This was also discussed in relation to increased field emission from stepped surfaces. It was shown that a four-fold increase in the tunneling current occurs for stepped Pd and Pt surfaces (of high step density), compared with flat surfaces.

Although the various approximations within the embedding method and tunneling calculations have been satisfactory for this thesis, there are several ways in which calculations could be improved. In the case of bonding atoms at the surface, the charge density is highly varying. In this case, the generalised gradient approximation [2] would provide a better description of the exchange-correlation potential over the local density approximation, which is used throughout this thesis. However, results presented in this thesis have shown good agreement with the literature.

A further improvement would be to investigate different types of surface defects. A limitation of our defect calculations is that only steps have so far been investigated. A much greater range of defects arises at surfaces, such as vacancies and kinks. Recently, kinked surfaces have gained much interest due to their chiral properties [3] and possible significance in drug design [4] and the pharmaceutical industry [5]. It would be interesting to investigate the local attributes of these defects, and compare the local effects of the surface properties with the step investigation.

Even though the results of the defect stepped surface investigation are based on well-defined structures with translational symmetry, we can relate these results to random defects on surfaces. The underlying principle of the step investigation is the high degree of locality of the altered surface properties. However, calculations involving steps have mainly concentrated on surfaces of high step density. In future calculations it will be important to investigate more isolated step sites. This would avoid any possibility of step-step interaction, and can be easily achieved by increasing the terrace length of our

surfaces. Unfortunately, computer resources limit the size of calculations at present.

This thesis has dealt with a wide range of surface topics, involving adsorbates, step defects, and field emission. The main message of the work is to promote the importance of the local description of surface physics when dealing with such aspects as surface reactivity [6], binding energy [7] and electron transport. The influence of defects can significantly alter the chemistry and physics of surface science. The result is that a huge amount of interest has been achieved in this area of research within the last few decades [8], with far more wide-ranging topics than those discussed in this thesis: crystal growth [9], electrochemistry [10, 11], and catalysis. I hope that this thesis makes a significant contribution to the subject.

Bibliography

- [1] H. Ishida, Phys. Rev. B **63**, 165409 (2001).
- [2] J.P. Perdew and Y. Wang, Phys. Rev. B **33**, 8800 (1986); A.D. Becke, J. Chem. Phys. **98**, 1372 (1992).
- [3] C.F. McFadden, P.S. Cremer and A.J. Gellman, Langmuir **12**, 2483 (1996).
- [4] D. Yu. Murzin, P. Mäki-Arvela and T. Salmi, Kinetics and Catalysis **44**, 323 (2003).
- [5] A.J. Gellman, J.D. Horvath and M.T. Buelow, J. of Mol. Catal. A: Chemical **167**, 3 (2001).
- [6] B. Gumhalter, K. Hermann and K. Wandelt, Vacuum **41**, 192 (1990).
- [7] K. Wandelt, J. Hulse and J. Küppers, Surf. Sci. **104**, 212 (1981).
- [8] G.E. Rhead, Surf. Sci. **68**, 20 (1977).
- [9] R. Stumpf and M. Scheffler, Phys. Rev B **53**, 4958 (1996).
- [10] V. Climent, G.A. Attard and J.M. Feliu, J. Electroanal. Chem. **532**, 67 (2002).
- [11] A. Berná, A. Rhodes and J.M. Feliu, Electrochim. Acta **49**, 1257 (2004).

APPENDIX A

Effective Charge

The amount of charge on any given atom in a molecular system is a useful quantity since it gives the value of charge transfer between bonding atoms. However, this value is rather difficult to obtain, arising from the definition of the atom boundary, and also because in a molecular system, electrons are shared along a path between bonding atoms. To overcome this rather arbitrary assignment, an *effective charge* q_i^* may be defined for an atom type i , rather than associating a static charge to a particular atom. The effective charge on an atom type i is a dynamical effect, defined from the change in the electric dipole contribution to the work function, when the atoms are displaced. Mathematical results for q_i^* , following that given in ref. [1], are given below.

For small applied electric fields ε , external to the surface, the force F_i on an atom of type i is given in terms of the effective charge by

$$F_i = q_i^* \varepsilon. \quad (\text{A.1})$$

The same effective charge is present when considering the work function change when the entire plane of atoms i is displaced normal to the surface:

$$\frac{d\Phi}{dz_i} = -\frac{4\pi q_i^*}{A_i}. \quad (\text{A.2})$$

Here A_i is the surface area per atom of type i , and $d\Phi/dz_i$ is the gradient of the work function/atom position dependence.

A periodic displacement of the surface atoms i produces a periodic variation in the local work function over the surface, due to (A.2), and this in turn produces patch electric fields. These produce a force on atoms i via (A.1), and an instability can result. It can be shown that the surface will be unstable due to these effects for wavelengths shorter than some critical wavelength, λ_c :

$$\lambda_c = \frac{8\pi^2 q_O^{*2}}{\alpha A}, \quad (\text{A.3})$$

where α is the local restoring force constant, estimated as 0.072 a.u. for O on Cu(001) using results obtained from Wuttig *et al.* [2]. Taking the effective charge as $q_O^* = -0.3|e|$, $A = 47.1$ a.u., and substituting into (A.3) gives $\lambda_c = 2.1$ a.u., which is far shorter than the minimum wavelength available to O, for which the interatomic spacing is 6.83 a.u. Hence the surface must be stable with respect to this model.

APPENDIX B

The Jellium Model

B.1 Initial Conditions

The initial potential for the jellium stepped surface is constructed by means of a Taylor expansion. In the x -direction a right-angled saw-tooth function $g(x)$ is used, whereas the z -direction dependence $f(z)$ includes the convenient shape of a tanh function:

$$V(x, z) = f(z + g(x)) \quad (\text{B.1})$$

$$= f(z) + g(x) \frac{\partial f(z)}{\partial z} \dots \quad (\text{B.2})$$

In this particular case, the Taylor expansion is taken up to the quadratic term. The saw-tooth function is given by the complicated Fourier expansion:

$$g(x) = \sum_n \left\{ \begin{array}{l} -2h \frac{\cos(\frac{n\pi c}{L})}{n\pi} \\ + \frac{h}{L^2} \left[2Lc \frac{\cos(\frac{n\pi c}{L})}{n\pi} - 2L^2 \frac{\sin(\frac{n\pi c}{L})}{(n\pi)^2} \right] \\ - \frac{h_c}{Lc} \left[2L^2 \frac{\sin(\frac{n\pi c}{L})}{(n\pi)^2} - 2Lc \frac{\cos(\frac{n\pi c}{L})}{n\pi} \right] \end{array} \right\} \sin\left(\frac{n\pi x}{L}\right) \quad (\text{B.3})$$

where c and h_c are given by:

$$c = \frac{h}{\frac{h}{L} + \frac{L}{h}}, \quad (\text{B.4})$$

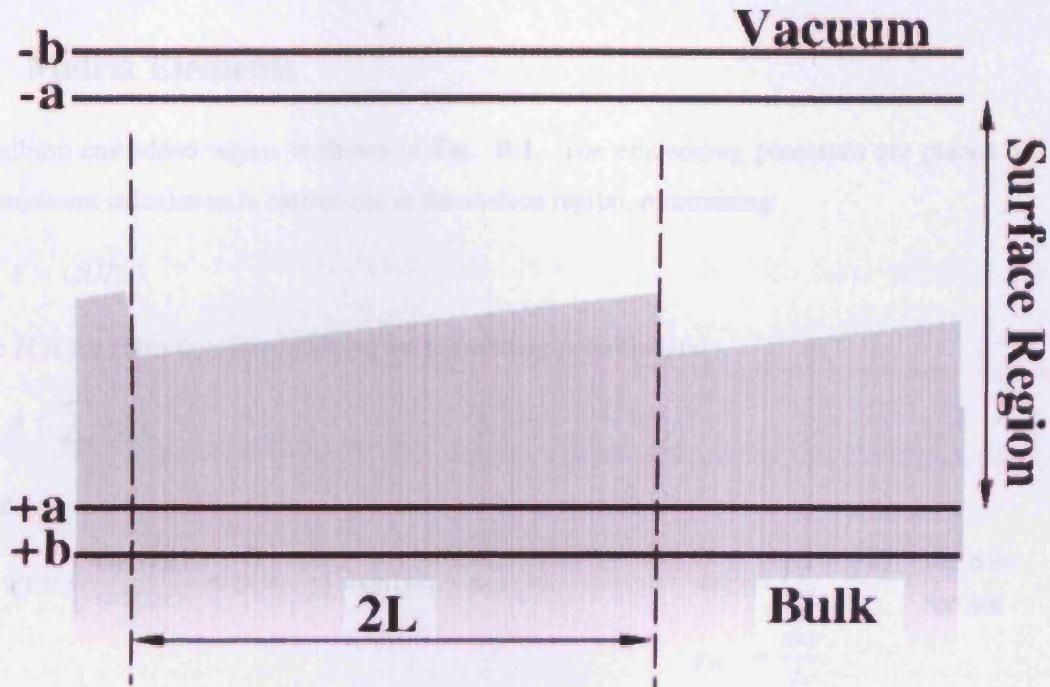


Figure B.1: Physical construction of the jellium surface. Region I is between the embedding planes on $\pm a$. The length $2L$ is the domain of the surface parallel direction, nominally containing one step site. $\pm b$ is the defined range of the trial wavefunctions in the z direction. $b > a$ to allow for variational freedom.

and

$$h_c = \frac{L}{\frac{h}{L} + \frac{L}{h}}. \quad (\text{B.5})$$

c and h_c define the step height and terrace length respectively. L and h are the input parameters defining the system structure (Fig. B.1).

The surface potential in the z -direction is given the form:

$$f(z) = \frac{V_0}{2} \tanh(-\alpha z) + \frac{V_0}{2}. \quad (\text{B.6})$$

The maximum potential difference between substrate and vacuum is controlled by V_0 , and α controls the rate of transition of the potential across the surface boundary. The form of the potential parallel to the step edges (here defined as the y -direction) is constant, since no structure exists in this direction within the jellium model.

We note that the theory using the jellium method takes the bulk-side z -displacement to be positive and the vacuum-side z -displacement to be negative (Fig. B.1). Conversely, the results of Chapter 6 use the opposite convention.

B.2 Matrix Elements

The jellium embedded region is shown in Fig. B.1. The embedding potentials are placed on $\pm a$. A self-consistent calculation is carried out in the surface region, minimising

$$E = \langle \phi | H | \phi \rangle \quad (\text{B.7})$$

where H is the Hamiltonian containing the embedding potential and

$$\phi = \sum_I a_I \chi_I \quad (\text{B.8})$$

having

$$\chi_I = \begin{cases} \cos(k_i z) \\ \sin(k_i z) \end{cases} \exp\{ik_y \cdot y\} \exp\{i(k_x + g_m) \cdot x\}, \quad \begin{aligned} k_i &= \begin{cases} \left(i + \frac{1}{2}\right) \frac{\pi}{b} & \text{for cos} \\ \frac{\pi i}{b} & \text{for sin} \end{cases} \\ g_m &= \frac{m\pi}{L}. \end{aligned} \quad (\text{B.9})$$

I corresponds to a set of $\{i, m\}$ values. This gives the overlap matrix elements as

$$O_{IJ} = 2L \int_{-a}^{+a} dz \begin{Bmatrix} \cos(k_i z) \\ \sin(k_i z) \end{Bmatrix} \begin{Bmatrix} \cos(k_j z) \\ \sin(k_j z) \end{Bmatrix} \delta_{mn}, \quad (\text{B.10})$$

and the Hamiltonian term as

$$H = K + U + D + G \quad (\text{B.11})$$

where

$$K_{IJ} = \frac{1}{2} \left[(k_x + g_n)^2 + k_y^2 + k_j^2 \right] \cdot O_{IJ} \quad (\text{B.12})$$

$$\begin{aligned} U_{IJ} &= \int_{-a}^{+a} dz \int_{-L}^{+L} dx \begin{Bmatrix} \cos(k_i z) \\ \sin(k_i z) \end{Bmatrix} \begin{Bmatrix} \cos(k_j z) \\ \sin(k_j z) \end{Bmatrix} V(x, z) \cos((g_n - g_m) x) \\ &\quad + i \int_{-a}^{+a} dz \int_{-L}^{+L} dx \begin{Bmatrix} \cos(k_i z) \\ \sin(k_i z) \end{Bmatrix} \begin{Bmatrix} \cos(k_j z) \\ \sin(k_j z) \end{Bmatrix} V(x, z) \sin((g_n - g_m) x) \end{aligned} \quad (\text{B.13})$$

$$D_{IJ} = \left[\begin{Bmatrix} \cos(k_i a) \\ \sin(k_i(-a)) \end{Bmatrix} \begin{Bmatrix} \sin(k_i(-a)) \\ -\cos(k_i a) \end{Bmatrix} - \begin{Bmatrix} \cos(k_i a) \\ \sin(k_i a) \end{Bmatrix} \begin{Bmatrix} \sin(k_i a) \\ -\cos(k_i a) \end{Bmatrix} \right] \quad (\text{B.14})$$

and,

$$\begin{aligned} G_{IJ} &= 2L \delta_{mn} \begin{Bmatrix} \cos(k_i(-a)) \\ \sin(k_i(-a)) \end{Bmatrix} \begin{Bmatrix} \cos(k_j(-a)) \\ \sin(k_j(-a)) \end{Bmatrix} \cdot G_0^{-1}(-a, E) \\ &\quad + 2L \delta_{mn} \begin{Bmatrix} \cos(k_i a) \\ \sin(k_i a) \end{Bmatrix} \begin{Bmatrix} \cos(k_j a) \\ \sin(k_j a) \end{Bmatrix} \cdot G_0^{-1}(a, E) \end{aligned} \quad (\text{B.15})$$

with

$$G_0^{-1}(-a, E) = \frac{1}{2} \left(2V - 2E - (k_x + g_n)^2 + k_y^2 \right)^{1/2} \quad (\text{B.16})$$

$$G_0^{-1}(a, E) = \frac{-i}{2} \left(2E - (k_x + g_n)^2 - k_y^2 \right)^{1/2}. \quad (\text{B.17})$$

Having constructed the Hamiltonian, the Green's function for the surface region can be found by the matrix inversion:

$$(H - EO)^{-1} = G \quad (\text{B.18})$$

which gives the charge density [3] as

$$\rho(\mathbf{r}, E) = \frac{1}{\pi} \Im m G(\mathbf{r}, \mathbf{r}; E + i\delta) \quad \mathbf{r} \in \text{I}. \quad (\text{B.19})$$

Knowing the charge density, the self-consistency cycle is achieved by constructing a new input potential from Poisson's equation:

$$-\nabla^2 V = 4\pi\rho(\mathbf{r}) \quad (\text{B.20})$$

and the exchange correlation potential, V_{xc} , using Ceperley-Alder-Perdew-Zunger parametrisation [4, 5]. The solution of Poisson's equation is discussed in the next section.

B.3 Solving Poisson's Equation at the Jellium Surface

The solution of the Schrödinger equation at the stepped surface from the initial, or trial, potential gives the charge density at this surface. To undergo self-consistency, the potential resulting from the charge density, the smooth jellium background, and the exchange-correlation potential, must be found.

Knowing the charge density, the exchange-correlation potential is calculated using the parametrised techniques of Ceperly-Alder-Perdew-Zunger [4, 5]. To find the potential due to the charge density of both the electronic structure and the positive background, i.e. the overall electrostatics of the system, Poisson's equation must be solved within the surface region. These quantities can be calculated separately. Considering only the $G_m = 0$ component of the electronic structure, the potential can be found from the charge density

$$\rho(x, z) = \sum_{mi} \rho_{mi} \exp(iG_m \cdot x) \begin{cases} \cos(k_i z) \\ \sin(k_i z) \end{cases} \quad (\text{B.21})$$

by integrating (B.20) twice, leaving

$$V(z) = A + Bz - 2\pi\rho_{00}z^2 + \sum_i' \frac{4\pi}{k_i^2} \rho_{0i} \begin{cases} \cos(k_i z) \\ \sin(k_i z) \end{cases}. \quad (\text{B.22})$$

A and B are constants determined by the boundary conditions $\partial V(-a)/\partial z = 0$ and $V(+a) = \phi_0 = \text{constant}$. The prime on the summation signifies that the zero-value of the summation index is ignored. For finite G_m , the potential is given by

$$V_m(x, z) = A \exp(G_m \cdot z) + B \exp(-G_m \cdot z) + \sum_{mi} \frac{4\pi}{k_i^2 + g_m^2} \rho_{mi} \begin{cases} \cos(k_i z) \\ \sin(k_i z) \end{cases} . \quad (\text{B.23})$$

The potential $V^b(x, z)$ due to the positive background charge is obtained by calculating the Fourier components of the jellium structure. The potential due to the smeared out background charge is then given by the expansion

$$V^b(x, z) = \sum_{\mathbf{g}} V_{\mathbf{g}}^b \exp(-i\mathbf{g} \cdot \mathbf{r}) . \quad (\text{B.24})$$

The overall potential is the sum of the electrostatic part (electronic and positive background) and the exchange-correlation potential. The input and output potentials of the present iteration of the self-consistent procedure are mixed to form a new input potential. The mixing procedure is described in Chapter 2.

Bibliography

- [1] J.E. Inglesfield and E.A. Colbourn, Phys. Rev. Lett. **66**, 2006 (1991).
- [2] M. Wuttig, R. Franchy, and H. Ibach, Surf. Sci. **213**, 103 (1989).
- [3] V. Heine, Solid State Physics **35**, 1 (1980).
- [4] D.M. Ceperley and B.J. Alder, Phys. Rev. Lett. **45**, 566 (1980).
- [5] J.P. Perdew and A. Zunger, Phys. Rev. B **23**, 5048 (1981).

